



Università degli Studi di Palermo



DIPARTIMENTO DI SCIENZE DELLA TERRA E DEL MARE
(Di.S.Te.M)

Ph.D. in Geochemistry

DOTTORATO DI RICERCA IN GEOCHIMICA- XXIII Cycle (GEO/08)

**The fate of Zr and Hf in aquatic systems under the effects of solid-liquid
interface processes, interpreted in the light of behaviour of
Rare Earths Elements and Yttrium**

Ph.D. thesis by

Maria Raso

Ph.D Coordinator:

Prof. F. Parello (University of Palermo)

Supervisors:

Prof. P.Censi (University of Palermo)

Dr. F. Saiano (University of Palermo)

Jan 2009 – Dec 2011



Università degli Studi di Palermo



DIPARTIMENTO DI SCIENZE DELLA TERRA E DEL MARE
(Di.S.Te.M)

Ph.D. in Geochemistry

DOTTORATO DI RICERCA IN GEOCHIMICA- XXIII Cycle (GEO/08)

**The fate of Zr and Hf in aquatic systems under the effects of solid-liquid
interface processes, interpreted in the light of behaviour of
Rare Earths Elements and Yttrium**

Ph.D. thesis by

Maria Raso

Ph.D Coordinator:

Prof. F. Parello (University of Palermo)

Supervisors:

Prof. P.Censi (University of Palermo)

Dr. F. Saiano (University of Palermo)

Reviewers:

Dr. T.H.Darrah (University of Rochester, Rochester)

Prof. S.A.Wood (University of Idaho, Moscow)

Prof P.Zuddas (University of Lyon, France)

Jan 2009 – Dec 2011

Ai miei genitori ... grazie!

Abstract

Solid-liquid interface processes are the main responsible for the Hydrosphere composition and contribute to regulating minor and trace elements composition in dissolved phase. Therefore, one of the most important geochemical challenges is to determine occurrence and features of solid-liquid interface processes. A large volume of literature produced in the late 80s suggests that such processes can be accurately determined by measuring the concentration and distribution of Y and Rare Earth Element (YREE). Reliability of this method lies in the REE capability of fractionating during dissolution-precipitation processes, and in the observed Y-Ho decoupling influenced by complexation equilibria between the solid and the dissolved phase. Recent, studies have begun to investigate whether Zr-Hf geochemical coherence and its loss during geochemical processes (if taking place) could be used to investigate occurring phenomena in aqueous media.

The present research was carried out to investigate Zr and Hf behaviour in several geochemical processes through coupling of the results with the information obtained by studying the YREE signature. The geochemical system investigated are: dissolution of suspended atmospheric particles in shallow seawaters, water column under oceanic conditions, mixing between oxic seawater and underlying anoxic deep brines, mixing between hydrothermal fluids and shallow water layers and classical rock-water interactions in thermal springs and groundwaters.

In order to obtain high-quality data and perform all measurements from the same sample aliquot, an original analytical approach, allowing the simultaneous determination of YREE, Zr and Hf occurring in pmol levels in several different aquatic matrices under variable conditions of salinity, was developed and validate.

Results obtained by coupling the analysis of YREE behaviour and the Zr/Hf signature, allowed us to establish the role played by fallout of atmospheric particulates in adding trace

elements to the shallowest water layer. During such process, minor and trace elements were mainly released from the external Fe-rich coating of atmospheric dust particles. Moreover, Zr/Hf and Y/Ho ratios coherently decreased under the effect of preferential release of Hf and Ho, and the whole process induced tetrad effects in the Gd-Ho interval whose extent is related to Y/Ho and Zr/Hf changes in the dissolved phase. Y/Ho and Zr/Hf co-variation always occurred under the effects of authigenic formation of a suspended phase until attaining to oxic seawater-anoxic brine interface. Authigenic particulate phase, which is responsible of the regulation of trace element and REE content along the water column, is undergone to reductive dissolution which delivers scavenged trace elements to the dissolved pool. Behaviour of Zr/Hf co-varied with Ce/Ce* through the shallow water interface and the oxic-anoxic interface, thus strengthening the interpretation that REE distribution in these transitional environments are driven by scavenging onto Fe-rich materials rather than onto Mn-oxyhydroxides as previously postulated.

Delivery of hydrothermal fluids under shallow water submarine conditions and in groundwater hydrothermal systems allowed us to investigate solid-liquid interactions and leaching of investigated elements from host rocks to the dissolved pool. Modification of compositions of hydrothermal fluids induced Zr/Hf and Y/Ho changes with rock-water amplitude interactions recorded by variations of positive Eu anomaly values. These relationships show to be broadly significant both for processes occurring in high temperature hydrothermal systems and in low temperature seawater media. Investigations carried out on Zr/Hf ratio and its changes in different conditions in aquatic systems, suggest its suitability for investigating interface processes and their mechanisms, especially if corroborated by Y/Ho ratio, Ce/Ce* and Eu/Eu* values. Specifically, Zr/Hf (mainly) and Y/Ho (secondarily) ratios in thermal and groundwaters are related to saturation index of studied waters, thus

corroborating the hypothesis that Zr/Hf and Y/Ho values are influenced by precipitation of authigenic minerals.

The main result standing out from this research is the large sensitivity of Zr-Hf reciprocal behaviour with respect to dissolution processes of lithogenic solids which represent the main Hf source, rather than Zr. This process causes coastal marine waters to have the lowest Zr/Hf values, and Mediterranean waters to be a large known source of Hf for Atlantic Ocean until today. This evidence explains the reason why seawaters from Pacific Ocean have higher Zr vs. Hf enrichments than Atlantic seawaters, whereas waters from Mediterranean sea are the least enriched.

Table of contents

Abstract	i
Table of contents	iv
List of Tables	vi
List of Figures	vii
Chapter 1: Introduction	1
1.1. Geochemical Aspects	1
1.2. Chemical Aspects	4
1.2.1. Zirconium and Hafnium	4
1.2.2. Yttrium and Rare Earth Elements (YREE)	6
1.2.3. Analytical Method	8
1.2.3.1. Co-precipitation on $\text{Fe}(\text{OH})_3$	9
1.3. Method Validation	11
1.3.1. Background	11
1.3.2. Linearity and working range	12
1.3.3. Detection Limit	14
1.3.4. Quantification Limit	15
1.3.5. Accuracy	15
1.3.5.1. Trueness	16
1.3.5.2. Precision	18
1.3.6. Measurement Uncertainty	21
1.3.6.1. Metrological approach or Bottom-up	22
Chapter 2: Method Development	29
2.1. Reagents, Materials and Instruments	29
2.1.1. Laboratory Material	29
2.1.2. Ultrapure water	29
2.1.3. Acids	29
2.1.4. Metal standard	29
2.1.5. Spiked solutions	29
2.1.6. Instrumentation and operational parameters	30
2.2. Extraction/pre-concentration optimization procedures	31
2.2.1. Co-precipitation on $\text{Fe}(\text{OH})_3$	31
2.2.2. Linearity and working range	32
2.2.3. Detection and Quantification Limit	33
2.2.4. Accuracy	36
2.2.4.1. Precision	36
2.2.4.2. Trueness	37
2.2.5. Evaluation of measurement uncertainty by metrological approach	41
Chapter 3: Investigated Geochemical Systems	53
3.1. Seawater under oceanic conditions and deep hypersaline basins	53
3.1.1. Seawater under oceanic conditions: Eastern Mediterranean Sea	53
3.1.2. Eastern Mediterranean deep hypersaline basins	55
3.1.3. Seawater and brines collection and storage	56

3.1.4.	Hydrography	58
3.1.4.1.	Oceanographic and physical-chemical characterization of seawater and basins	58
3.1.5.	Results	60
3.1.5.1.	Kryos seawater	60
3.1.5.2.	Deep hypersaline basin	69
3.2.	Hydrothermal submarine vents	75
3.2.1.	Fumarolic vents in Panarea Island	75
3.2.2.	Collection and storage	76
3.2.3.	Results	77
3.3.	Thermal springs	84
3.3.1.	Thermal springs along Belice Fault (Western Sicily)	84
3.3.2.	Sampling and storage	85
3.3.3.	Results	86
3.4.	Comprehensive discussion	95
3.5.	Conclusions	102
Appendix A		104
References		106

List of Tables

Tab. 1.1	Zirconium and Hafnium chemical properties	4
Tab. 1.2	Hydrolysis constants for Zirconium and Hafnium	5
Tab. 1.3	Performance parameters required for validation of different types of analysis	12
Tab. 1.4	The most common contribution to uncertainty measurement	26
Tab. 1.5	Mathematical expressions for the calculation of measurement uncertainty by	28
Tab. 2.1	ICP-MS operating conditions and measurement parameters	30
Tab. 2.2	Characteristic of calibration curves for each measured isotope	32
Tab. 2.3	Mean value (\bar{y}) and standard deviation (s) of signals of Calibration Blank in cps. IDL and IQL in pg/mL	34
Tab. 2.4	Mean values and standard deviations in pg/mL of procedural blanks, 16.6 times concentrated and methodological DL and QL in pg/mL	35
Tab. 2.5	The mean value and the standard deviation of the nine replicates obtained by the different co-precipitation of A_i and S_i solutions in pg/mL	36
Tab. 2.6	Mean value (A_m), standard deviation (s_{Am}), relative standard deviation %, repeatability limit (r), recovery % and standard deviation of recovery % of A solutions	37
Tab. 2.7	Mean value (S_m), standard deviation (s_{Sm}), relative standard deviation %, repeatability limit (r), recovery % and standard deviation of recovery % of S solutions	38
Tab. 2.8	t_{calc} values, degree of freedom and $t_{th}(P=0.05 \text{ and } P=0.02)$	39
Tab. 2.9	t_{calc} values, freedom degree and t_{th} values for A and S solutions	40
Tab. 2.10	Repeatability Uncertainty for YREE, Zr and Hf	43
Tab. 2.11	Recovery Uncertainty for YREE, Zr and Hf	44
Tab. 2.12	Reference Material contribution to combined uncertainty	45
Tab. 2.13	Reference Material uncertainty	46
Tab. 2.14	Instrumental calibration uncertainty	48
Tab. 2.15	Pre-concentration uncertainty	48
Tab. 2.16	Contributions to combined uncertainty	50
Tab. 3.1	YREE, Zr and Hf concentration (pmol/L) in Kryos seawater column	61
Tab. 3.2	YREE, Zr and Hf concentration (pmol/L) at the oxic-anoxic interface and inside the brine	69
Tab. 3.3	YREE, Zr and Hf contents (pmol/L) in hydrothermal submarine springs	78
Tab. 3.4	Physical-chemical parameters of water samples of western Sicily	86
Tab. 3.5	YREE, Zr and Hf concentration in western Sicily springs (pmol/L)	89

List of Figures

Fig. 1.1	Distribution diagram of hydroxide species for Zirconium and Hafnium	6
Fig. 1.2	YREE hydrolysis constant (β_1)	7
Fig. 1.3	Distribution diagrams for La (III) and Lu (III)	8
Fig. 1.4	Distribution diagram for Iron (III)	10
Fig. 1.5	Some key performance parameters	13
Fig. 1.6	Mathematical relationship between precision, trueness and accuracy	16
Fig. 1.7	Blocks diagram for the evaluation of uncertainty	23
Fig. 1.8	Cause and effect diagram	24
Fig. 2.1	Steps of extraction/pre-concentration procedure	31
Fig. 2.2	Cause and effect diagram for YREE, Zr and Hf determination by co-precipitation on $\text{Fe}(\text{OH})_3$	42
Fig. 2.3	Graphical representation of contributions to relative combined uncertainty	51
Fig. 3.1	Morphology of the Mediterranean Sea: geography of the basins	53
Fig. 3.2	Schematic representation of the upper thermocline circulation	54
Fig. 3.3	Sampling instrumentation	57
Fig. 3.4	Sampling points	58
Fig. 3.5	Vertical distribution of YREEs, Zr and Hf in Kryos basin	62
Fig. 3.6	PAAS normalised YREE patterns of LIW and EMDW	63
Fig. 3.7	PAAS normalised YREE pattern along the Kryos water column	64
Fig. 3.8	Zr vs Hf relationship from ocean to continental context	68
Fig. 3.9	Y/Ho vs Zr/Hf in Kryos water column	68
Fig. 3.10	YREE concentration (pmol/L) at the oxic-anoxic interface and in deep sea brines	69
Fig. 3.11	YREE, Zr and Hf ERs in interface and anoxic brine compared to overlying oxic seawater	70
Fig. 3.12	a) PAAS normalised YREE pattern in Tyro brine and seawater b) PAAS normalised YREE pattern in Tyro, Thetis and Medea brine	71
Fig. 3.13	SEM analysis of deep hypersaline sediments	74
Fig. 3.14	Aeolian Archipelago	75
Fig. 3.15	(a) Sampling points (modified from Sieland, 2009), (b) sampling plan, (c) Main gas exhalation of Bottaro sampling point in November 2002	77
Fig. 3.16	(a) PAAS normalised YREE pattern in hydrothermal submarine springs, (b) Chondrite normalised YREE pattern in hydrothermal submarine springs	79
Fig. 3.17	HSS 1C normalised YREE pattern	80
Fig. 3.18	PAAS normalised YREE pattern of particulate matter of HSS 1A	81
Fig. 3.19	Distribution coefficients (K_d)	82
Fig. 3.20	Y/Ho and Zr/Hf values in hydrothermal submarine springs	83
Fig. 3.21	Location of sampling sites and the main fault systems of Western Sicily	85
Fig. 3.22	Langelier-Ludwig diagram	87

Fig. 3.23	Na vs Cl relationship in water samples of western Sicily	88
Fig. 3.24	Ca vs SO_4^{2-} relationship in water samples of western Sicily	89
Fig. 3.25	ΣYREE (pmol/L) in water samples of western Sicily	90
Fig. 3.26	PAAS normalised YREE pattern of thermal springs (i)	91
Fig. 3.27	PAAS normalised YREE pattern of thermal springs (ii)	91
Fig. 3.28	PAAS normalised YREE pattern of cold springs (iii)	92
Fig. 3.29	Saturation index vs Y/Ho and Zr/Hf ratios relationship	93
Fig. 3.30	Ce/Ce* and LREE along the water column	96
Fig. 3.31	Ce/Ce* vs Zr/Hf for seawater and brine	97
Fig. 3.32	Eu/Eu* vs Y/Ho and Zr/Hf	99

Chapter 1: Introduction

1.1. Geochemical Aspects

Many geochemical processes are interface phenomena and their evolution represents the main factor influencing the composition of Hydrosphere. In the largest oceanic water masses, such geochemical processes occur in the shallowest water layer where delivery of atmospheric fallout takes place. Atmospheric fallout is responsible of trace element release from delivered solids to dissolved pool (Greaves et al., 1999). Solid-liquid interface processes regulate trace element distributions in dissolved phase through crystallization of suspended authigenic particulates or by inducing scavenging processes onto surfaces of detrital products of different nature. These phenomena occur along the whole water column until the deepest water layers, where changes of redox conditions are observed . If these phenomena take place (at the oxic seawater-anoxic deep sea brine interface) dissolutions of oxidized authigenic particulate causes another round of trace elements release and their sharing to crystallization of solids stable under reducing conditions. The last process re-introduces trace elements into the Lithosphere closing their residence time in dissolved media.

Further deliveries of trace elements occur when input of hydrothermal fluids are associated to volcanic activity both in bottom and shallow seawater. Under these conditions, when hot acidic and often reducing hydrothermal fluids are mixed with cold, slightly alkaline seawater, deep fluids become supersaturated with respect to many solids and precipitate them creating favourable conditions for new solid-liquid processes (German and Von Damm, 2005 and references therein). If these processes occur in deep-sea hydrothermal systems, like mid-oceanic ridges, their study is harder to carry out, mainly for technical reasons that can be easily overridden if hydrothermal vents are located in shallow marine systems.

Therefore, a wide literature about solid-liquid interface processes has been developed according to a direct approach which is often based on the geochemical investigation of only

the dissolved phase that participates in the reaction (Zuddas and Michard, 1990, 1993; Kendrick et al., 2002; Marini et al., 2003; Tamburo et al., 2011 and references therein), micro- and nanoscopic morphological observations (SEM-TEM investigations), and through kinetic investigation about the reactivity of solid surfaces (De Giudici and Zuddas, 2001; Cassiaux et al., 2006; Scislewski and Zuddas, 2010). Those studies were carried out under controlled thermodynamic conditions so to investigate the fate of mineral surfaces during dissolution-precipitation processes. Conversely, several geochemical studies based on the measurement of Y and Rare Earth Elements (here defined YREE) concentrations were carried out from the late 80s to indirectly investigate mechanisms and amplitudes of interface processes (Banner et al., 1989; Daux et al., 1994; Ojiambo et al., 2003). In those studies YREE content was measured both in solids and coexisting liquids so that particular YREE chemical characteristics allowed authors to infer information about migration mechanisms of trace elements among coexisting materials. Increasing analytical capabilities and precision of data analyses of elements occurring in pmol/L concentrations enabled researchers to exploit two fundamental YREE features: nephelauxetic effect typically occurring in *f* block elements, and decoupling of Y and Ho geochemical behaviour in accordance with features of interface processes (Kawabe, 1992; Bau, 1999; Irber, 1999; Monecke et al., 2002; Bau and Alexander, 2009).

This approach, which is not just limited to direct observations, allowed to investigate the mechanisms driving a wider range of solid-liquid processes occurring under a wider range of geochemical conditions. In this setting, processes like dissolution, adsorption, dissolved complexation, surface complexation and crystallization took place within a more natural environment. Recently, Godfrey et al. (1996), after the pioneering paper by Boswell and Elderfield (1988), have investigated the couple Zr and Hf behaviour in the dissolved pool and several further studied couple Zr/Hf and Y/Ho ratios as suitable geochemical proxies to

investigate solid-liquid processes under different geochemical conditions that are mainly found in the marine environment (Banks et al., 1999; Ece & Nakagawa, 2003; Godfrey et al., 2008; Firdaus et al., 2008; 2011;). Similarly to Y-Ho behaviour, these studies started from the Zr-Hf coupling during primary high temperature processes when elemental behaviour is mainly driven by their ionic charge and radii (Bau, 1996). Further studies were performed to investigate process occurring at low temperature conditions but a lack of data existed about Zr and Hf behaviour during these low temperature solid-liquid processes. In order to fill these gaps, my project was carried out exploring Zr and Hf behaviour under particular chemical-physical conditions occurring in several borderline environments of classical marine system like deep-sea brines, shallow seawater hydrothermal springs and in shallowest water layers in contact with the atmosphere. To relate all these processes to one another, a 3200 m deep seawater column under "oceanic" conditions was also investigated in order to clarify whether the Ce fate during oxidizing scavenging was coherent with Mn- or Fe-bearing suspended solids. This goal was obtained by studying the Zr-Hf geochemical couple and comparing it with their analogue Y-Ho and REE behaviour, in order to investigate processes occurring at solid-liquid interfaces with host rocks, atmospheric particulates, deep-sea sediments and suspended matter along the seawater column. Due to the lack of knowledge in terms of simultaneous determination of Zr, Hf and YREE in these matrices, the collection of geochemical results for this research required setting up an analytical method for the determination of these metals in the studied materials.

1.2. Chemical Aspects

1.2.1. Zirconium and Hafnium

The chemical behaviour of Zirconium and Hafnium are very similar due to the effect of the Lanthanide contraction: atomic and ionic radii are very similar and present the same valence state +4 (Cotton & Wilkinson, 1968).

Tab. 1.1 Zirconium and Hafnium chemical properties

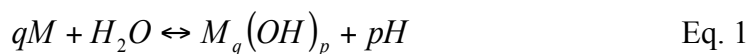
	Zr	Hf
Electronic configuration	[Kr]4d ² 5s ²	[Xe]4f ¹⁴ 5d ² 6s ²
Valence state	+4	+4
Atomic radius	1.45 Å	1.45 Å
Ionic radius	0.74 Å	0.75 Å

Because of their high ionic charge, Zr and Hf are defined High Field Strength (HFS) elements. Although they are of appropriate size for many cations sites in common minerals, their charge is too great and requires one or more coupled substitutions to maintain charge balance, so the replacements are often energetically unfavourable. Thus Hf and Zr are moderately incompatible elements (White W.H., 2001).

The aqueous chemistry of their M⁴⁺ ions would be confined mostly to strong acid solutions but, also there the existence of Zr⁴⁺ and Hf⁴⁺ is in doubt because of hydrolysis and is dominated by the formation of one or more polymeric species; the M⁴⁺ ions are coordinated by oxygen atoms. of OH⁻ bridges.

The solution chemistry of Zirconium is more extensive than Hafnium because of less tendency to hydrolysis (Eq. 1 and 2 and Tab. 1.2).

In Tab 1.2 the stability constant for equilibrium hydrolysis are listed



$$\beta_{q,p} = \frac{[M_q(OH)_p] \cdot h^p}{[M]^q} \quad \text{Eq. 2}$$

Tab. 1.2 Hydrolysis constants for Zirconium and Hafnium

	Log β_{11}	Log β_{12}	Log β_{13}	Log β_{14}	Log β_{15}
Zr⁴⁺	0.3	-1.7	-5.1	-9.7	-16
Hf⁴⁺	-0.25	-2.4	-6	-10.7	-17.2

If interactions with other species (HA) is very strong, hydrolysis can be neglected or suppressed.

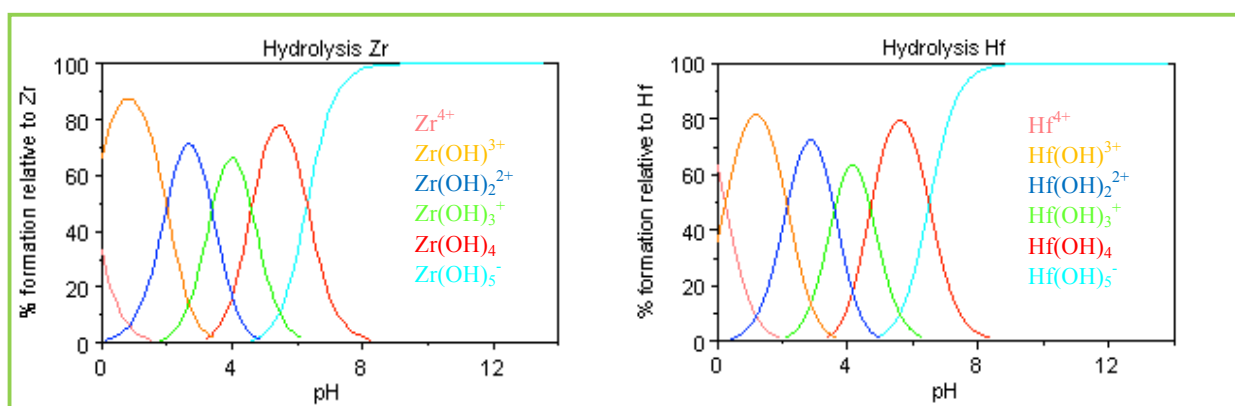


$$\beta_{q,p} = \frac{[M_qA_p] \cdot h^p}{[M]^q \cdot [HA]} \quad \text{Eq. 4}$$

According to the Ahrlund and Pearson classification (Pearson, 1963) Zirconium and Hafnium can be defined as “Hard Metal”, as such they form very stable complexes with hard ligands containing highly electronegative donor atoms such as oxygen and fluorine.

These ions form very stable complexes with fluoride ions (Norén, 1967), weaker ones with sulphate, and much weaker ones with halides and nitrate. Stable complexes are formed with multidentate ligands as polyaminocarboxylic acids and β diketones.

At the pH values of natural waters, as shown in Fig.1.1, Zirconium and Hafnium are present as anionic hydroxide species, $Zr(OH)_5^-$ and $Hf(OH)_5^-$ (Baes & Mesmer, 1976).

Fig. 1.1 Distribution diagram of hydroxide species for Zirconium and Hafnium

1.2.2. Yttrium and Rare Earth Elements (YREE)

The Rare Earth Elements (REE) series comprises the fifteen chemical elements with atomic numbers from Lanthanum 57 to Lutetium 71. They are also termed Lanthanides because the lighter elements in the series are chemically similar to Lanthanum. Yttrium (Y) shares the same chemical properties, including charge and ionic radius, as the heavier Lanthanides.

Chemical consistency, i.e. the property whereby all elements of the series show similar chemical behaviour, is determined by the electronic structure. The distribution of values of functions $[\Psi]^2$ for orbital 6s, 5d and 4f imply that the outermost electrons, which usually define the chemical behaviour of an element, are located in the 6s orbital whilst 5d and 4f orbitals are gradually filled in a portion of the atomic volume closest to the nucleus.

The characteristic that governs their relative behaviour is the ionic radius, which decreases progressively from La^{3+} (115 pm) to Lu^{3+} (93 pm) and is commonly defined as Lanthanide contraction (Cotton S., 2007).

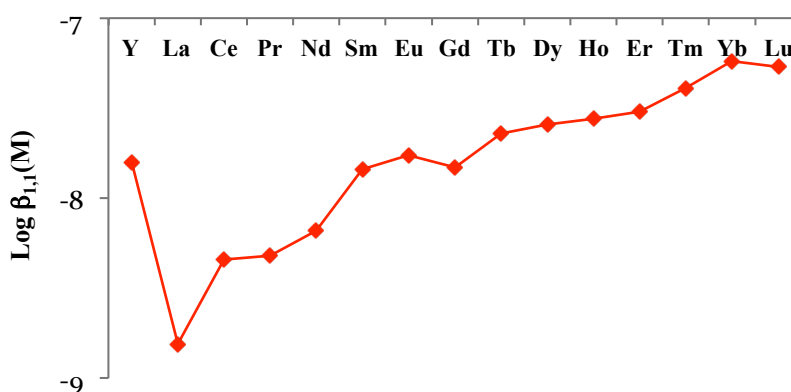
The Lanthanides are in the +3 valence state over a wide range of oxygen fugacities. At the oxygen fugacity of the Earth surface, however, Ce can be partly or wholly in the +4 state, whereas Eu can be partly in the +2 state at the low oxygen fugacities of the Earth's interior.

Because of their high charge and large radii, the REE are incompatible elements. However, the heavier REE can be accommodated to some degree in many common minerals. The heaviest REE readily substitute for Al^{3+} in garnet, and hence can be concentrated by it. Eu, when in its +2 state, substitutes for Ca^{2+} in plagioclase feldspar more readily than the other elements.

In solution, YREE show weaker tendency to hydrolysis than Zr and Hf. Taking into account the equilibrium hydrolysis, there are no discernable pattern in the magnitudes of hydrolysis across the YREE series other than a general, but poorly defined, increase between the lightest Lanthanides and the heaviest ones.

In spite of the close similarity in the ionic radii of Ho^{3+} and Y^{3+} , the hydrolysis behaviour of Y^{3+} is intermediate to that observed for Sm^{3+} and Eu^{3+} (Fig. 1.2). This is consistent with behaviour expected for Y^{3+} and Lanthanides complexation by a highly covalent ligand. Yttrium is a harder ion than any of the rare earths (Byrne et al., 1993). It is more weakly complexed than Ho in cases where Lanthanides–ligand interactions are significantly covalent and, on the contrary is more strongly complexed than Ho^{3+} in strongly electrostatic in character interactions.

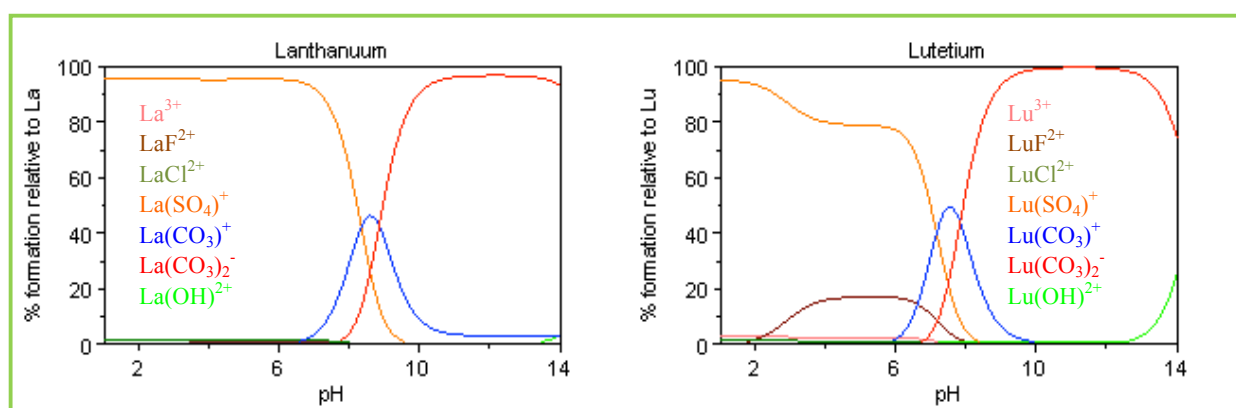
Fig. 1.2 YREE hydrolysis constant (β_1)



Due to the complexation of Lanthanides by a variety of ligands, only a small fraction of each YREE in neutral waters is typically in the form of free hydrated ions (M^{3+}). These ions form very stable complexes with carbonate ions, weaker ones with sulphate and phosphate, much weaker ones with halides and nitrate (Millero, 1992).

In natural system, at neutral or alkaline pH values, Lanthanides complexation is generally dominated by the formation of carbonate complexes $M(CO_3)^+$ and $M(CO_3)_2^-$ (Fig. 1.3) (Byrne and Sholkovitz, 1996; Tang and Johannessons, 2003).

Fig. 1.3 Distribution diagrams for La (III) and Lu (III)



1.2.3. Analytical Method

Understanding of a geochemical processes in any natural systems is only possible if the identification and quantification of the elements is obtained using reliable and comparable chemical measurements. For this reason the ability of an analytical protocol to generate reproducible values is paramount.

Under ideal conditions, the analysis of trace elements would not require any initial concentration or separation stage. Even with recent developments in selectivity and sensitivity, direct instrumental analysis is often impossible because the concentrations of analytes are below the detection limit of the method or the matrix provides interferences which must be removed. When both problems are encountered simultaneously, a

separation/pre-concentration step is obligatory. The determination of Zr, Hf and YREE in aqueous natural systems is a challenge mainly for two reasons: first of all because the concentration of these elements range from pg/mL to fg/mL, and secondly because even if ICP-MS is a highly sensible instrument and allows simultaneous multi-elements analysis, the likely salty matrix gives rise to analytical interferences and severe instrumental problems (such as. polyatomic ions mass spectral overlapping, instrumental drift, signal suppression and clogging of the sample introduction system of the instrument). Thus, selective enrichment and clean-up of these elements is indispensable prior to ICP/MS analysis.

Among all the pre-concentration techniques that were suitable to allow the simultaneous quantification of all analytes of interest, I have considered co-precipitation, (Ederfield and Greaves, 1988; Bau M. , 1999), sorption and chelation and ion-exchange resin (Orians & McKelvey, 1998; Moller et al., 1999).

1.2.3.1. Co-precipitation on $\text{Fe}(\text{OH})_3$

Co-precipitation allows the quantitative precipitation of the metal ions of interest by the addition of a co-precipitant. Co-precipitation of metal ions on collectors can be attributed to several mechanisms, as follows:

- *adsorption* – the charge on the surface can attract ions of opposite charge in solution
- *occlusion* – ions are embedded within the forming precipitate
- *co-crystallization* – the ion can be incorporated in the crystal structure of the precipitate.

The major disadvantage of a not extremely selective co-precipitation technique is that the voluminous precipitate can be a large source of contamination. One of the most common co-precipitant ion is iron, e.g. as $\text{Fe}(\text{OH})_3$.

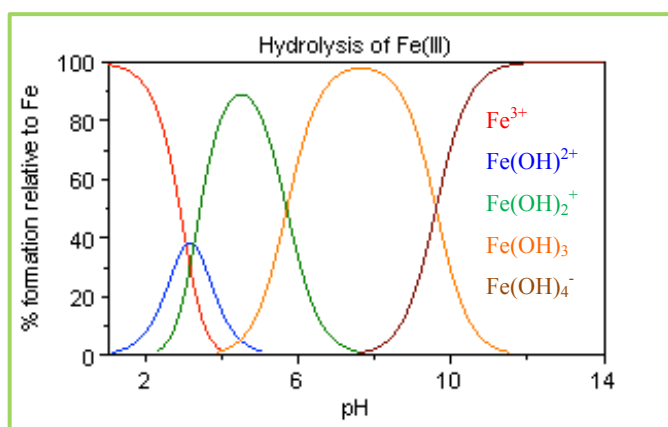
Normally hydrated oxides are obtained in the form of amorphous particles or very small crystals. These precipitates have a very large area and can adsorb large amounts of other electrolytes.

One of the most important parameters to be monitored for pre-concentration techniques of trace metals by co-precipitation on $\text{Fe}(\text{OH})_3$ is the pH value. Precipitation of hydroxide is usually obtained by ammonia solution. The buffer $\text{NH}_3/\text{NH}_4^+$ helps adjusting the pH value to ensure precipitation of most metal as the hydroxide.

An excess of ammonium ions avoids the precipitation of Zn^{2+} , Ni^{2+} , Cu^{2+} and Co^{2+} , due to the formation of complexes with ammonia $[\text{Co}(\text{NH}_3)_4]^{2+}$, $[\text{Ni}(\text{NH}_3)_6]^{2+}$, $[\text{Zn}(\text{NH}_3)_4]^{2+}$, as well as precipitation of alkaline earth metal.

As show by distribution diagram (Fig 1.4), at the optimum pH value of 8, all Fe(III) is present in the form $\text{Fe}(\text{OH})_3$

Fig. 1.4 Distribution diagram for Iron (III)



To co-precipitate, Fe standard solution was added to sample, then the pH was adjusted to 8.0 using concentrated ammonium hydroxide. To allow the homogenization and the precipitation of Fe-hydroxide, the samples were stirred for two hours and matured for two days. The samples were filtered and the Fe-hydroxide filtrate was washed with ultra-pure water and later dissolved in HCl 6 mmol/mL.

1.3. Method Validation

1.3.1. Background

Reliable analytical methods are required for compliance with national and international regulations in all area of analysis. Therefore, every laboratory must take appropriate measures to ensure to be able to provide data of required quality. Such measures include:

- using validated method of analysis;
- following internal quality control procedures;
- participating in proficiency testing schemes.

Method validation is one essential measure that a laboratory should implement to allow production of reliable analytical data.

The term “*Validation*” means to confirm, by means of objective evidences, that the requirements for a particular use or intended application have been met. The validation process therefore has the aim to establish through the evaluation of all relevant parameters (analyst, equipment, methods, reagents etc.) whether the chosen method is valid for the determinations that are going to be performed. Validation applies to a defined protocol for the determination of a specified analyte and range of concentration in a particular type of test material used for a specified purpose. In general, validation should check that the method performs adequately for the purpose throughout the range of analyte concentration and test material to which it is applied.

The validation procedure, as well as assessing the performance of an analytical method, provides the parameters to set the routine quality control in the application of the method. The aim on the routine quality control is to demonstrate that the method is under controlled conditions, or that the benefits are those expected.

The quality control can take on different characteristics, both in the laboratory (internal quality control), and among the different laboratories (external quality control).

The type of quality checks to be carried out depends on the nature, frequency, and critical analysis, the number of samples in the day, the possible use of automated systems, the difficulty of the analysis, and on the operator's opinion, based on experience gained using the method (In-House Method Validation, 2003).

The key performance parameters that require attention during validation, vary from requirement to requirement and from method to method. Some of the most important parameters are listed in Tab.1.3.

Tab. 1.3 Performance parameters required for validation of different types of analysis

Parameter	Type of analysis			
	Qualitative	Major component	Trace analysis	Physical property
Precision		✓	✓	✓
Specificity/Selectivity	✓	✓	✓	✓
Bias/Recovery		✓	✓	✓
Ruggedness	✓	✓	✓	✓
Sensitivity/linearity/working range		✓	✓	✓
Detection limit	✓		✓	
Quantification limit			✓	

In the following paragraphs parameters required for trace analysis will be discussed.

1.3.2. Linearity and working range

In any quantitative method it is necessary to determine the range of analyte concentrations or property values within which the method may be applied. At the lower end of the concentrations range, the limiting factors are the values of the limits of detection and/or quantification. At the upper end of the concentrations range, limitations will be imposed by various effects depending on the instrument response system (Fig 1.5).

Within the “*working range*” there may exist a linear response range. Within the linear range, signal response will have a linear relationship to analyte concentration or property value. The extent of this range may be established during the evaluation of the working range.

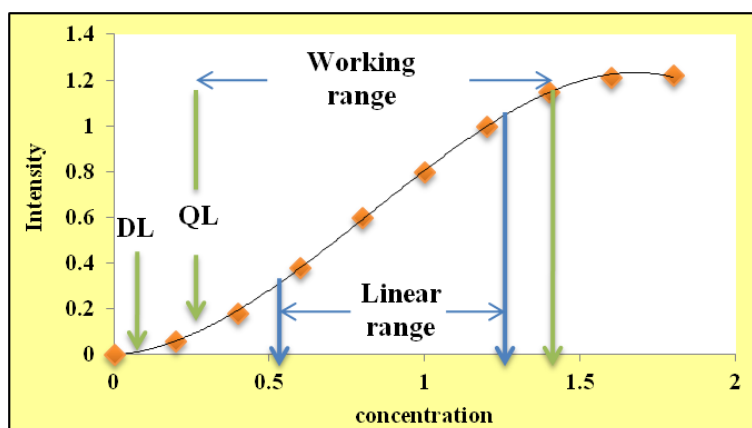
“*Linearity*” can be checked informally by examination of a plot of residual produced by linear regression analysis of the response on the concentrations in an appropriate calibration set (Burke S., 2001).

Despite its current widespread use as an indicator of quality of the fit, use of the correlation coefficient as a test for linearity is misleading and inappropriate, hence it should be avoided. Evaluation of the working and linear ranges will also be useful for planning what degree of calibration is required when using the method on a day-to-day basis. It is advisable to investigate the variance across the working range. Within the linear range, one calibration point may be sufficient, to establish the slope of the calibration line. Elsewhere in the working range, multi-point calibration will be necessary.

The relationship of instrument response to concentration does not have to be perfectly linear for a method to be effective but the curve should be repeatable from day to day.

Both the working range and the linear range may differ for different matrices, in agreement with the effects of interferences from the matrices themselves.

Fig. 1.5 Some key performance parameters



1.3.3. Detection Limit

In general the “*detection limit (DL)*” may be described as the concentration of the analyte that gives an instrumental signal significantly different from the blank or background signal. Although this parameter is widely used in many analytical documents there is still no full agreement between researchers, publishers and professional body on the interpretation of the expression “*significantly different*” because it acquires different meaning referring to qualitative or quantitative analysis.

Recently, there has been an increasing trend to define the detection limit as the analyte concentration giving a signal equal to the blank signal, y_b , plus three standard deviations of the blank, s_b . It should be based on several independent determinations of analyte concentration in a typical blank matrix or low level material, with no censoring of zero or negative results (In House Method Validation, 2003).

Other approaches to obtain detection limit that are based on regression analysis are the criterion of confidence bands and the propagation of errors. These are easy to calculate and are obtained by interpolation of intercept of the upper confidence band on the calibration line (criteria of confidence bands) or by interpolating the intercept of the sample of the upper confidence band on the calibration line (criterion of error propagation).

These two methods, when applicable, give us the more likely detection limit coming from statistical consideration. Unfortunately they provide only instrumental detection limit, due to the fact that calibration carried out using simple standard solutions doesn't take into account matrix effect.

In the method validation there should always be a distinction between “*instrument detection limit (IDL)*” and “*method detection limit (MDL)*”. The former is based on measurement on reagent blank and the latter on measurement of a blank real sample that has been processed through all steps of the method. Clearly IDL is often far smaller than a MDL

and it is inappropriate for method validation because does not take into account the matrix effects which may be relevant in determining detection limit (Thompson et al., 2002).

1.3.4. Quantification Limit

It is sometimes useful to state a concentration below which the analytical method cannot operate with acceptable precision.

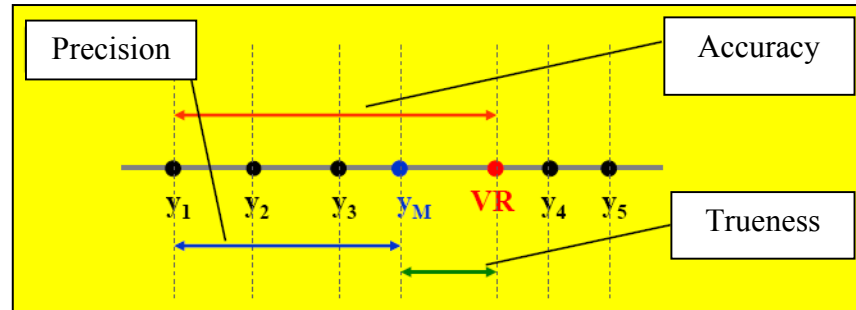
Since detection limit provides a value with an extremely low degree of accuracy, it is necessary to establish another limit that defines the minimum amount of analyte in the sample that can be detected with a probability established *a priori*. As such, the “*quantification limit (QL)*” for chemical and physical measurement is introduced, which is defined as the lowest concentration of analyte which can be determined with an acceptable level of accuracy (repeatability). As a detection limit it can be obtained through several completely independent determination of analyte concentration in a typical matrix blank or a low level material, with no censoring of zero or negative results. QL is defined as the analyte concentration giving a signal equal to the blank signal, y_b , plus ten standard deviations of the blanks, s_b .

1.3.5. Accuracy

“*Accuracy*” expresses the closeness of agreement between a test result and the accepted reference value. Method validation seeks to quantify the likely accuracy of results by assessing both systematic and random effects on results. Therefore, accuracy is normally studied in terms of two components: ***trueness*** and ***precision*** (Fig 1.6). The “*trueness*” (of a method) represents how close the mean of a set of results (produced by the method) is to the true value. Trueness is normally expressed in terms of “*bias*”. “*Precision*” is a measure of how close the results are to one another, and is usually expressed by measures such as the standard deviation, which describe the spread of results. In addition, an increasingly common

expression of accuracy is the “*measurement uncertainty*”, which provides a unique expression of accuracy. These three different parameters will be discussed below.

Fig. 1.6 Mathematical relationship between precision, trueness and accuracy



$$\text{Accuracy} = \text{Precision} + \text{Trueness}$$

1.3.5.1. Trueness

Trueness is expressed in terms of bias, with smaller bias indicating greater trueness. Typically it is determined by comparing the response of the method on a reference material to its known value (Thompson et al., 1999).

Certified Reference Materials (CRMs) are traceable to international standard with a known uncertainty and therefore can be used to address all aspect of bias (method, laboratory ect.) simultaneously, assuming that there is no matrix mismatch.

To check trueness using a reference material, the mean and standard deviation of a series of replicate tests are determined and compared to the characteristic values of the reference material by applying Student's t-test as follows:

$$t_{calc} = \frac{C_{CRM} - \bar{X}}{\sqrt{\frac{s_r^2}{n} + u_{CRM}^2}} \leq t_{th(p,v)} \quad \text{Eq. 5}$$

where the degree of freedom (ν) are calculated as follows

$$\nu = \frac{\left(\frac{S_r^2}{N} + u_{spike}^2 \right)}{\left(\frac{S_r^2}{N} \right)^2} \cdot (N - 1) \quad \text{Eq. 6}$$

If the test gives a positive result then it is possible to claim that the method provides accurate results to the significance level chosen and the recovery is equal to 1. The certified reference material should be as similar as the matrix under consideration during the validation. When interpreting the results, the uncertainty associated with the certified values should be taken into account.

When CRMs are not available, any material sufficiently well characterized for the purpose may be used. Example of *Reference Material* (RM) includes materials characterized by the reference material producers, but whose values are not accompanied by an uncertainty statement; materials characterized by their own manufacturer; materials characterized in the laboratory used as a reference material.

In the absence of reference material, or to support reference material studies, bias can be investigated by “*spiking*” and “*recovery*” procedures (Thompson et al., 1999).

An aliquot of a test material is analysed with the method under validation and another aliquot after the addition (spiking) of known mass of the analyte. By using this approach the spiked sample become the RM. Validation needs to fit the purpose, so the choice of reference material must be appropriate to the use. Care must be taken to ensure that the matrix composition is not changed during spiking and that the concentration of spiked materials closely matches that of the sample to be analysed.

In all cases, bias can be calculated as the ratio between the difference of the mean of a number of determinations of a test sample, obtained under repeatability condition, and its “true” or accepted concentration, as follows:

$$\%BIAS = \frac{C_0 - C_R}{C_R} \times 100 \quad \text{Eq. 7}$$

where C_0 is the mean value obtained from repeated measurements of a RM using the method under validation and C_R is the assigned property value for the RM.

Measurement bias is often called Recovery, which can be expressed as the ratio or percentage between C_0 and C_R and can be greater or lower than 100%.

When recovery is studied by means of spiking, the $\%Recovery$ is calculated as follows

$$\%Recovery = \frac{C_{(spike+blank)} - C_{blank}}{C_{spike}} \times 100 \quad \text{Eq. 8}$$

where $C_{spike+blank}$ is the mean value obtained from repeated measurements of a sample, after the spike addition; C_{blank} is the mean value obtained from repeated measurements of a sample prior to the spike addition, and C_{spike} is the known mass of the analyte added to the test portion.

1.3.5.2. Precision

According IUPAC, precision is “The closeness of agreement between independent test results obtained under stipulated conditions”(Thompson et al., 2002). The precision is usually stated in terms of standard deviation (s), the relative standard deviation (RSD), or standard deviation of the mean ($S(x_m)$) of an n number of replicates.

A measure of the dispersion of a set of n values is given by the equation

$$s = \sqrt{\frac{\sum_{i=1}^n (x_i - \bar{x})^2}{(n-1)}} \quad \text{Eq. 9}$$

The standard deviation s , relative to the mean value \bar{x} is equal to

$$RSD = \frac{s}{\bar{x}} \quad \text{Eq. 10}$$

The $S(x_m)$ is a measure of the dispersion of a set of mean values obtained from n repeated measurements

$$S(x_m) = \frac{s}{\sqrt{n}} \quad \text{Eq. 11}$$

Precision depends only on the distribution of random errors and does not relate to the true or specified value. The size of precision depends on a variety of factors, including the number of parameters that are modified during the precision study and the level of variation in the operating conditions. Individual sources of imprecisions can be studied; however, two types of overall precision are commonly estimated: “*repeatability*” and “*reproducibility*”. These represent the two extreme measures of precision which can be obtained. Repeatability can be expressed as “*repeatability or intermediate repeatability*”

Repeatability indicates the agreement between independent results obtained under repeatability condition; the method is performed by a single analyst with the same material, in the same laboratory, and over a short timescale (the smallest expected precision).

From the repeatability standard deviation, s_r , it is useful to calculate the “*repeatability limit r* ”, which enables the analyst to decide if the difference between duplicate analyses of a sample, determined under repeatability conditions, is significant.

$$r = |x_1 - x_2| = t_{(p,v)} \cdot s_r \cdot \sqrt{2} \quad \text{Eq. 12}$$

In order to evaluate the agreement between independent result obtained under repeatability condition but in a extended timescale the intermediate repeatability parameter can be used.

Reproducibility is a measure of dispersion of the distribution of test results under reproducibility conditions; the method is performed with the same material in different laboratories, by different analysts using different equipments and in a extended timescale.

This is the largest measure of precision normally encountered, although it does formally exclude variation with respect to time. Sometimes, in-between measures are the most useful as it is the case for precision measured between different analysts over extended timescales within a single laboratory. This is sometimes known as “intermediate precision”, but the exact conditions should be stated.

As for repeatability, it is useful to calculate the “*reproducibility limit (R)*” from the reproducibility standard deviation (s_R)

$$R = |x_1 - x_2| = t_{(p,v)} \cdot s_R \cdot \sqrt{2} \quad \text{Eq. 13}$$

Both repeatability and reproducibility are generally dependent on analyte concentration, and so they should be determined at a different level of concentrations and, if relevant, the relationship between precision and analyte concentration should be established. Relative standard deviation may be more useful in this case because concentration has been factored out and so it is largely constant over the range of interest, provided this is not too great.

1.3.6. Measurement Uncertainty

A measurement process, according to the International Vocabulary (VIM-ISO, 1993), is the set of operations made in order to determine a value of magnitude.

The measurand is a particular quantity subject to measurement. Since the true value of the measurand is unknown, the measurement process simply provides the best estimate of the true value. Therefore, the analytical result should not be considered complete, nor interpretable or comparable to reference values, if not accompanied by an uncertainty of the result as quantitative indicator of the degree of confidence attributed to the measure. “*Measurement uncertainty* (U)” is formally defined as a parameter associated with the result of a measurement, that characterizes the dispersion of the values that could reasonably be attributed to the measurand. This is a particularly important statement. It indicates that although the uncertainty is associated with a measurement result, the range quoted must relate to the possible range of values for the measurand (Eurachem Guide, 2000).

The existence of uncertainty associated with a measure does not mean that the validity of the measure is uncertain. On the contrary, its assessment strengthens the significance and validity of all information. Uncertainty is considered an essential part of good measurement practice and needs to be evaluated as a part of method validation.

Measurement uncertainty arises from a variety of sources, since in most cases a measurement result is obtained by combining results of several variables. Therefore measurement uncertainty must be calculated taking into account all sources contributing to the results; through applying the law of propagation of errors, their linear combination gives the “*combined uncertainty*”.

Assessing partial uncertainty as well as quantifying combined uncertainty of measurement is particularly useful for evaluating the critical stages of the process; high

uncertainty of a single step affects predominantly combined uncertainty, therefore its reduction modifying the method can lead to a significant reduction in combined uncertainty.

There are two general approaches to the estimation of uncertainty. The first described as “*empirical*”, “*experimental*”, “*retrospective*”, or “*top-down*”, uses some level of replication of the whole measurement procedure to give a direct estimate of the uncertainty for the final result of the measurement and is called the ‘empirical’ approach. The second, variously described as “*modelling*”, “*theoretical*”, “*predictive*” or “*bottom-up*”, aims to quantify all of the sources of uncertainty individually, and then uses a model to combine them (Manuali ARPA, 2003). It will accordingly be referred to as the “modelling” approach. These approaches are not mutually exclusive. All approaches can usefully be used together to study the same measurement system, if required. The applicability of the two approaches varies between the different materials to sample.

The important feature of these different classifications is that each is intended to ensure that all important effects, however grouped and evaluated, are taken into account in estimating the uncertainty. As long as this requirement is met, any categorisation scheme may be applied to the estimation of uncertainty. In the follow paragraph I will describe in detail the approach used in this thesis to estimate combined uncertainty.

1.3.6.1. Metrological approach or Bottom-up

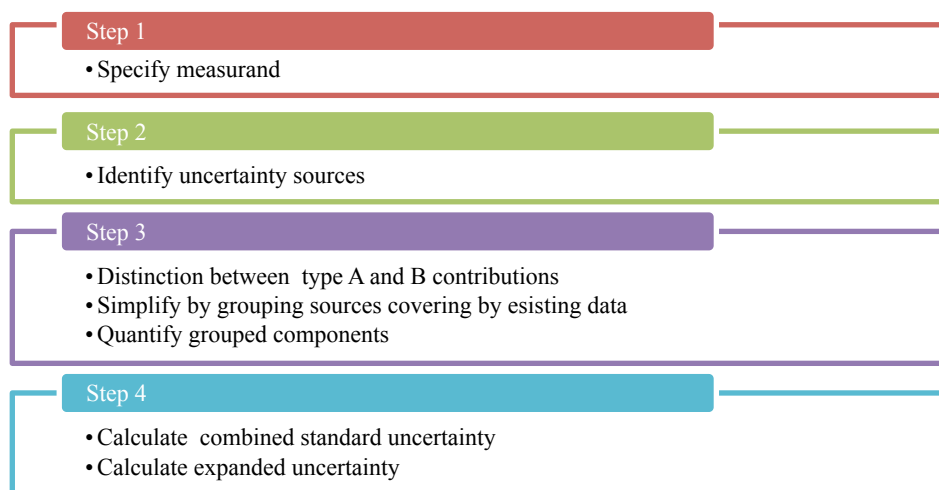
The methodology called “*metrological*” or “*bottom-up*” is the most rigorous, because it takes into account all the various contributions to uncertainty. This approach, derived from the physical sciences, is based on transfer of concepts derived from physical measurements to chemical or microbiological measures. Physical measures are mainly applied to properties involving mass, length, time, temperature etc; in most cases, physical measures only require a correction due to environmental influences and depend upon well-defined physical laws.

In addition, the variables have usually systematic or constant error that are added together algebraically and have all the same weight in uncertainty determination.

In contrast, chemical and microbiological measurements are characterized by a predominance of random variability, and are added vectorially in the final calculation of uncertainty. This means that greater contribution from these measurements will weigh more on the result.

To quantify the combined uncertainty it is necessary to divide the process into four distinct phases: definition of the measurand, identification of sources of uncertainty, quantification of components to uncertainty components, calculation of combined uncertainty (Fig.1.7) (Eurachem guide, 2000).

Fig. 1.7 Blocks diagram for the evaluation of uncertainty



Step 1: Definition of the measurand

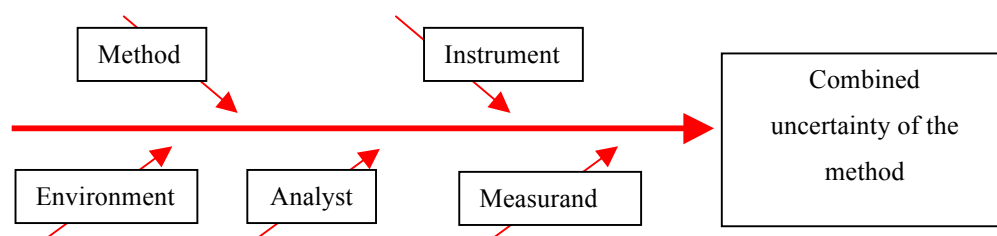
Definition of the measurand requires both a clear and unambiguous statement of what is being measured, and a quantitative expression correlating the value of the measurand to the parameters upon which it depends. These parameters may be other measurands, quantities which are not directly measured, or constants. Formally, the output quantity, about which information is required (denoted by Y), is often related to input quantities, (denoted by $x_1...$

x_N) about which information is available, by a measurement model in the form of a measurement function

$$Y = f(x_1, x_2, x_3 \dots x_n) \quad \text{Eq. 14}$$

Usually, these parameters can be derived from analytical methods or standard operating procedures. In the first phase, a helpful tool is represented by the “cause and effect” diagrams which show all variables that may contribute to combined uncertainty (Fig .1.8).

Fig. 1.8 Cause and effect diagram



- ✓ **Method:** is the greatest contributor to the calculation of uncertainty. It should take into account all the analytical procedures adopted.
- ✓ **Instrument:** it should take into account the instrument and the reference materials used for calibration.
- ✓ **Environment:** it is sometimes negligible; it includes pressure, temperature, dilution, volumes and influences instrumental stability.
- ✓ **Analyst:** he is fundamental for the calculation of the method uncertainty. His training, experience and attention should be considered.
- ✓ **Measurand:** it should take into account the intrinsic nature of the measurand.

Step 2: Identification of sources of uncertainty

Between the possible sources of variability, effects statistically evaluated by repeated measures and effects leading to consistent and repeatable changes must be distinguished. The former, called “*Type I contribution or Type A uncertainty*”, depend on the intrinsic variability of method, and are measurable but not predictable; furthermore, they can be taken into account by accuracy, expressed in terms of repeatability of the method. The latter, called “*Type II contribution or Type B uncertainty*”, is often not known and, whenever possible, it is estimated in terms of standard deviations, evaluated from assumed probability distributions based on experience or other kind of information. Examples of Type B contributions are: the uncertainty of reference materials used for calibration of instruments, uncertainty of calibrated equipment (glassware, etc.), uncertainty due to instrumental calibration, uncertainty due to environmental conditions, uncertainty due to the recovery (where applicable), etc.

These factors, when known, must be considered and inserted into the formula for calculating the combined uncertainty. The best estimate of the uncertainty takes into account the contribution of the method repeatability and other parameters documented with certainty. Since repeatability includes all the uncertainties about the individual steps of analytical process, in the combined uncertainty only those that are not included in the calculation of repeatability are to be added.

Following this approach it is avoided to take into account several times the same contribution which would lead to an overestimation of the range. In the Tab.1.4 the most common contributions are shown, listed by operators, broken down by type, and sources.

Tab. 1.4 The most common contribution to uncertainty measurement

Stages	Contribution to uncertainty		Sources	Degree of freedom
Weighing	Measure	Type A	Unc. repeatability	n-1
	Calibration	Type B	Calibr. certificate	∞
Dilution	Measure	Type A	Unc. repeatability	n-1
	Calibration	Type B	Calibr. paper	∞
Treatment	Recovery	Type B	Experimental	n-1
Calibration	Instrumental Calibration	Type B	Calibr. Curve	n-1 or n-2
	Certified Reference material	Type B	Certificate	∞
Final measure	Measure	Type A	Unc. repeatability	n-1
Repeatability	Standard deviation of repeatability	Type A	Unc. repeatability	n-1

Step 3: Quantification of components of the uncertainty

After identifying the uncertainty sources, as explained in step 2, the next step is to quantify the uncertainty arising from these sources. In some cases, particularly when few or no method performance data is available, the most suitable procedure may be to evaluate each uncertainty component separately. The general procedure, used in combining individual components, is to prepare a detailed quantitative model of the experimental procedure, to assess the standard uncertainties associated with the individual input parameters, and to combine the uncertainties by using the law of propagation of uncertainties.

In-house development and validation studies mainly consist in the determination of the method performance parameters indicated in Table 1.3 and 1.4 and discussed in the previous paragraphs. Uncertainty estimation from these parameters utilises:

- The best available estimate of overall precision.
- The best available estimate (s) of overall bias and its uncertainty.
- Quantification of any uncertainties associated with effects incompletely accounted for in the above overall performance studies.

Step 4: Calculation of combined uncertainty

Before combining, all uncertainty contributions must be expressed as standard uncertainties, that is, as relative standard deviations. The general relationship between the uncertainty $\dot{U}_C(y)$ of a value y and the uncertainty of the independent parameters $\dot{U}(X_n)$, on which it depends is described by

$$\dot{U}_C(y(x_1, x_2, x_N)) = \sqrt{\sum_{i=1, N} \dot{U}(x_i)^2} \quad \text{Eq. 15}$$

The final stage is to multiply the combined standard uncertainty by the chosen coverage factor in order to obtain an “*expanded uncertainty*”. The expanded uncertainty is required to provide a range which may be expected to include a large fraction of the distribution of values, which could reasonably be attributed to the measurand.

In choosing a value for the coverage factor (k), a number of issues should be considered: the level of confidence required, knowledge of the underlying distributions, and knowledge of the number of values used to estimate random effects.

For most purposes it is recommended that k is set to 2. However, the k value may be insufficient when the combined uncertainty is based on statistical observations with relatively few degrees of freedom. k that depends on the effective number of degrees of freedom will be set equal to the two-tailed value of Student's t for the number of degrees of freedom associated, and for the level of confidence required (normally 95%). The overall degree of freedom (ν_{eff}) may be calculated by the Welch–Satterthwaite expression:

$$\nu_{eff} = \frac{\dot{U}_C^4}{\sum \left[\frac{\dot{U}_i^4}{\nu_i} \right]} \quad \text{Eq. 16}$$

Tab. 1.5 Mathematical expressions for the calculation of measurement uncertainty by metrological approach

Quantity	Mathematical equation	Relative quantity
Average	$\bar{x} = \sqrt{\frac{\sum_{i=1}^n x_i}{n}}$	
Standard deviation	$s = \sqrt{\frac{\sum_{i=1}^n (x_i - \bar{x})^2}{(n-1)}}$	
Standard deviation of the mean	$S(x_m) = \frac{s}{\sqrt{n}}$	
Repeatability Uncertainty	$u_{rep}(x) = \sqrt{\frac{s^2}{n}}$	$\dot{u}_{rep}(x) = \frac{u_{rep}(x)}{x_m}$
Type B uncertainty	$u_{ref} = \frac{a}{\sqrt{3}}$	$\dot{u}_{ref}(x) = \frac{u_{ref}(x)}{x}$
Standard deviation of the residuals	$s_{y/x} = \sqrt{\frac{\sum_i y_i^2 - \left(\sum_i y_i\right)^2 \cdot (n-2)}{n - b \cdot \left(\sum_i x_i y_i - \sum_i x_i \sum_i y_i / n\right)}}$	
Instrument Calibration Uncertainty	$s_{cal} = \frac{s_{y/x}}{b} \sqrt{\frac{1}{m} + \frac{1}{n} + \frac{(y_i - \bar{y}_{regr})^2}{b^2 \sum (x_i - \bar{x}_{regr})^2}}$	
Calibration Uncertainty	$u_{cal}(x_m) = \sqrt{\frac{\sum s_{cal}^2}{n^2}}$	$\dot{u}_{cal}(x_m) = \frac{u_{cal}(x_m)}{x_m}$
Recovery Uncertainty	$u_{rec} = \sqrt{\frac{s^2}{n} + u_{CRM}^2}$	$\dot{u}_{rec} = \frac{u_{rec}}{X_m}$
Combined Uncertainty		$\dot{U}_C(y(x_1, x_2, x_N)) = \sqrt{\sum_{i=1, N} \dot{U}(x_i)^2}$
Effective degree of freedom	$v_{eff} = \frac{\dot{U}_C^4}{\sum \left[\dot{U}_i^4 / v_i \right]}$	
Expanded Uncertainty	$U(y) = \dot{U}_c(y) \cdot k \cdot y$	

Chapter 2: Method Development

2.1. Reagents, Materials and Instruments

2.1.1. Laboratory Material

All labware was in polyethylene, polypropylene or in Teflon and the calibration of all volumetric equipments was verified. A calibrated E42-B balance (Gibertini, Italy) was used to weigh all samples and standards.

2.1.2. Ultrapure water

High purity water, 18.2 MΩ cm, was obtained by Easy pure II purification system (Thermo, Italy).

2.1.3. Acids

Ultra clean acids (nitric and hydrochloric acid and ammonia solution) used for sample analysis and cleaning plastic-ware were purchased from VWR International.

2.1.4. Metal standard

Working standard solutions for each element (Zr, Y, La, Ce, Pr, Nd, Sm, Eu, Gd, Tb, Dy, Ho, Er, Tm, Yb, Lu and Hf) were daily prepared by stepwise dilution of the multi-element stock standard solutions DBH, Merck or CPI International ($1000 \pm 5 \mu\text{g/mL}$) in a HCl 1 mmol/mL medium.

2.1.5. Spiked solution

As described in section 1.3.5.1, CRMs are useful tool to test the analytical procedure; if these are not available the method can be investigated by spiking and recovery.

For our purposes nine aliquots of two seawater solutions, A₁-A₉ and S₁-S₉, spiked with $19.92 \pm 0.31 \mu\text{g/mL}$ for Zr, Hf and YREE, were prepared to test and validate the method proposed. Solutions A₁-A₉ were prepared by spiking nine *procedural blanks* (P_{B1}- P_{B9}) obtained by co-precipitating twice the seawater sample with Fe-hydroxide, until the

concentrations of YREE, Zr and Hf were below the instrumental quantification limit. S₁-S₉ solutions were obtained by directly spiking seawater matrix.

2.1.6. Instrumentation and operational parameters

An ICP-MS instrument (Agilent Technologies 7500ce Series Spectrometer) equipped with a collision cell, was used for the analyses of all the investigated trace elements. All parameters were daily optimized using a 1 ng/mL solution of ⁷Li, ⁸⁹Y, ¹⁴⁰Ce, ²⁰⁵Tl; to obtain maximum sensitivity, the instrument was tuned on ⁸⁹Y. Each solution was measured three times, and ICP-MS analyses were carried out with a classical external calibration approach. Such approach involved investigating a range of concentrations for each element between 2.5 and 500 pg/mL, and using ²⁰⁵Tl (1 ng/mL) as internal standard (ISTD) to compensate for any signal instability or sensitivity changes during the analysis. A 1M HCl blank was run during the analysis to ensure that the memory effect, due to the more refractory elements, was negligible. Operating conditions are shown in Table 2.1.

Tab. 2.1 ICP-MS operating conditions and measurement parameters

RF power	1550 W
Sample uptake rate	0.400 mL/min
Coolant argon flow rate	15 L/min
Carrier argon flow rate	0.80 L/min
Make-up argon flow rate	0.25 L/min
Torch	Quartz
Nebuliser	MicroMist 200 µl
Sampler and Skimmer Cones	Nickel
Number of scans	3
Ion lens settings	Adjusted daily to obtain max. signal intensity
Washing time	1 min (5% v/v HNO ₃)
Oxide ¹⁵⁶ CeO ⁺ / ¹⁴⁰ Ce ⁺ ratio	< 0.8%
Double charged ⁷⁰ Ce ⁺⁺ / ¹⁴⁰ Ce ⁺ ratio	< 0.5%
Measured Isotope:	⁸⁹ Y, ⁹⁰ Zr, ¹³⁹ La, ¹⁴⁰ Ce, ¹⁴¹ Pr, ¹⁴³ Nd, ¹⁴⁷ Sm, ¹⁵¹ Eu, ¹⁵⁸ Gd, ¹⁵⁹ Tb, ¹⁶¹ Dy, ¹⁶⁵ Ho, ¹⁶⁷ Er, ¹⁷¹ Yb, ¹⁷⁵ Lu, ¹⁷⁸ Hf.
Internal standard	²⁰⁵ Tl 1000 pg/mL

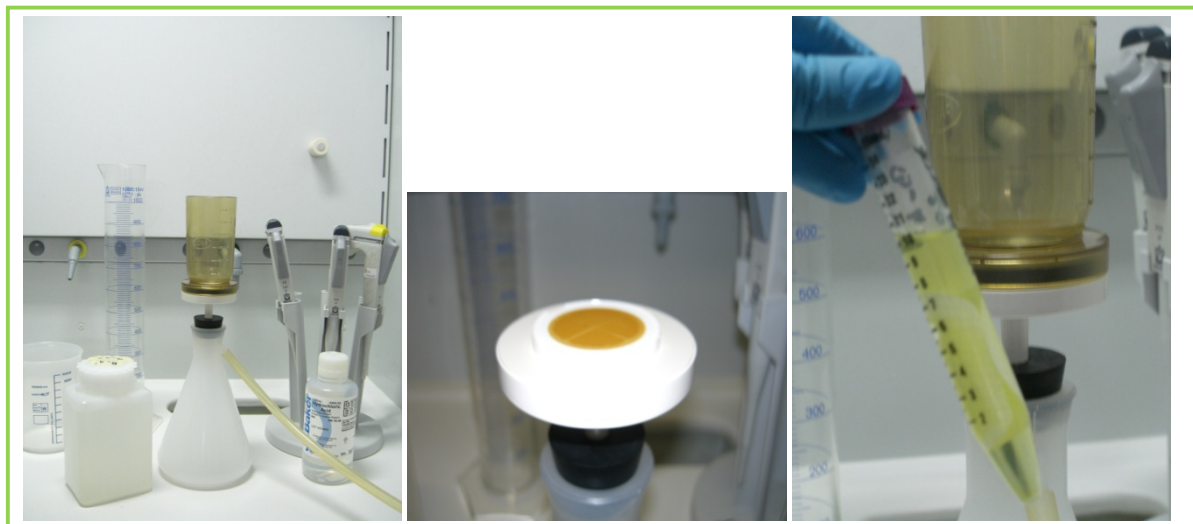
2.2. Extraction/pre-concentration optimization procedure

2.2.1. Co-precipitation on $\text{Fe}(\text{OH})_3$

The extraction/pre-concentration procedure by co-precipitation on $\text{Fe}(\text{OH})_3$ was tested by treating A_1 - A_9 and S_1 - S_9 solutions, prepared as described in paragraph 2.1.5.

Each sample was added of 1.000 ± 0.005 mL of the Fe standard solution (1000 ± 5 mg/mL) then ammonium hydroxide was added to $\text{pH } 8.0 \div 8.5$. The sample bottle is capped and agitated for two hours to allow the homogenization and the precipitation of Fe-hydroxide. The iron precipitates as a reddish-brown to yellow, gelatinous flake. The bottle is allowed to stand for 24h while the iron hydroxide precipitate settles to the bottom of the sample bottles. The iron precipitate was collected by filtration on acid pre-cleaned $0.45\mu\text{m}$ Nucleopore membrane and washed twice with 25 mL of ultra-pure water. The filter with the Fe-hydroxide precipitate was put into 15 mL polypropylene centrifuge tube and dissolved in 10 mL of HCl 6 mmol/mL (Fig. 2.1). Prior to ICP-MS measurement, the solution was diluted six times with ultra-pure water. The overall pre-concentration was about 16 times.

Fig. 2.1 Steps of extraction/pre-concentration procedure



2.2.2. Linearity and working range

To evaluate linearity of calibration curve for each element, residual distribution over the x values was evaluated. Moreover the data were subjected to Mandel's test to verify the validity of the linear model, and slope (b) and interception (a) were tested to statistically assess the possibility of the curve intersection with the zero point. The r squared value (R^2), indicating linearity between signal and concentration, was considered satisfactory when ≥ 0.998 for all the isotopes monitored.

For all elements in the working range 2.5-500 pg/mL, residual analysis indicated a normal distribution and the Mandel's test was positive; therefore, a statistically significant linear relationship existed. In Tab. 2.2 shows the a, b, and R^2 values for all elements.

Tab. 2.2 Characteristic of calibration curves for each measured isotope

Isotope	Slope(b)	Intercept(a)	R^2
Y	1.57E-02	2.69E-02	1
Zr	5.59E-03	3.57E-02	0.9998
La	2.13E-02	4.11E-02	0.9998
Ce	2.03E-02	7.18E-02	1
Pr	2.45E-02	7.87E-03	1
Nd	4.44E-03	7.53E-03	0.9998
Sm	3.84E-03	7.51E-04	1
Eu	1.27E-02	2.82E-03	1
Gd	4.17E-03	2.36E-02	0.9986
Tb	2.82E-02	7.66E-03	1
Dy	7.06E-03	3.29E-03	1
Ho	2.82E-02	5.73E-03	1
Er	9.46E-03	3.99E-03	1
Tm	2.99E-02	4.75E-03	1
Yb	4.94E-03	3.11E-03	1
Lu	2.95E-02	5.67E-03	1
Hf	8.30E-03	8.83E-03	1

2.2.3. Detection and Quantification Limit

To carry out instrumental detection and quantification limit (IDL and IQL) analyses, 9 different aliquots of calibration blank (HCl 1 mmol/mL) were measured. Behaviour of collected data was analysed according to the Shapiro-Wilks's test ($P=0.05$) to verify the normal distribution of obtained data, and according to David's ($P=0.05$), Grubb's ($P=0.05$) and Huber's tests ($P=0.05$) to verify the presence of outliers (Miller and Miller, 2005). The IDL and IQL in pg/mL, was calculated according to the following expressions:

$$Y_{DL} = y + 3s \quad \text{Eq. 17}$$

$$Y_{QL} = y + 10s \quad \text{Eq. 18}$$

combined into:

$$DL = \frac{y_{DL} - a}{b} \quad \text{Eq. 19}$$

$$QL = \frac{y_{QL} - a}{b} \quad \text{Eq. 20}$$

Tab. 2.3 shows mean values and the standard deviations of replicates in counts per second (cps) and all values obtained, in pg/mL, for IDL and IQL.

All the results demonstrate the very good performance of ICP-MS. In particular, the instrumental DL and QL were for all elements comparable or lower than the mean concentration estimated in natural seawater, from Zr (20 pg/mL) Y, (13 pg/mL), to Tb, 0.14 (pg/mL).

**Tab. 2.3 Mean value (y) and standard deviation (s) of signal of Calibration Blank in cps.
IDL and IQL in pg/mL**

Isotope	Calibration Blank			
	y _{CB}	s _{CB}	IDL	IQL
Y	3.04E-02	2.68E-03	0.7	1.9
Zr	9.09E-02	1.62E-02	18.6	38.8
La	6.72E-02	3.27E-03	1.7	2.8
Ce	1.01E-01	4.90E-03	2.2	3.9
Pr	2.50E-02	3.47E-03	1.1	2.1
Nd	1.17E-02	9.72E-04	1.6	3.1
Sm	4.76E-03	6.77E-04	1.6	2.8
Eu	7.84E-03	1.30E-03	0.7	1.4
Gd	7.28E-03	7.67E-04	2.3	3.6
Tb	1.55E-02	1.59E-03	0.4	0.8
Dy	7.13E-03	5.81E-04	0.8	1.4
Ho	1.47E-02	1.06E-03	0.43	0.7
Er	7.09E-03	8.30E-04	0.6	1.2
Tm	1.49E-02	9.64E-04	0.4	0.7
Yb	6.46E-03	8.11E-04	1.2	2.3
Lu	1.54E-02	1.36E-03	0.5	0.8
Hf	5.77E-02	4.31E-03	7.5	11.1

To take into account the matrix contribution, method detection and quantification limit (MDL and MQL) were evaluated on measurements of a blank real sample that had been processed through all steps of the method.

Procedural blank was obtained by subjecting 9 aliquots of seawater real samples to entire method twice. The results for first (B) and second co-precipitation (B') are summarized in Tab 2.4. In B solution the concentrations of Y, Zr and light YREE (from La to Nd) were much higher than middle and heavy YREE (from Sm to Lu) and Hf. These results can be explained both by their natural abundance in earth's crust and by the presence of Ba²⁺ and Sr²⁺ adsorbed onto the surface of Fe-hydroxide precipitate which presence in ICP-MS may generate interferences in particular ⁸⁸SrH⁺ and ¹³⁸BaH⁺ on ⁸⁹Y and ¹³⁹La, ⁸⁹YH⁺, ¹³⁹LaH⁺, ¹⁴⁰CeH⁺, ¹⁴⁵NdH⁺ on ⁹⁰Zr, ¹⁴⁰Ce, ¹⁴¹Pr and ¹⁴⁶Nd.

The second co-precipitation (B' solution) gave results close or minor to IQL for ^{90}Zr (40.88 ± 6.83 pg/mL) and from ^{147}Sm (3.18 ± 0.85 pg/mL) to ^{178}Hf (1.02 ± 0.84 pg/mL). By analyzing the concentrations of B' solution, I concluded that further co-precipitation was not necessary, inasmuch the quantification was not possible because below the IQL.

The obtained procedural blank (B' solutions) was used to carry out MDL and MQL, calculated as above (Tab. 2.4). As expected MDL and MQL were much higher than IDL and IQL. The determination of these parameters allowed me to state that our ICP-MS would be able to return a correct quantification of most of the elements even without pre-concentration, if there were no interferences from the matrix.

Tab. 2.4 Mean values and standard deviations in pg/mL of procedural blank, 16.6 times concentrated and methodological DL and QL in pg/mL

	B		B'		Method	
	C_B	s_B	$C_{B'}$	$s_{B'}$	MDL	MQL
Y	336.61	12.96	15.66	3.67	27.2	54.4
Zr	296.04	6.56	40.88	6.83	61	109.6
La	2263.66	715.32	123	97	408.3	1076.6
Ce	190.36	6.86	42	16	92.3	208.6
Pr	24.87	0.57	5	2	11.5	25.9
Nd	109.18	5.42	13.95	4.57	28.4	62.1
Sm	25.35	1.12	3.18	0.85	5.3	11.6
Eu	6.40	0.04	1.4	0.62	3.2	7.5
Gd	50.45	3.58	5.14	2.04	11.9	26.3
Tb	4.66	0.22	1.30	0.67	3.5	8.2
Dy	28.48	1.17	3.47	1.65	8.3	20.2
Ho	6.5	0.2	1.3	0.7	2.1	4.8
Er	19.65	0.63	2.31	1.3	3.7	7.7
Tm	2.77	0.14	2.21	0.84	4.5	10.1
Yb	17.00	0.47	2.15	1.16	6	14.2
Lu	3.05	0.15	1.04	0.44	2.9	7.5
Hf	2.37	0.27	1.02	0.84	3.8	9.7

2.2.4. Accuracy

2.2.4.1. Precision

Precision of the method was evaluated by subjecting samples A₁-A₉ and S₁-S₉ to the entire method of analysis. Data from procedural blank and seawater, without YREE, Zr and Hf, were subtracted to spiked solutions. After controls carried out according the Shapiro-Wilks's (P=0.05), David's (P = 0.05), Grubb's (P=0.05) and Huber's tests (P = 0.05) the mean value of the nine replicates (A_m and S_m) and the standard deviations (s_A and s_S) (Tab.2.5) were calculated (about 16.7 times concentrated). These values were higher than method QL but into the linearity range of the calibration adopted. Relative standard deviation percentage (RSD%) for most of the elements both for A and S solutions were less than 10% except for ¹³⁹La.

Tab. 2.5 Mean value and standard deviation of the nine replicates obtained by the different co-precipitation of A_i and S_i solution in pg/mL (about 16.6 times concentrated)

A solutions				S solution		
	C _A	s _A	RSD%	C _S	s _S	RSD%
Y	332.2	12.7	4	368.1	33.9	9
Zr	247.7	30.9	16	325.0	124.1	56
La	348.3	107.5	31	-1695.2	715.3	-42
Ce	335.1	23.3	7	370.4	30.8	8
Pr	341.8	16.2	5	316.0	2.4	1
Nd	339.8	16.5	5	362.5	21.8	6
Sm	353.6	4.6	1	372.3	11.6	3
Eu	341.8	16.4	5	374.2	10.3	3
Gd	347.6	15.0	4	372.6	21.9	6
Tb	343.8	17.1	5	369.6	9.6	3
Dy	339.8	16.6	5	363.9	10.9	3
Ho	342.1	16.3	5	364.9	9.3	3
Er	343.7	16.0	5	365.9	9.5	3
Tm	341.9	17.4	5	362.3	10.0	3
Yb	334.1	17.7	5	356.1	10.9	3
Lu	342.8	17.0	5	362.0	9.5	3
Hf	337.1	16.1	5	293.4	15.0	5

Extraction/pre-concentration procedure by co-precipitation on $\text{Fe}(\text{OH})_3$ for YREE, Zr and Hf gave precise results. According to Gonzales et al., (2007) for amounts of analyte lower than $1\mu\text{g/Kg}$ the maximum standard deviation accepted is 45%.

2.2.4.2. Trueness

In order to evaluate the accuracy of the entire procedure, trueness was evaluated by recovery of YREE, Zr and Hf from A_i and S_i solutions according Eq. 8. Presence of outliers and normal distribution was verified as described in section 2.2.3. Mean values, standard deviations, and recovery percentages both for A and S solution are listed in Tab 2.6 and 2.7, respectively. Recovery percentages are in the range 101% - 108% and 95% - 113%, with a good repeatability ($< 10\%$) for A_m and S_m solutions, respectively.

Tab. 2.6 Mean value (A_m), standard deviation (s_{Am}), relative standard deviation %, repeatability limit (r), recovery % and standard deviation of recovery % of A solution

	A_m	S_{Am}	RSD %	r	Rec %	S_{Rec} %
	pg/mL	pg/mL		pg/mL		
Y	20.08	0.74	4	2.40	100.8	4
Zr	14.94	0.86	6	2.78	75.0	4
La	21.05	6.42	31	20.71	105.7	32
Ce	20.74	1.23	6	3.97	104.1	6
Pr	21.06	0.77	4	2.47	105.7	4
Nd	20.95	0.89	4	2.87	105.2	4
Sm	21.12	0.28	1	0.90	106.0	1
Eu	21.05	0.71	3	2.31	105.7	4
Gd	21.42	0.94	4	3.02	107.5	5
Tb	21.18	0.76	4	2.44	106.3	4
Dy	20.93	0.75	4	2.40	105.1	4
Ho	21.07	0.72	3	2.33	105.8	4
Er	21.18	0.78	4	2.51	106.3	4
Tm	21.06	0.71	3	2.30	105.7	4
Yb	20.58	0.70	3	2.27	103.3	4
Lu	21.11	0.76	4	2.44	106.0	4
Hf	20.77	0.87	4	2.81	104.3	4

Tab. 2.7 Mean concentration value (S_m), standard deviation (s_{Sm}), relative standard deviation %, repeatability limit (r), recovery % and standard deviation of recovery % of S solution

	S_m	s_{Sm}	RSD%	r	Rec %	S_{rec} %
	pg/mL	pg/mL		pg/mL		
Y	22.06	2.03	9	6.56	110.8	10
Zr	19.48	1.91	10	6.16	97.8	10
La	-101.72	42.92	-42	138.38	-510.7	215
Ce	22.21	1.85	8	5.95	111.5	9
Pr	18.95	0.15	1	0.47	95.1	1
Nd	21.73	1.31	6	4.22	109.1	7
Sm	22.33	0.69	3	2.24	112.1	3
Eu	22.44	0.62	3	2.00	112.7	3
Gd	22.34	1.31	6	4.24	112.2	7
Tb	22.16	0.58	3	1.86	111.3	3
Dy	21.82	0.65	3	2.11	109.5	3
Ho	21.88	0.56	3	1.79	109.9	3
Er	21.94	0.57	3	1.83	110.2	3
Tm	21.73	0.60	3	1.93	109.1	3
Yb	21.36	0.65	3	2.11	107.2	3
Lu	21.71	0.57	3	1.83	109.0	3
Hf	17.60	0.90	5	2.90	88.3	5

Matrix contribution and the role of interferences were discovered by subjecting both A_i and S_i solutions to the entire method. In spiked real seawater (S solutions) we obtained values slightly higher than the A solution, thus confirming that also our procedural blank, despite the high similarity to the real matrix, brought about significant differences mostly in ultra-traces analytical determination. This is dramatically explained by ^{139}La , that in A solutions showed an acceptable recovery of $106 \pm 21\%$, whereas in S solution could not be quantified.

To verify if the differences between A and S solutions could be accounted for by random or systematic errors, a significance test was employed. In order to decide whether the difference between two samples means, A_m and S_m , was significant, the null hypothesis ($H_0 = \mu_A = \mu_S$) was tested.

The statistic t parameter was calculated for each element:

$$t_{calc} = \frac{A_m - S_m}{s \cdot \sqrt{\frac{1}{n_a} + \frac{1}{n_s}}} \quad \text{Eq. 21}$$

where s was calculated from:

$$s^2 = \frac{(n_A - 1) \cdot s_A^2 + (n_S - 1) \cdot s_S^2}{n_A + n_S - 2} \quad \text{Eq. 22}$$

Comparison of t_{calc} with t_{th} showed in Tab 2.8 allowed to state that only for Ce, Nd, Gd, Er, Tm, Yb and Lu the differences are due to random errors ($t_{calc} < t_{th}$), whereas for the other elements the differences are due to systematic errors, thus confirming that the two matrices are significantly different.

Tab. 2.8 t_{calc} values, degree of freedom and $t_{th}(P=0.05 \text{ and } P=0.02)$

	T_{calc}	ν	$t_{th95\%}$	$t_{th98\%}$
Y	2.59	14	2.14	2.51
Zr	5.68	11	2.2	2.59
La	6.99	9	2.26	2.69
Ce	1.78	12	2.18	2.56
Pr	6.00	12	2.18	2.56
Nd	1.46	15	2.13	2.49
Sm	3.97	12	2.18	2.56
Eu	3.57	11	2.2	2.59
Gd	1.53	12	2.18	2.56
Tb	2.93	14	2.14	2.51
Dy	2.58	15	2.13	2.49
Ho	2.52	14	2.14	2.51
Er	2.25	14	2.14	2.51
Tm	1.98	13	2.16	2.53
Yb	2.36	15	2.13	2.49
Lu	1.80	14	2.14	2.51
Hf	7.13	14	2.14	2.51

In the case of repeated analyses of a certified reference material, the guideline ranges for the deviation from the certified values of the experimentally determined recoveries range from -50% to +20% for mass fraction lower than 1 µg/Kg. Data are acceptable only when they fall within the ranges indicated above (2002/605/EC). When no such CRMs are available, as described in section 1.3.5.1, it is acceptable that trueness of measurements be assessed through recovery of known amounts of the analyte added to a blank matrix. Therefore, following these criteria, analyses of results for A and S solutions demonstrated that YREE, Zr and Hf were almost completely recovered after co-precipitation on Fe(OH)₃.

To evaluate the efficiency of recovery on a statistical basis, discriminant function t is calculated (Eq. 6) and compared with the theoretical value of student t .

In Eq. 6 used to calculate t , C_{CRM} and u_{CRM} have been replaced with C_{spike} and u_{spike} equal to 19.92 ± 0.031 pg/mL for all analytes. The results obtained by statistical consideration (Tab 2.9), indicated that in A_i solutions t_{calc} is less than t_{th} only for Y, La, Ce, Yb and Hf thus they were fully recovered, while in S_i solutions the recovery was unitary only for Zr and Ce.

Tab. 2.9 t_{calc} values, freedom degree and t_{th} values for A and S solutions

A solution					S solution			
	t_{calc}	ν	$t_{\text{th } 95\%}$	$t_{\text{th } 98\%}$	t_{calc}	ν	$t_{\text{th } 95\%}$	$t_{\text{th } 98\%}$
Y	0.40	40	2.02	2.33	2.74	10	2.26	2.69
Zr	11.07	22	2.08	2.41	0.52	7	2.45	2.97
La	0.43	5	2.57	3.16	6.34	4	2.78	3.5
Ce	1.54	16	2.13	2.49	2.81	7	2.45	2.97
Pr	2.84	49	2.02	2.33	3.06	2286	1.98	2.28
Nd	2.39	35	2.03	2.34	3.26	15	2.14	2.51
Sm	3.64	356	1.98	2.28	6.08	47	2.02	2.33
Eu	2.83	44	2.02	2.33	6.06	20	2.09	2.42
Gd	3.31	25	2.06	2.39	3.91	9	2.31	2.75
Tb	3.07	39	2.02	2.33	6.04	77	1.99	2.29
Dy	2.55	53	2.01	2.31	4.90	55	2.01	2.31
Ho	2.86	43	2.02	2.33	5.34	86	1.99	2.28
Er	3.03	36	2.03	2.34	5.47	80	1.99	2.28
Tm	2.77	33	2.04	2.35	4.81	70	2.00	2.30
Yb	1.68	61	2.00	2.30	3.71	55	2.01	2.31
Lu	2.82	29	2.05	2.37	4.91	109	1.98	2.28
Hf	2.00	37	2.03	2.34	5.05	20	2.09	2.42

This result not alarming, and did not compromise the method validation; but implies that it must be taken into account in the calculation of measurement uncertainty (Thompson et al., 1999).

2.2.5. Evaluation of measurement uncertainty by metrological approach

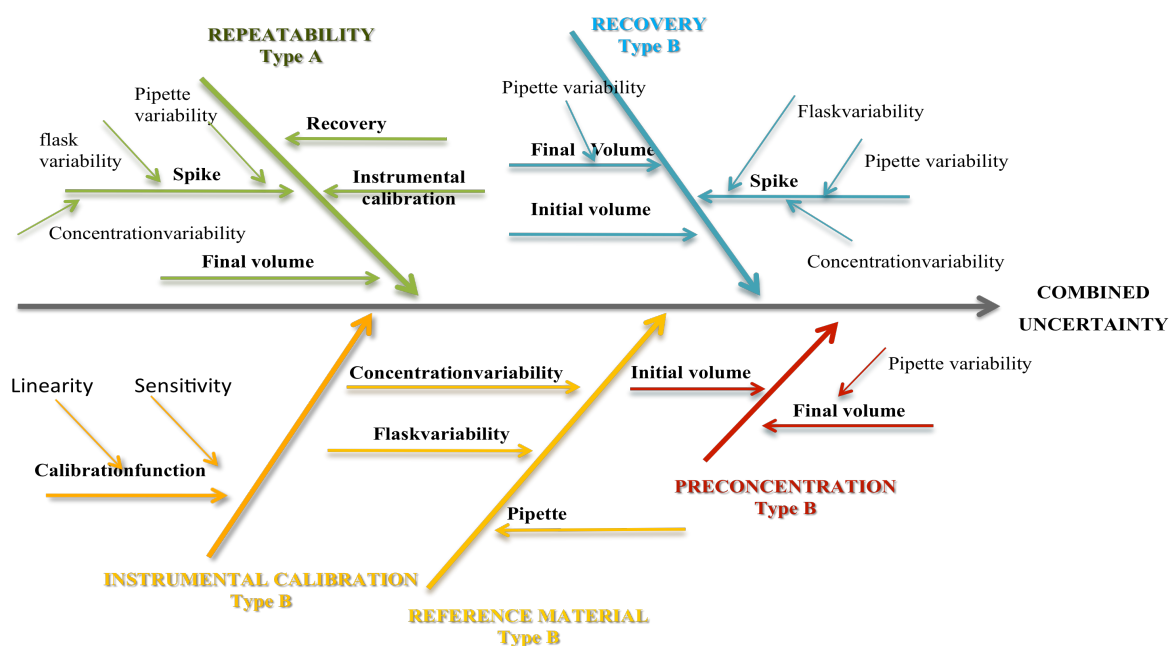
After evaluating key performance parameters for extraction/pre-concentration procedure of YREE, Zr and Hf by co-precipitation on Fe(OH)_3 , I assessed measurement uncertainty by metrological approach. Firstly, the entire procedure was divided into four steps according to Fig. 1.6. Measurand was defined by the mathematical relation

$$X_i = \frac{\left[\left(\frac{I_{spiked+blank} - a}{b} \right) - \left(\frac{I_{blank} - a}{b} \right) \right] * Dil.Factor * V_{HCl}}{V_{sample}} \quad \text{Eq. 23}$$

Where X_i is the concentration expressed in pg/mL of each investigated analyte, I is the instrumental response, $Dil.Factor$ is the dilution made prior to ICP-MS measurement, V_{HCl} is the volume of HCl in which Fe hydroxide was dissolved and V_{sample} is the initial volume of sample.

To identify the various contributions to the measurement uncertainty, I built a cause and effect diagram in which I pointed out all possible sources that may contribute to combined uncertainty (Fig. 2.2). The parameters in the equation of the measurand are represented by the main branches of the diagram. Further factors were added to the diagram, considering each step in the analytical procedure, until the contributory factors became sufficiently remote.

Fig. 2.2 Cause and effect diagram for YREE, Zr and Hf determination by co-precipitation on $\text{Fe}(\text{OH})_3$



By examining the input variables and their contributions, identified as significant to the final calculation of the uncertainty, I concluded that the following sources of uncertainty must be taken into account:

- repeatability uncertainty expressed as precision of the method (type A contribution);
- recovery uncertainty (type B contribution);
- reference material (type B contribution);
- instrumental calibration uncertainty (type B contribution);
- pre-concentration uncertainty (type B contribution).

Repeatability uncertainty

The contribution of the repeatability uncertainty was calculated on the basis of results from nine replicates performed for the study of the precision (see section 2.2.4.1).

After verification of the absence of outliers and normal distribution, data were statistically treated by mathematical Gaussian model. The repeatability contribution $U_{rep}(X)$ and its relative values $\dot{U}_{rep}(X)$ were calculated, taking into account the number of replicates which were obtained, by equation in Tab. 1.5 and are listed in Tab.2.10.

Tab. 2.10 Repeatability Uncertainty for YREE, Zr and Hf

	X pg/mL	n	$U_{rep}(X)$	$\dot{U}_{rep}(X)$
Y	20.084	8	0.263	0.0131
Zr	14.936	7	0.326	0.0218
La	21.052	6	2.622	0.1246
Ce	20.243	8	0.435	0.0215
Pr	21.062	9	0.256	0.0121
Nd	20.949	9	0.297	0.0142
Sm	21.125	6	0.114	0.0054
Eu	21.054	8	0.253	0.0120
Gd	21.423	8	0.332	0.0155
Tb	21.178	8	0.267	0.0126
Dy	20.935	9	0.249	0.0119
Ho	21.071	8	0.255	0.0121
Er	21.178	8	0.275	0.0130
Tm	21.058	7	0.269	0.0128
Yb	20.576	9	0.234	0.0114
Lu	21.111	7	0.286	0.0135
Hf	20.770	9	0.290	0.0140

Recovery uncertainty

The t test, applied on the results obtained from the spiked solutions, showed that for most of the analytes recovery is not unitary. In this case, the analyst can choose to correct or not the data for recovery. I decided to not apply the correction factor for recovery because the difference was not significant. When recovery is significantly different from 1, recovery uncertainty cannot be included in repeatability contribution.

To get a better estimate of the measurand, it is necessary to consider the contribution resulting from recovery uncertainty, U_{rec} . In this contribution, calculated according equation

in Tab 1.5, standard deviations and number of replicates obtained through trueness evaluation, along with the standard deviations of reference material used to spike solutions, are taken into account. Also this contribution, shown in Tab. 2.11, will be included in the final formula for calculating the combined uncertainty.

Tab. 2.11 Recovery Uncertainty for YREE, Zr and Hf

	X pg/mL	Sr	n	U_{rec}	\dot{U}_{rec}
Reference Material	19.92	0.3107	∞		
Y	20.084	0.743	8	0.407	0.0194
Zr	14.936	0.863	7	0.450	0.0259
La	21.052	6.424	6	2.641	0.0928
Ce	20.243	1.230	8	0.534	0.0235
Pr	21.062	0.767	9	0.402	0.0188
Nd	20.949	0.891	9	0.430	0.0197
Sm	21.125	0.279	6	0.331	0.0155
Eu	21.054	0.715	8	0.401	0.0189
Gd	21.423	0.938	8	0.454	0.0209
Tb	21.178	0.756	8	0.410	0.0193
Dy	20.935	0.746	9	0.398	0.0188
Ho	21.071	0.722	8	0.402	0.0190
Er	21.178	0.777	8	0.415	0.0195
Tm	21.058	0.712	7	0.411	0.0194
Yb	20.576	0.703	9	0.389	0.0188
Lu	21.111	0.756	7	0.422	0.0199
Hf	20.770	0.871	9	0.425	0.0204

Reference Material

To evaluate this contribution, all labware used to prepare calibration standards and the uncertainty of reference material declared by the supplier company must be taken into account. Calibration standards were daily prepared by stepwise dilution of the multi-element stock standard solution ($1000 \pm 5 \mu\text{g/mL}$).

For each element, the absolute uncertainty of stock standard solution, assuming rectangular distribution, is given by:

$$U_{ref} = \frac{1000 \mu\text{g} / \text{mL}}{\sqrt{3}} \quad \text{Eq. 24}$$

The subsequent step was to evaluate the contribution of the uncertainty of labware for the preparation of the calibrating solutions.

From stock standard solution, a 1 $\mu\text{g/mL}$ and 1 ng/mL intermediate solutions were prepared by two successive dilutions. Through the 1 ng/mL dilution, all calibrating solutions were prepared in the range 2.5 – 500 pg/mL . To assess the contribution of the reference material towards combined uncertainty, I evaluated the dilution process to obtain the 1 $\mu\text{g/mL}$ and 1 ng/mL solutions, and the preparation of the 2.5 pg/mL and the 500 pg/mL solutions like those. In Tab. 2.12 used labware and their respective variability are summarized.

Tab. 2.12 Reference Material contribution to combined uncertainty

	Unit	Quantity	Declared variability	U_{ref}	\dot{U}_{ref}
Stock solution	$\mu\text{g/mL}$	1000	± 5	2.88675	0.002887
I dilution					
Flask class A	mL	50	± 0.06	0.03464	0.000693
pipette	mL	0.05	± 0.0003	0.00017	0.003464
II dilution					
Flask class A	mL	50	± 0.06	0.03464	0.000693
pipette	mL	0.05	± 0.0003	0.00017	0.003464
III dilution					
Flask class A	mL	10	± 0.07	0.04041	0.004041
pipette	mL	0.025	± 0.0002	0.00012	0.004619
IV dilution					
Flask class A	mL	10	± 0.07	0.04041	0.004041
pipette	mL	5	± 0.05	0.02887	0.005774

For each step relative uncertainty was evaluated by applying the law of propagation of the errors; finally, all contributions were added to obtain the contribution of reference material (Eq.25, Tab 2.13) that was included in the final formula for combined uncertainty.

$$\dot{U}_{Ref} = \sqrt{\dot{U}_{mast.s \tan d}^2 + \dot{U}_{Idil}^2 + \dot{U}_{IIdil}^2 + \dot{U}_{IIIdil}^2 + \dot{U}_{IVdil}^2} \quad \text{Eq. 25}$$

Tab. 2.13 Reference Material uncertainty

	Unit	Quantity	\dot{U}_{i_ref}
master standard	µg/mL	1000	0.002887
I dilution	µg/mL	1	0.003533
II dilution	ng/mL	1	0.003533
III dilution	pg/mL	2.5	0.006137
IV dilution	pg/mL	500	0.007047
\dot{U}_{Ref}			0.010983

Instrumental calibration uncertainty

As described in section 2.2, the statistical test of regression applied for assessing the linearity and working range were positive. Specifically, the Mandel's test was positive, indicating that there was a statistically linear relationship; the analysis of residual was acceptable, and the test on the slope and the intercept was positive.

I calculated the parameters used to assess the contribution of regression function towards measurement uncertainty. The contribution due to instrumental calibration quantifies the dispersion of experimental points along the calibration line. It is quantified applying the following equation

$$s_{cal} = \frac{s_{y/x}}{b} \sqrt{\frac{1}{m} + \frac{1}{n} + \frac{(y_i - \bar{y})^2}{b^2 \sum (x_i - \bar{x})^2}} \quad \text{Eq. 26}$$

Where **b** is the slope of calibration curve, **m**, equal to 1, is the number of replicates of the sample, **n** equal to 9 is the number of calibrating solution, **y_i** and **ȳ** are the signal and the mean value in cps, obtained from replicates during repeatability study, **x_i** and **ȳ** are the concentration of each level of calibration solutions and the mean value respectively, **s_{y/x}** is the standard deviation of residual calculated according Eq. 27

$$s_{y/x} = \sqrt{\frac{\sum_i y_i^2 - \left(\sum_i y_i\right)^2 \cdot (n-2)}{n - b \cdot \left(\sum_i x_i y_i - \sum_i x_i \sum_i y_i / n\right)}} \quad \text{Eq. 27}$$

where **x_i** and **y_i** are the concentration and the instrumental signal of calibration curve.

By applying the Eq. 26, the calibration uncertainty values (**s_{cal}**) were as many as the number of replicates performed to repeatability evaluation; the average of these values provides the average calibration uncertainty, **u_{cal} (x_m)**. The relative calibration uncertainty, **Ū_{cal}(x)**, was obtained dividing the average calibration uncertainty for the mean value **ȳ**, in pg/mL, obtained by performing repeatability evaluation (Eq. 28). In Tab. 2.14 calibration uncertainty and all parameters required to its calculation are listed.

$$u_{cal}(x_m) = \sqrt{\frac{\sum S_{cal}^2}{n^2}} \quad \text{Eq. 28}$$

Tab. 2.14 Instrumental calibration uncertainty

analyte	$S_{y/x}$	$\sum (x_i - \bar{x})^2$	\bar{y}	n	$\sum S_{cal}^2$	$U_{cal}(x)$	$\dot{U}_{cal}(x)$
Y	0.01765	216347.2	5.472	8	11.326	0.4207	0.00121
Zr	0.01575		1.643	7	67.231	1.1714	0.00407
La	0.04631		8.601	6	32.729	0.9535	0.00203
Ce	0.02970		7.752	8	21.289	0.5767	0.00153
Pr	0.03031		8.500	9	15.388	0.4359	0.00126
Nd	0.00900		1.586	9	41.889	0.7191	0.00203
Sm	0.00448		1.368	6	9.349	0.5096	0.00143
Eu	0.01783		4.355	8	20.201	0.5618	0.00164
Gd	0.01183		2.003	8	43.235	0.8219	0.00233
Tb	0.03571		9.779	8	16.131	0.5020	0.00145
Dy	0.00941		2.431	9	18.135	0.4732	0.00138
Ho	0.03175		9.701	8	13.004	0.4508	0.00131
Er	0.01346		3.294	8	20.140	0.5610	0.00162
Tm	0.03198		10.269	7	11.868	0.4921	0.00143
Yb	0.00887		2.241	9	18.148	0.4733	0.00141
Lu	0.02383		10.129	7	6.745	0.3710	0.00108
Hf	0.01102		2.808	9	17.613	0.4663	0.00138

Pre-concentration uncertainty

To assess pre-concentration uncertainty, the contribution coming from V_{HCl} , Dil. Fact. and V_{sample} , indicated in Eq.26, should be evaluated. All these parameters can be merged into pre-concentration factor. Each parameter was evaluated as described for reference material taking into account all labware used and finally adding them to obtain pre-concentration uncertainty (Tab.2.15).

Tab. 2.15 Pre-concentration uncertainty

	Unit	Quantity	Declared variability	U	\dot{U}	\dot{U}
V HCl						
pipette	mL	10	0.05	0.02887	0.002887	0.002887
Dil.fact						
pipette	mL	5	0.05	0.02887	0.005774	
pipette	mL	1	0.005	0.00289	0.002887	0.006455
V sample						
cylinder	mL	1000	4	2.30940	0.002309	0.002309
\dot{U}_{prec}					0.007439	0.007439

Calculation of combined uncertainty

Before applying the general formula of propagation of uncertainties, it was necessary to correct the repeatability contribution for a correction factor which takes into account the number of replicates performed for the determination of the unknown sample.

Since the repeatability was calculated by repeating the measurement 9 times, while the unknown sample was repeated only once, the contribution given by repeatability must be corrected for a correction factor obtained by the following expression:

$$\left[\dot{U}_{rep}(X) \right]_n = \dot{U}_{rep}(X) \sqrt{\frac{N}{m}} \quad \text{Eq. 29}$$

where **N** is the number of replicates and **m** the replicates performed for the determination of the unknown sample.

This correction is necessary because the contribution given by repeatability was calculated using the standard deviation of the mean, which is significantly smaller than the standard deviation obtained from a single measure replicated.

The same correction is necessary for the contribution of the instrumental calibration.

After quantifying all contributions to the uncertainty of measurement, these were combined according to Eq. 15.

Tab. 2.16 shows mean values, standard deviations expressed in pg/mL, repeatability, recovery, reference material, calibration and pre-concentration contributions. In the last three columns relative, absolute and percentage combined uncertainty are shown.

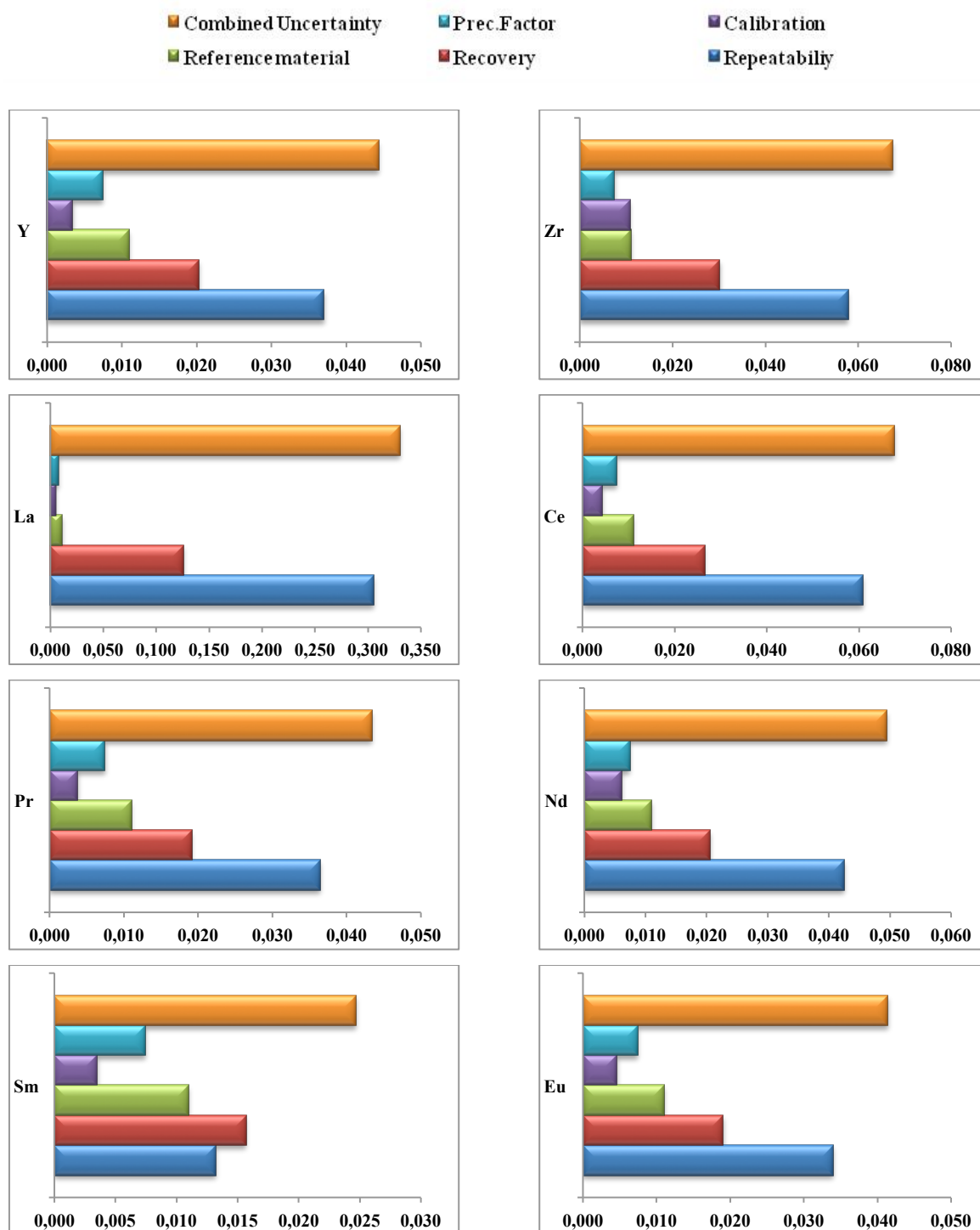
Tab. 2.16 Contributions to combined uncertainty

	X	Sr	n	$[\dot{U}_{Rep}(X)]_n$	\dot{U}_{rec}	U_{Ref}	$[\dot{U}_{cal}(X)]_n$	\dot{U}_{prec}	\dot{U}_C	U_C	$\% U_C$
Y	20.08	0.74	8	0.037008	0.020262	0.01098	0.003423	0.007439	0.044360	0.89	4.44
Zr	14.94	0.86	7	0.057755	0.030154	0.01098	0.010779	0.007439	0.067358	1.01	6.74
La	21.05	6.42	6	0.305138	0.125443	0.01098	0.004979	0.007439	0.330221	6.95	33.02
Ce	20.24	1.23	8	0.060755	0.026401	0.01098	0.004325	0.007439	0.067697	1.37	6.77
Pr	21.06	0.77	9	0.036411	0.019103	0.01098	0.003769	0.007439	0.043369	0.91	4.34
Nd	20.95	0.89	9	0.042537	0.020519	0.01098	0.006102	0.007439	0.049433	1.04	4.94
Sm	21.12	0.28	6	0.013206	0.015665	0.01098	0.003499	0.007439	0.024658	0.52	2.47
Eu	21.05	0.71	8	0.033954	0.019024	0.01098	0.004630	0.007439	0.041378	0.87	4.14
Gd	21.42	0.94	8	0.043770	0.021209	0.01098	0.006593	0.007439	0.050844	1.09	5.08
Tb	21.18	0.76	8	0.035688	0.019350	0.01098	0.004115	0.007439	0.042906	0.91	4.29
Dy	20.93	0.75	9	0.035622	0.019007	0.01098	0.004136	0.007439	0.042700	0.89	4.27
Ho	21.07	0.72	8	0.034281	0.019087	0.01098	0.003713	0.007439	0.041584	0.88	4.16
Er	21.18	0.78	8	0.036711	0.019589	0.01098	0.004585	0.007439	0.043914	0.93	4.39
Tm	21.06	0.71	7	0.033829	0.019524	0.01098	0.003784	0.007439	0.041423	0.87	4.14
Yb	20.58	0.70	9	0.034188	0.018918	0.01098	0.004223	0.007439	0.041479	0.85	4.15
Lu	21.11	0.76	7	0.035812	0.019996	0.01098	0.002856	0.007439	0.043202	0.91	4.32
Hf	20.77	0.87	9	0.041925	0.020472	0.01098	0.004138	0.007439	0.048681	1.01	4.87

The evaluation of combined measurement uncertainty by metrological approach allowed me to highlight the critical stages of the determination through extraction/pre-concentration procedure of ultra trace YREE, Zr and Hf in a high salt matrix by co-precipitation on $\text{Fe}(\text{OH})_3$. The percentage combined uncertainty for all elements is below 5% except for La that show $\%U_C$ equal to 33%. Graphical representation of each contribution to combined uncertainty (Fig. 2.3) indicates that the critical stages of the process are the

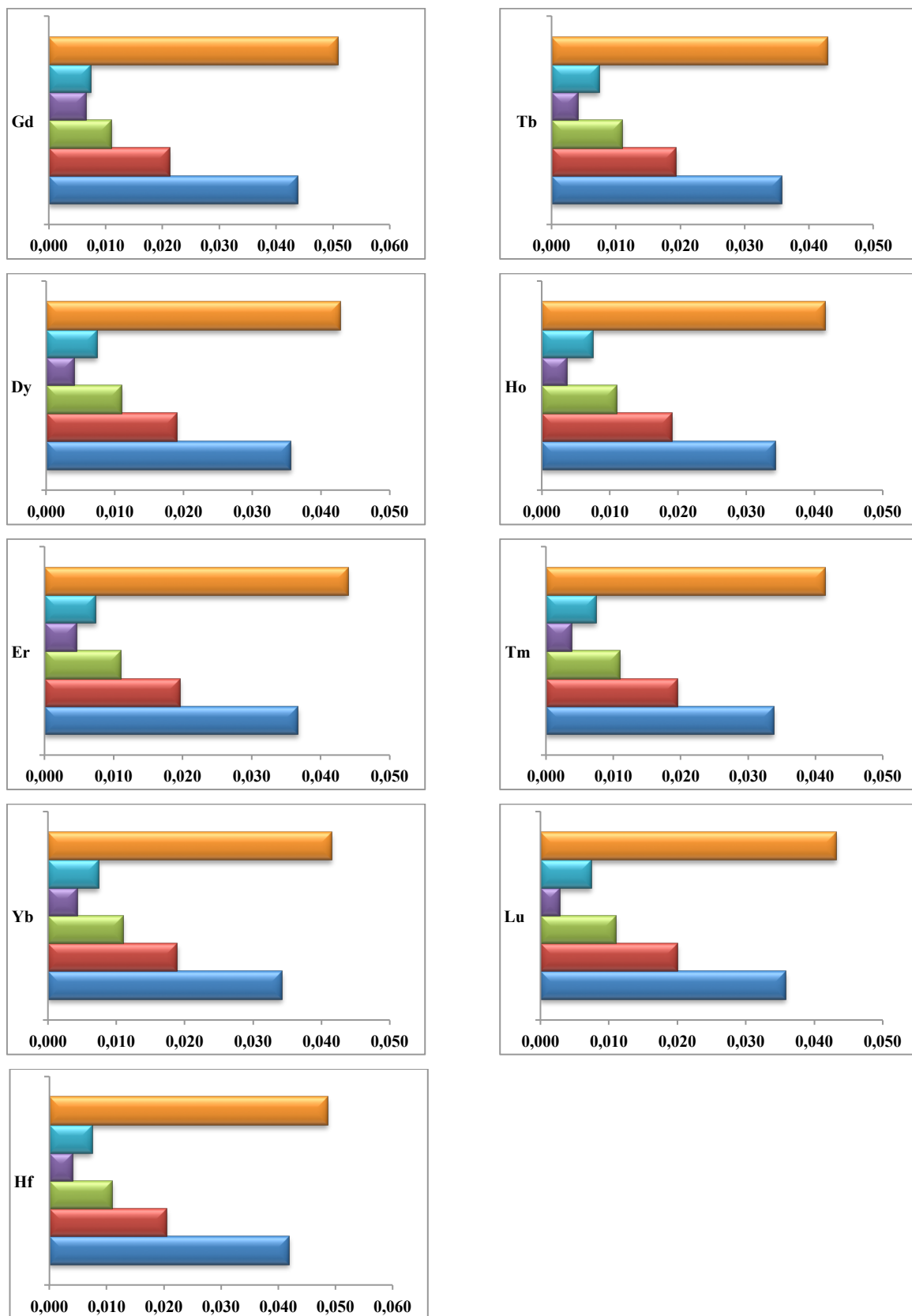
repeatability and recovery, while calibration, reference material and pre-concentration have lower influence on the assessment of combined uncertainty.

Fig. 2.3 Graphical representation of contributions to relative combined uncertainty



continued on next page

Fig. 2.3 (Continued)



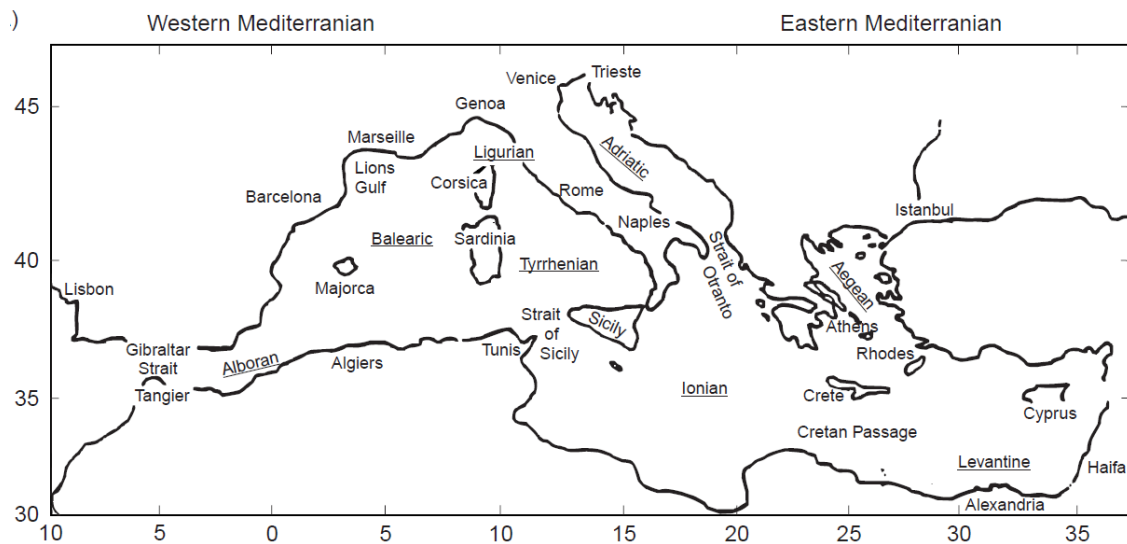
Chapter 3: Investigated Geochemical Systems

3.1. Seawater under oceanic condition and deep hypersaline basin

3.1.1. Seawater under oceanic conditions: Eastern Mediterranean Sea

The Mediterranean Sea is an enclosed basin connected to the Atlantic Ocean by the narrow and shallow Strait of Gibraltar. It is composed of two similar size basins, a Western one and a Eastern one, connected by the Strait of Sicily. The Eastern Mediterranean has a more complicated structure than the Western, with a much more irregular, complex topography constituted by a succession of deep valleys, ridges, and localized pits.

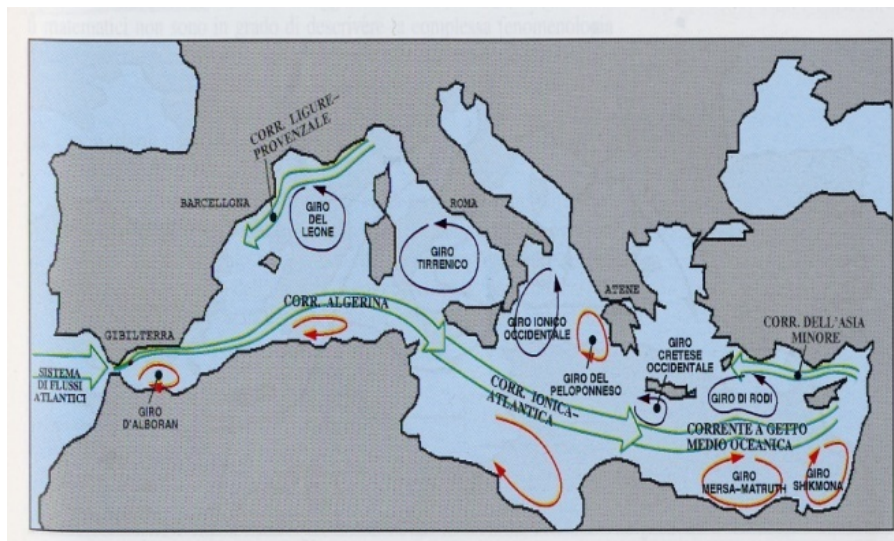
Fig. 3.1 Morphology of the Mediterranean Sea: geography of the basins



Four sub-basins (or seas) can be defined in the Eastern Mediterranean (Fig. 3.1): the Ionian, the Levantine, the Adriatic, and the Aegean. The Ionian Sea is the deepest in its central part, ending in the shallow Gulf of Sirte at its southernmost end. The Cretan passage leads from the Ionian into the Levantine basin, which reaches its maximum depth in a localized depression south-east of the island of Rhodes.

The hydrology and circulation of the Mediterranean Sea have been overall known for some time. For instance, it is well known that both Mediterranean basins, the Western and the Eastern, are evaporation basins (lagoons), with freshwater fluxing from the Atlantic through the Gibraltar Straits and into the Eastern Mediterranean through the Sicily Strait. The Atlantic Water (AW) mass ($S = 36.15$ PSU and temperature $T = 15.3^{\circ}\text{C}$) entering through Gibraltar increases in density because the evaporation exceeds the precipitation and becomes Modified Atlantic Water (MAW) in its route to the Levantine basin. At the Sicily Strait, the saltier MAW has a salinity $S \leq 37.5$ PSU reaching a maximum of $S < 38.9$ PSU in the Levantine basin. Here in its northern part, winter cold, dry winds blowing from the mainland under surface cooling and evaporative fluxes lead to the formation of Levantine Intermediate Water (LIW) which has $39.0 \leq S \leq 39.2$ PSU and potential temperature (θ) between 15°C and 16°C at the formation sites, the most important of which is the well-known Rhodes gyre. The LIW return route is westward in the layer between 200 and 600m depth. At the Gibraltar Strait LIW it is diluted to $S \leq 38.5$ PSU, and spreads out in the North Atlantic, becoming Upper North Atlantic Intermediate Water (Fig. 3.2).

Fig. 3.2 Schematic representation of the upper thermocline circulation



3.1.2. Eastern Mediterranean deep hypersaline basins

The discovery of anoxic basins in the eastern Mediterranean Sea occurred in the early 80's, during a cruise of the Dutch R/V Tyro (1983) and the Italian R/V Bannock that aimed at studying seismology, micropaleontology and geochemistry of Mediterranean sea.

The discovered basins, named Bannock and Tyro appeared to be filled with NaCl saturated anoxic brines, formed by dissolution of outcropping or underlying Messinian evaporites (Camerlenghi, 1990). Bannock Basin is located west of Crete while Tyro Basins is located south of Crete.

At both basins, an extremely sharp interface separates oxygenated Mediterranean waters from anoxic brines with salinity one order of magnitude higher than normal seawater.

Across this interface, many chemical and physical parameters decrease or increase dramatically over less than 1 m. The sharp density gradient effectively prevents downward mixing of oxygen (Schijf et al., 1995).

Although Bannock and Tyro are filled with anoxic brines of similar origin, they show several significant differences. Tyro basin, located near Strabo Trench at the southern boundary of the Hellenic Trench system is a pull-apart basin and its formation is thus unrelated to the presence of evaporites. The process that formed Bannock basin, located near the Syrtic abyssal Plain on the southern edge of the Mediterranean ridge, is directly related to the presence of evaporites and is also the origin of the so called “cobblestone topography” that characterise the general area. Due to their different formation histories, the morphology of the two basins is different. In the Tyro area only a single basin containing anoxic brine was found, whereas the Bannock area consists of several different sub-basins.

According to several authors (Bregant et al., 1990; de Lange et al., 1990a, 1990b) brines from Tyro and Bannock basins have different compositions, probably because derived from evaporitic rocks of different compositions. The Bannock brine was formed by

dissolution of late stage evaporites, whereas Tyro brine was formed by dissolution of early stage evaporitic horizons. In both cases brine chemistry highlights the occurrence of secondary alteration processes. In Bannock alteration of original brine structure allowed formation a distinct two-layered structure, each layer having a slightly different chemical composition. On the contrary, in the Tyro brine no multi-layered structure was observed.

3.1.3. Seawater and brines collection and storage

Seawater and brine samples of Eastern Mediterranean Sea for the determination of YREE, Zr and Hf were collected in September 2008 during scientific cruise on RV Urania devoted to exploration of the genomic richness of deep hypersaline anoxic lakes.

Sample were collected using method developed by Bruland et al., (1979). Seawater was collected in 12 l Niskin bottles with barometric opening at 5-10 m depth to avoid the contamination from the surface layer.

The sampling system consists of a circular structure where Niskin bottles are located. This structure is completed by a multiparametric probe SBE 911 SEA-BIRD ELECTRONICS CTD Inc. (Fig. 3.3). The heart of the instrumentation is a multi-channel logger which can capture different analogical signals. The sensors are located in a metal structure that is submerged in water, while the acquisition system is located in the ship laboratory. The connection between sensors and data acquisition card is made through a serial shielded cable. The probe contains sensors measuring temperature, conductivity, pressure, light transmission, salinity and dissolved oxygen. Data acquisition requires that the CTD multiparametric probe is immersed in the sea and sent down at a nearly constant velocity until the possible maximum depth. The condition of constant rate of descent is not sufficient to ensure proportionality between the real depth of the probe and fall time. It must be remembered that waves can roll the ship and, consequently, the absolute depth of the probe can remain constant only for a certain period of time. In this case, since the sampling frequency (24 Hz) is constant, will be

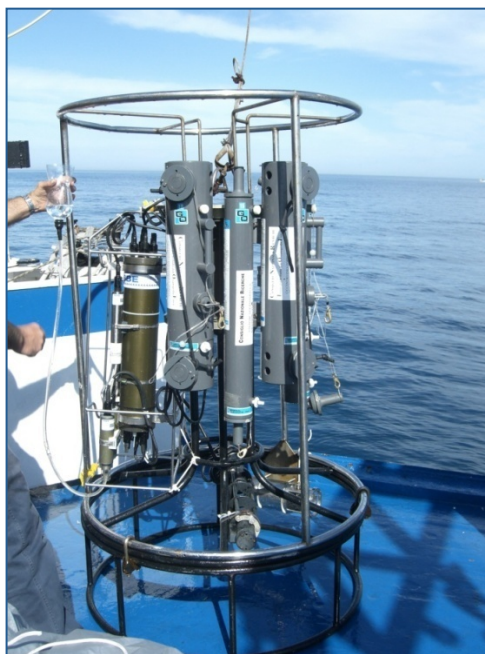
sampled at the same point values. This problem can be solved only during data post-processing.

Seawater samples were collected during the ascent and were chosen on the basis of physical-chemical parameters recorded during the descent. Samples were carefully taken from the Niskin bottles and stored in polyethylene bottles for laboratory analysis.

The samples were filtered through acid-cleaned 47 mm, 0.45 μm nitrocellulose membrane filters (Millipore Corporation), acidified to pH 2 with HNO_3 and stored until analytical determination by co-precipitation onto $\text{Fe}(\text{OH})_3$ as described in section 2.2.1.

To apply the validated method, brine sample were diluted with ultrapure water (dilution factor 10) before co-precipitation, to obtain a concentration similar to seawater.

Fig. 3.3 Sampling instrumentation



Seawater was collected from Bannock basin (sampling points named KRYOS and THETIS), brine samples were collected from Bannock and Tyro basins (sampling points named THETIS, MEDEA, and TYRO) as shown in Fig. 3.4.

Fig. 3.4 Sampling points

3.1.4. Hydrography

3.1.4.1. Oceanographic and physical-chemical characterization of seawater and basins

Physical chemical parameters of Kryos ($34^{\circ}57'N$ $22^{\circ}05'E$), Thetis ($34^{\circ}40'N$ $22^{\circ}08'E$), Medea ($34^{\circ}24'N$ $22^{\circ}27'E$) and Tyro basins ($33^{\circ}52'N$ $26^{\circ}02'E$) are shown in appendix A.

Kryos

Kryos seawater samples were collected along the water column, from surface to 3238m below the sea level. Physical structure of water body was followed according to variations of physical-chemical parameters measured during sample collections. From 25 to 200 m below the sea level, the temperature slowly decreased from $19.8^{\circ}C$ to $15.3^{\circ}C$ allowing to locate the thermocline, while density increased from 1027.93 g/L to 1029.94 g/L . Salinity values were those typical of Mediterranean sea (higher than 38‰); the seawater layer between

100 and 500 showed high salinity values (close to 39 ‰) that allowed us to identify the occurrence of Levantine Intermediate Water (LIW).

Thetis basin

The seawater-brine interface was found at 3258 m below the sea level and the brine thickness estimated at about 157 m. The temperature at seawater-brine interface was 13.98°C and slowly increased to 15.05 °C downward to the seabed. At the interface seawater-brine, conductivity and salinity sharply increased reaching values of about three times the average values of sea water. Conductivity ranged from 46.7 mS/cm to 148.9 mS/cm and salinity from 39.05 PSU to 152.95 PSU. The brine Thetis basin had a total salt concentration of 338 g/L; density increase from 1043.5 to 1132.7 Kg/m³. Dissolved oxygen sharply decrease, within less than 1 m from 5.66 mL/L to 2.84 mL/L and as a consequence the redox potential decreased from +213 mV to -340mV indicating the presence of highly reduced environment in the lower layer of the brine basin.

Medea basin

The seawater-brine interface was found at 2919 m below the sea level and the brine thickness estimated at about 170 m. The temperature at seawater-brine interface was 13.90°C and slowly increased to 15.42°C downward to the seabed. At the interface seawater-brine, conductivity and salinity sharply increased reaching values of about three times the average values of sea water. Conductivity ranged from 50.8 mS/cm to 150.0 mS/cm and salinity from 41.49 PSU to 156.72 PSU. The brine Thetis basin had a total salt concentration of 367 g/L; density increased from 1043.6 to 1134.8 Kg/m³. Dissolved oxygen sharply decreased, within less than 1 m from 5.59 mL/L to 2.74 mL/L and as a consequence the redox potential decreased from +200 mV to -316 mV indicating the presence of high reduced environment in the lower layer of the brine basin.

Tyro basin

The seawater-brine interface was found at 3325 m below the sea level and the brine thickness estimate about 105 m. The temperature at seawater-brine interface was 14.05°C and slowly increased to 14.18°C downward to the seabed. At the interface seawater-brine, conductivity and salinity sharp increased reaching values of about three times the average values of sea water. Conductivity ranged from 51.9 mS/cm to 157.4 mS/cm and salinity from 42.92 PSU to 167.4 PSU.

The brine Thetis basin had a total salt concentration of 328 g/L; density increased from 1047.6 to 1146.8 Kg/m³. Dissolved oxygen sharply decreased, within less than 1 m from 5.53 mL/L to 2.55 mL/L and as a consequence the redox potential decreased from +199 mV to -288 mV indicating the presence of high reduced environment in the lower layer of the brine basin.

3.1.5. Results

3.1.5.1. Kryos seawater

The concentrations of Zr, Hf, and YREE along the water column of Kryos basin, expressed in pmol/L are listed in Tab. 3.1 and shown in Fig. 3.5.

From vertical distribution it was possible to observe that the upper water layer (from 25 to 75 m) was characterised by a decrease of all investigated elements. Major differences in vertical distribution was observed in the water layer between 200 to 1500 m; for most of the elements a large variability was present; in particular, vertical profile was characterized by a maximum between 500 and 750 m and a minimum at 1500 m below the sea level. This large variability may be related to the presence of thermocline region that, according to physical-chemical parameters, extends from 200 to 1000 m water depth and that is characterized in Mediterranean Sea by the presence of Levantine Intermediate Water. Observed YREE, Zr and

Hf variations in the bottom water layer (from 1500 to 3238 m) were mainly within the uncertainty of measure.

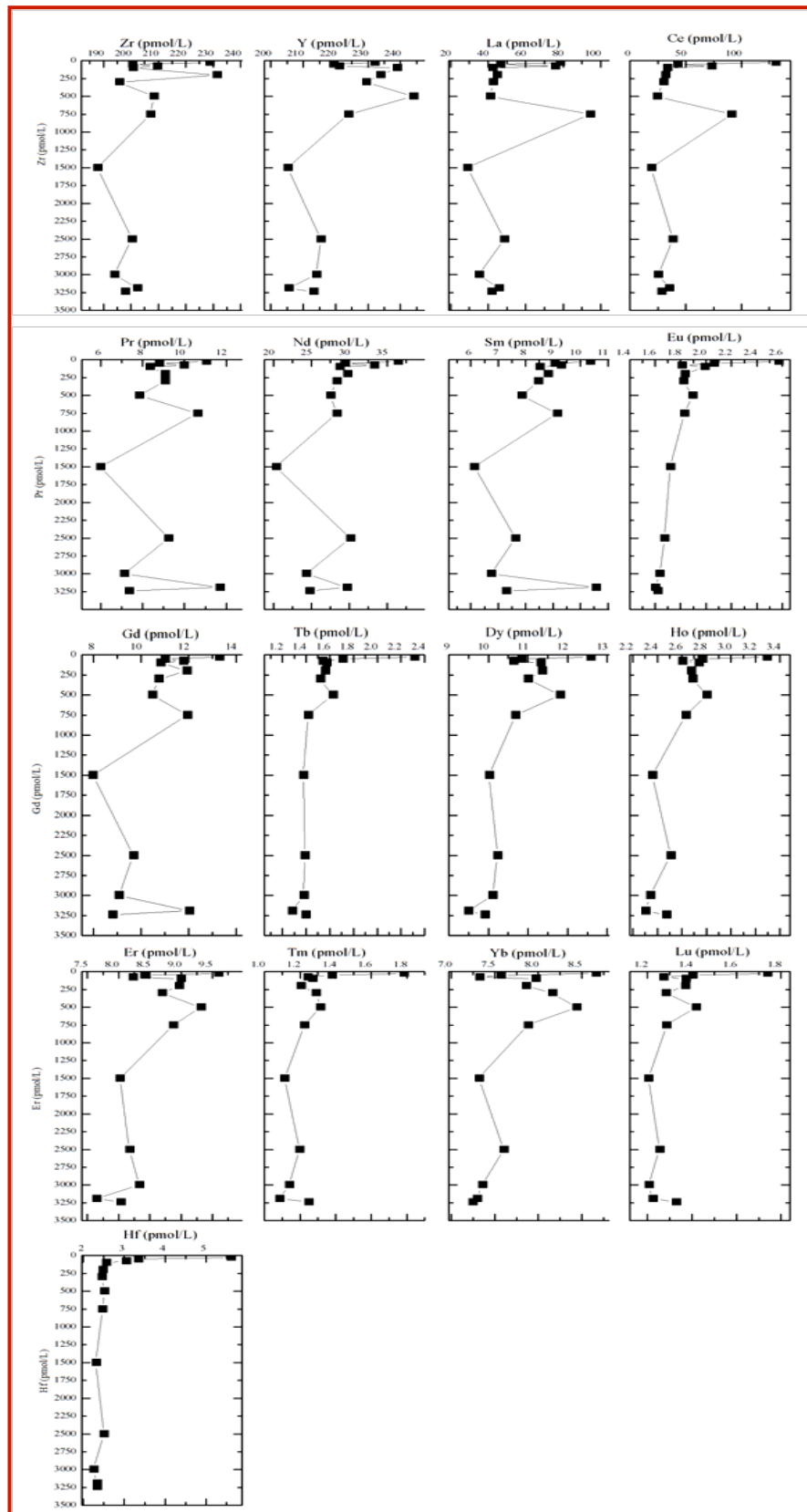
Tab. 3.1 YREE, Zr and Hf concentration (pmol/L) in Kryos seawater column

depth (m)	Zr	Y	La	Ce	Pr	Nd	Sm	Eu	Gd	Tb	Dy	Ho	Er	Tm	Yb	Lu	Hf
25	229	232	78	131	11.0	36	10.4	2.57	13.3	2.31	12.6	3.3	9.6	1.78	8.7	1.74	5.6
50	200	219	47	42	8.8	29	9.1	2.06	11.0	1.71	10.8	2.8	8.4	1.38	7.6	1.40	3.3
75	210	221	76	73	10.0	33	9.3	1.81	11.8	1.54	10.6	2.6	8.2	1.24	7.3	1.27	3.0
100	201	239	42	33	8.4	29	8.5	1.99	10.8	1.57	11.3	2.7	9.0	1.27	8.0	1.37	2.6
200	231	234	45	32	9.1	30	8.8	1.83	11.9	1.56	11.4	2.7	9.0	1.20	7.9	1.37	2.5
300	196	229	43	30	9.1	28	8.5	1.82	10.7	1.52	11.0	2.7	8.7	1.29	8.2	1.28	2.4
500	208	244	41	24	7.8	28	7.9	1.89	10.5	1.62	11.8	2.8	9.3	1.31	8.4	1.42	2.5
750	207	224	94	91	10.6	28	9.1	1.83	11.9	1.42	10.7	2.6	8.9	1.22	7.9	1.28	2.5
1500	188	205	29	19	6.0	20	6.1	1.72	8.0	1.38	10.0	2.4	8.0	1.11	7.3	1.20	2.3
2500	200	215	48	38	9.2	30	7.6	1.67	9.7	1.39	10.2	2.5	8.2	1.20	7.6	1.25	2.5
3000	194	214	35	25	7.1	24	6.7	1.64	9.1	1.38	10.1	2.3	8.3	1.14	7.4	1.21	2.2
3190	202	205	46	35	11.7	30	10.6	1.60	12.0	1.28	9.5	2.3	7.6	1.08	7.3	1.22	2.3
3238	198	213	42	28	7.4	25	7.3	1.62	8.8	1.40	9.9	2.5	8.0	1.25	7.2	1.33	2.3

Largest yttrium concentrations along the water column attain to the maximum value (244 ± 10 pmol/L) close to the thermocline region at 500 m water depth, whereas the minimum (205 ± 9 pmol/L) was observed at 1500 m water depth.

On the contrary Ho shows a more homogeneous vertical profile, characterized by decreasing concentrations from shallow waters (3.28 pmol/L to 2.6 pmol/L in the first 50 m), to 1500 m water depth (2.7 ± 0.1 pmol/L), followed by a further slight decrease reaching the deepest water layer (2.4 ± 0.1 pmol/L).

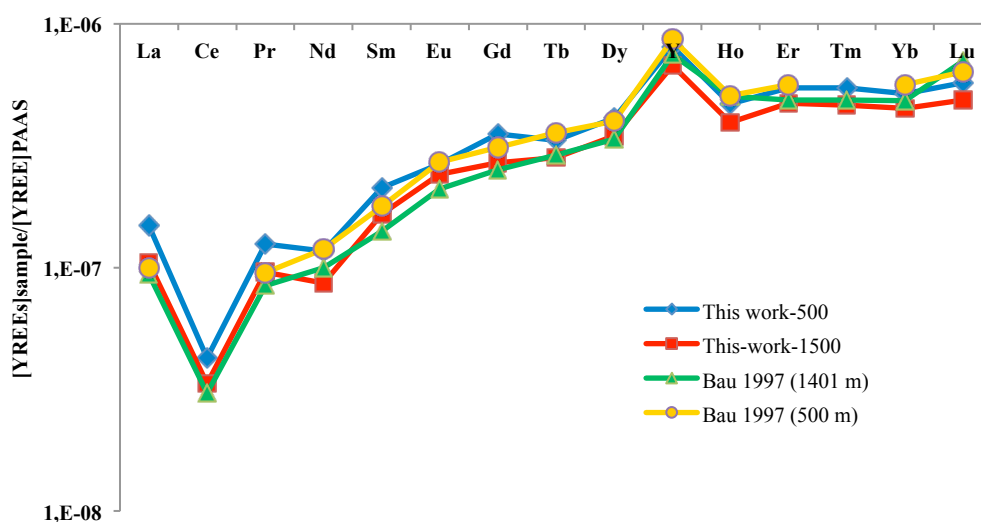
Fig. 3.5 Vertical distribution of YREE, Zr and Hf in Kryos basin



Zirconium concentration decreased from 228 ± 15 pmol/L to 200 ± 13 pmol/L in the first 50 m and showed slight variation along the water column (200 ± 7 pmol/L), except for a 231 ± 15 pmol/L maximum value registered at 200 m probably due to the presence of thermocline. Vertical profile of Hafnium concentrations were largest in shallowest waters (5.61 ± 0.27 pmol/L). Therefore Hf content progressively decreased to 2.56 ± 0.12 pmol/L along the first 100 m below the sea level, but then it remained constant until the deepest water layer. These features are in agreement with a terrigenous origin of Hf, as corroborated by the highest Zr and Hf concentrations recorded in coastal sampling stations (Godfrey et al., 2008 and reference therein).

By comparing the above mentioned data with those reported for YREE concentrations in Eastern Mediterranean Seawater (Bau et al., 1997; Schijf et al., 1995) large similarities can be observed. Despite sampling location and collection depth were different, good agreement is shown between our data measured at 500 m and 1500 m below the sea level and values analysed in LIW and EMDW by Bau (1997), collected at 500 m and 1401 m respectively (Fig. 3.6).

Fig. 3.6 PAAS normalised YREE pattern of LIW and EMDW

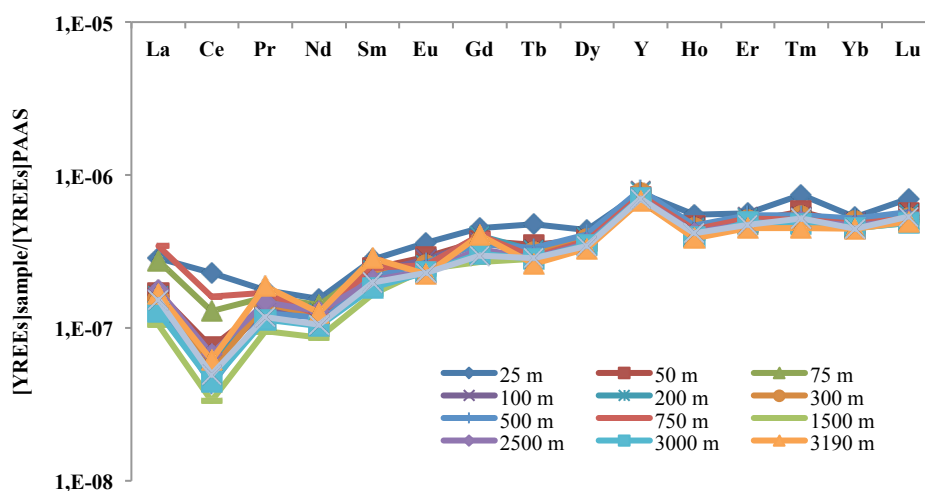


Observed differences were less than 10 % in LIW samples for all elements apart from La, Pr, Sm that are respectively 50 %, 31% and 19 % more concentrated. In EMDW sample these differences are less than 10 %, except for Lu (30%). The above mentioned similarities allowed us to identify samples collected at 500 and 1500 m as representative of LIW and EMDW, respectively.

Unfortunately further comparisons cannot be carried out due to the lack of knowledge of YREE content in shallowest waters from the same area because both Bau et al. (1997) and Schijf et al. (1995) did not investigate those waters. Concentrations of LREE in deepest water layer are higher than those analysed by Bau et al., (1997).

To highlight the distribution of YREE, Fig. 3.7 shows the rare earth pattern normalized to PAAS (post-Archean shale).

Fig. 3.7 PAAS normalised YREE pattern along the Kryos water column



To evaluate features of YREE patterns and processes occurring along the water column, elemental anomalies were evaluated according to the following expression:

$$\frac{[REE_i]}{[REE_i]^*} = \frac{2 \cdot [REE_i]_n}{[REE_{i-1}]_n + [REE_{i+1}]_n} \quad \text{Eq. 30}$$

(Alibo and Nozaki, 1999). The anomaly value is calculated as ratio between normalized measured concentrations in the sample and the estimated concentrations of the preceding (i-1) and following (i +1) investigated element.

The presence of these anomalies in YREE distribution in geochemical systems are usually justified by crystallographic reasons, being mainly typical of Eu behaviour during feldspar crystallization. On the contrary, in dissolved pool Ce behaviour is influenced by oxidative occurring conditions. Thus, the higher stability of Ce^{IV} with respect to Ce^{III}, in the oxic waters and in systems in equilibrium with the atmosphere, leads to negative Ce anomalies induced by Ce removal from dissolved phase as insoluble CeO₂, directly precipitated or scavenged onto Mn and/or Fe – oxide phase.

Reciprocal yttrium and holmium fractionations, described both in terms of Y/Ho molar ratio and as amplitude of yttrium anomaly, defined Y/Y* calculated placing Y between Dy and Ho in normalised sequence, usually occurs, suggesting that Y particle reactivity is noticeably lower than Dy and Ho involving an higher Y residence time in seawater with respect to those of its neighbors in the YREEs series (Bau et al., 1997).

Surface water samples showed the highest dissolved concentrations, indicating that the main YREE source is atmospheric dust particles falling on the shallowest water layer. This evidence is confirmed by Ce/Ce* values ranging from 0.99 in surface water to 0.36 in bottom waters, whereas Y/Y* progressively increase from 1.54 to 1.85 along the water column from swallow to bottom layers. As atmospheric dust progressively sinks along the water column, YREE are leached leading to their dissolved concentrations increase.

While all the other YREE are simply involved in dissolved complexation-surface complexation equilibria with authigenic particulate matter, Ce also shares to oxidation processes. Therefore, recognitions of Ce/Ce* values close to 1 in the shallowest waters, suggest that the kinetic of Ce oxidation is lower with respect to that of Ce release from atmospheric particulates. Additionally, Ho is not fully preferentially fractionated with respect to Y in shallow waters, probably because authigenic FeOOH particulate is not entirely formed.

A different evolution of Y/Y* values is observed in deepest seawater samples collected from 3000 to 3238 m water depth. Here Y/Y* ratios decrease progressively suggesting that conditions occurring along the seawater column changed. This process is probably a consequence of the reductive dissolution of authigenic FeOOH formed along the oxic seawater column at seawater-brine interface.

The occurrence of these YREE data by Bau et al. (1997) allows us to hypothesize a YREE flux from highly concentrated interface zone between oxic bottom water and deep-sea brine, from which LREE progressively dissolve upwardly.

The increase in concentration found with respect to samples collected in 1993 by Bau et al. (1997), could be explained by a slow diffusion, observable only on an extended time scale, from the more concentrated underlying brine towards above seawater. The above mentioned REE flux, that was invoked by Bau et al. (1997) from the interface to deepest seawater, is thus enriched in Ho rather than Y, thus explaining the observed Y/Y* values decrease. The observed enrichment in HREE compared to LREE in the studied samples is due to the progressive increase of stability of REE dissolved carbonate complexes along the elemental series.

For Zr and Hf distributions, there is no comparison with previous data collected in the Mediterranean. The few reference data (Boswell and Elderfield, 1988; Firdaus et al., 2008,

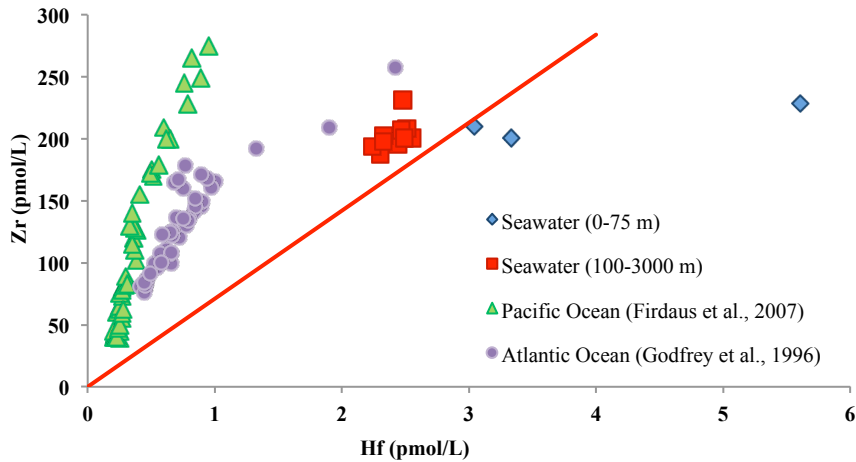
2011; McKelvey and Orians, 1998; Godfrey et al., 1996, 2008) reported dissolved concentrations between 30 and 300 pmol/L for Zr and between 0.1 and 1 pmol/L for Hf. Only Godfrey et al. (1996) found Hf concentrations up to 2.5 pmol/L in Atlantic Ocean. Higher value, up to 12 pmol/L were measured only in the Hudson estuary and attributed to lithogenic origin (Godfrey et al., 2008).

As previously mentioned analogies between our data and those reported by Bau et al. (1997) allowed us to define YREE signatures that can be extended to Zr and Hf contents that were not previously investigated both in LIW and in EMDW. These concentrations measured at 500 m depth and 1500 m allowed us to identify Zr and Hf concentrations in LIW of 208 pmol/L and 2.51 pmol/L, respectively, whereas the same values for EMDW were 187 pmol/L and 2.3 pmol/L for Zr and Hf, respectively.

Features of Zr/Hf molar ratio mainly changed between 25 and 200 m water depth sharply increasing from 40 to 94, due to the stronger Hf decrease than Zr (Tab. 3.1). Between 300 and 1500 m, Zr/Hf ratio reaches 83 ± 1 , slightly increasing to 86 ± 1 in deepest waters. Differences in Zr and Hf distributions along the water column mirror Zr and Hf sources (Fig. 3.8). We note that samples of seawater collected at depths greater than 75 m fall in a region of the plan Zr vs. Hf higher than the line with $Zr/Hf = 71$, representing the typical ratio of continental crust. In this sample, as mentioned before, the concentration varies only slightly, with a minimum at 1500 m (188 pmol/L and 2.4 pmol/L for Zr and Hf) and a modest increase at 3200 m. By comparing our data with those reported by Godfrey et al. (1996) from Atlantic Ocean and by Firdaus et al. (2007) from Pacific Ocean, we can see that waters collected under more "oceanic" environments, fall along linear trends with larger slopes, whereas samples from shallowest waters and/or collected more closely to coastlines, are clustered around linear trends with lower slopes. In particular, our samples, that were collected in an epicontinental context, are greatly affected from lithogenic inputs and, consequently, fall close to the

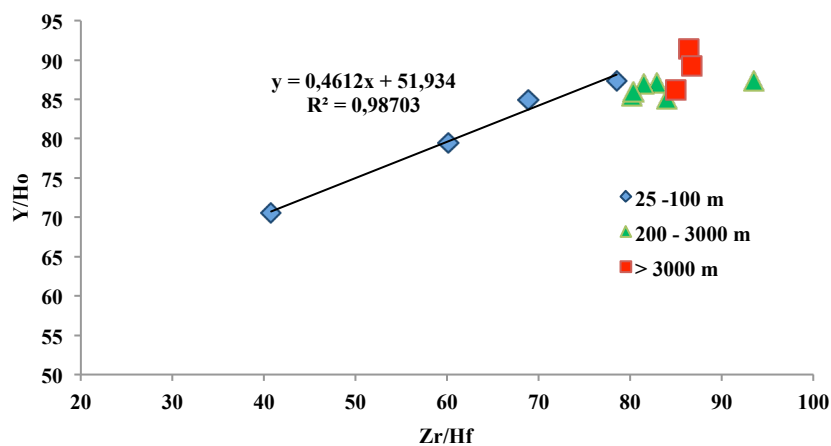
”chondritic“ line, similar to the shallowest samples collected by Godfrey et al. (1996) in their more coastal sampling site.

Fig. 3.8 Zr vs Hf relationship from ocean to continental context



Also Y/Ho ratio behaves similarly to Zr/Hf ratio as highlighted in Fig. 3.9. In this plot a correlation is found in the shallowest water layer (0-75 m). The statistical significance of this relationship progressively decreases with depth, thus suggesting that other processes (aside from the release of YREE from the lithogenic particulate matter) regulate the distribution of Y/Ho and Zr/Hf in the intermediate and deepest water layers. This hypothesis would explain why only intermediate and deepest waters from Mediterranean Sea fall in the ”seawater field“ depicted by Bau (1996) whereas shallowest samples are outside.

Fig. 3.9 Y/Ho vs Zr/Hf in Kryos water column



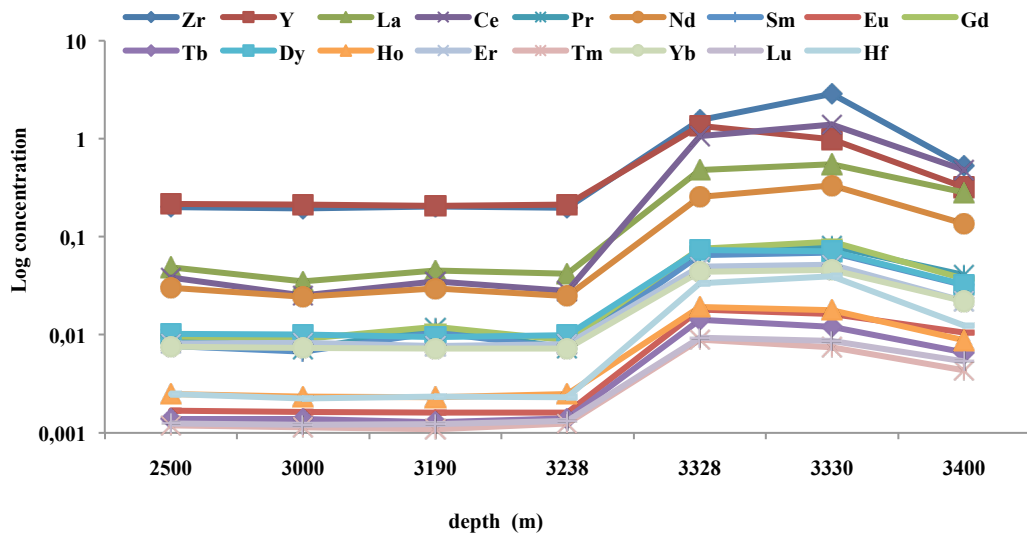
3.1.5.2. Deep hypersaline basin

YREE concentrations in deep-sea brines and at the oxic-anoxic interface are listed in Tab. 3.2. In Fig. 3.10 Zr, Hf and YREE distributions along the deepest water, the Tyro interface and brine are shown.

Tab. 3.2 YREE, Zr and Hf concentration (pmol/L) at the oxic-anoxic interface and inside the brine

depth (m)	Zr	Y	La	Ce	Pr	Nd	Sm	Eu	Gd	Tb	Dy	Ho	Er	Tm	Yb	Lu	Hf
Tyro Upper interface 3328 m	1557	1349	481	1065	70	255	64.7	18.0	75	14	73	19.3	50	8.9	44	9.3	34
Tyro Lower interface 3330	2874	992	550	1387	80	333	68.7	16.3	89	12	71	17.7	52	7.4	46	8.7	39
Tyro brine 3428	522	320	285	479	41	136	31.9	10.5	37	7	33	8.8	22	4.3	22	5.3	12.5
Thetis brine 3404	122	815	581	477	45	150	47.7	12.0	58	9	59	13.7	40	6.1	40	7.6	6.2
Medea brine 3034	954	609	396	566	54	176	53.1	13.5	60	10	45	12.5	35	8.4	42	11.2	10.5

Fig. 3.10 YREE concentration (pmol/L) at the oxic-anoxic interface and in deep sea brines

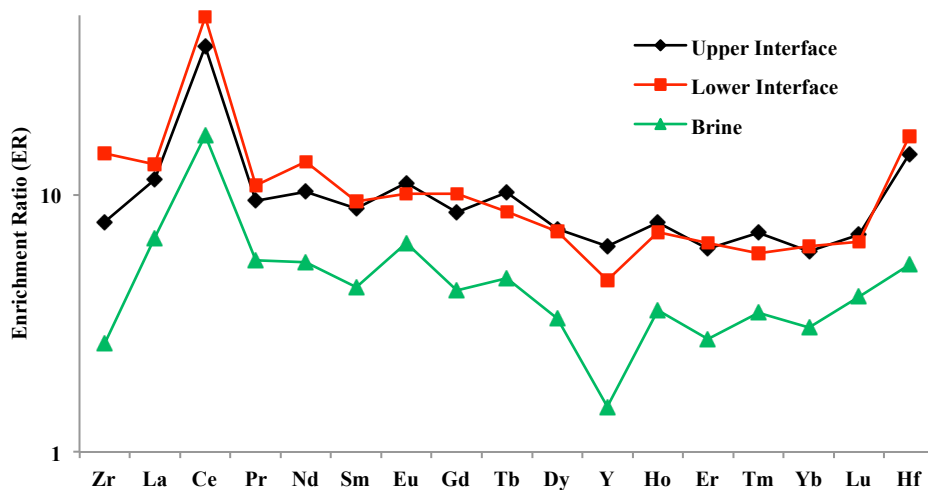


Above mentioned values are quite constant along the deepest water layer until the interface zone between oxic seawater and anoxic deep-sea brine. This interface was divided in upper (3328 m depth), and lower interface (3330 m depth), followed by the main brine body (3400 m depth).

All the above mentioned dissolved concentrations are characterised by strong increases that reach a maximum in the upper or lower interface and decrease downward in correspondence with the brine.

YREE, Zr, and Hf enrichment ratios (ER) of dissolved concentrations measured in the anoxic upper interface with respect to the oxic seawater (3238 m depth) range from 6 to 14 for all elements, with the largest value measured for Ce (38). This can be explained by reductive dissolution of CeO_2 to Ce^{+3} due to the decrease of redox potential from +199 mV to -288 mV (Fig. 3.11). Apart from Ce behaviour, a regular progressive decrease of ER values is observed with the increase in atomic number. Hf represents a further exception, its ER value being larger with respect to Lu one. Y shows an irregular behaviour too, its ER value being lower than that measured for both Dy and Ho, and also for Zr in the lower interface. A less regular ER sequence is observed in brines where Y and Zr behaviour is similar, whereas Hf behaves as a super heavy REE.

Fig. 3.11 YREE, Zr and Hf ERs in interface and anoxic hypersaline brine compared to overlying oxic seawater



As regards as YREE behaviour, our data closely agree with those reported by Bau et al. (1997) and by Schijfs et al. (1995). Values from Bannock basin are higher than Tyro basin

for La, Ce and Nd. Our values, otherwise, resemble closely those reported in Tyro basin by Bau et al. (1997).

Fig. 3.12a shows the YREE pattern normalised to PAAS for oxic seawater, interfaces and Tyro brine. The patterns are characterised by decrease of Y/Y^* values from seawater to lower interface, reaching negative value in brine. Negative seawater-like Ce anomaly values, become positive ($Ce/Ce^* = 1.5$) at the lower interface, then decreasing until $Ce/Ce^* = 1$ in brine. Compared to the oxic water column, both interfaces and brine show LREE enrichments and a flatter YREE normalised patterns. It is likely that local features influence YREE behaviour, given that little differences can be recognised in studied brines (Fig. 3.12b).

YREE normalised pattern shows higher LREE/HREE ratio compared to ambient seawater, suggesting a net effect of the competing process between surface and solution complexations.

Fig. 3.12a PAAS normalised YREE pattern in Tyro brine and seawater

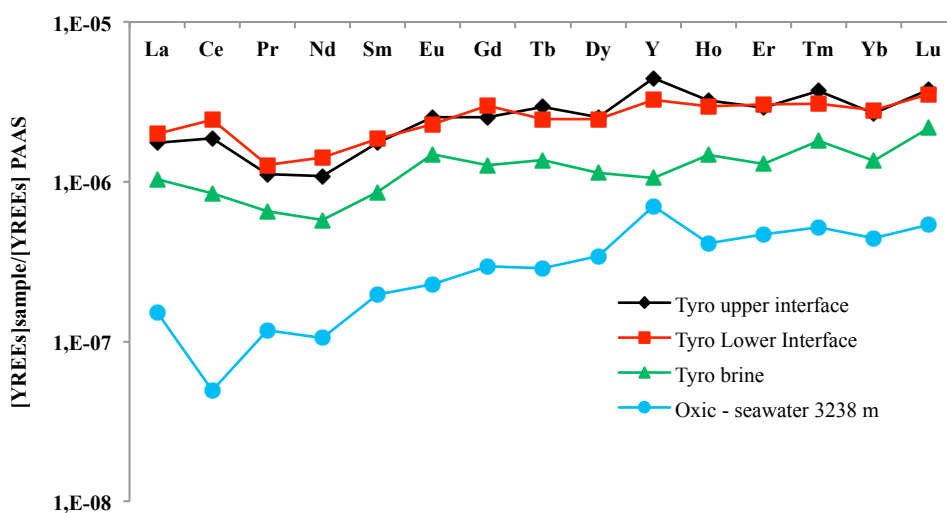
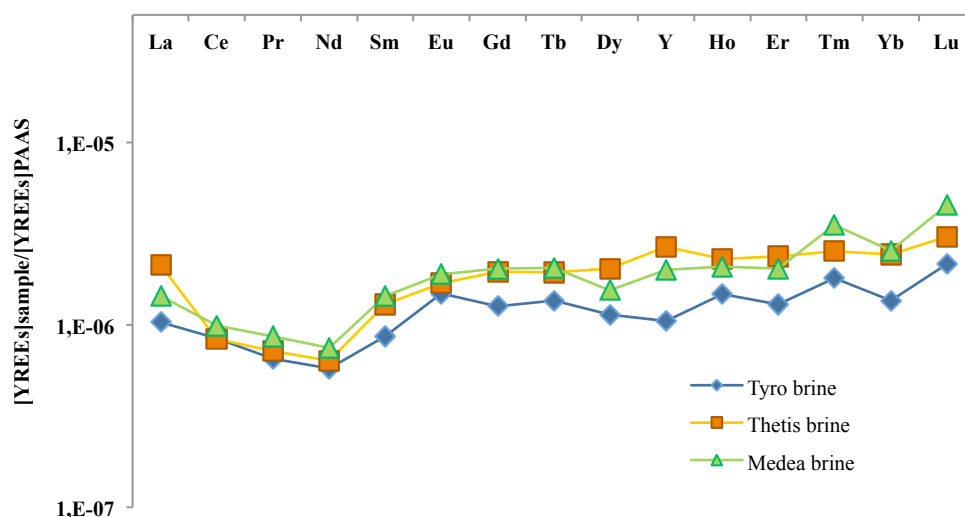


Fig. 3.12b PAAS normalised YREE pattern in Tyro, Thetis and Medea brine

There is no previous literature illustrating Y/Ho behaviour during the transition between oxic and anoxic environments taking in account the transitional environment offered by interface zone.

According to literature data, dissolved concentration of both Mn and Fe shows a sharp increase of four and two orders of magnitude, respectively (Bau et al., 1997), at the interface between oxic seawater and anoxic brine. This phenomenon is attributed to the reductive dissolution of Mn-Fe oxyhydroxides particle upon settling into the anoxic dense waters.

Upward diffusion of Mn^{2+} and Fe^{2+} across the interface may lead to the re-formation of fresh Fe- and Mn- oxyhydroxides. Trace metals may be involved in this redox-cycling to their scavenging by the Mn and/or Fe oxyhydroxides in oxic waters and their release upon dissolution of the carrier phases in sub or anoxic water below the redox-boundary.

Precisely in this environment, data collected on Y and Ho indicate that their behaviour is related to the same process as the reductive dissolution of Ho-enriched authigenic FeOOH particulate formed along the seawater column. This dissolution involves a general YREE increase in dissolved pool from seawater to interface. During this dissolution Y/Ho ratio sharply decreases from 90 in oxic medium to 35 in the deep brine.

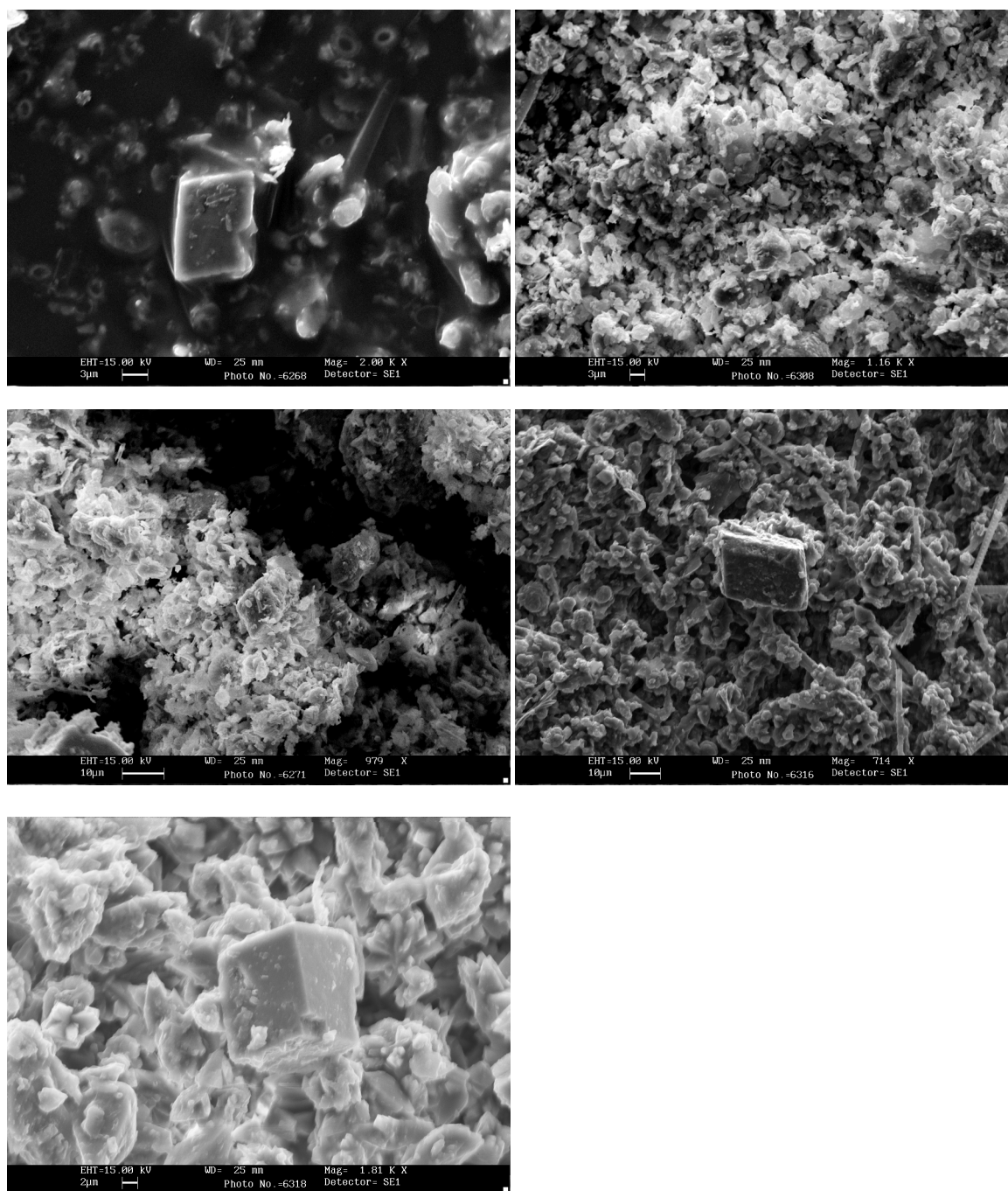
Also Zr vs Hf relationship abruptly changes at the interface between oxic seawater and brine. This is well evidenced by changes of Zr/Hf ratio that is clustered at about 86 in deepest seawater samples and decreases to reach the lowest recognised values close to 42 in deep brine. These data suggest that both Hf and Ho behave similarly at oxic-anoxic interface.

In deep sea brine, YREE dissolved contents decreases again, suggesting the occurrence of a new YREE scavenging episode onto newly-formed reduced phases. As it can be seen in Fig. 3.12, the interface-to-brine transition is highlighted by: changes in terms of LREE/HREE fractionation, Pr, Nd and Sm depletions, the growth of a slight positive Eu anomaly and a general decrease of dissolved YREE concentrations. The last evidence concurs to depict a scenario where the main process is the crystallization of authigenic phases, as demonstrated by the finding of authigenic dolomite rhombohedral in shallow layer of sediments in contact with brines (Fig. 3.13). Moreover, dolomite occurrence is consistent with observed YREE features in Fig. 3.12 because authigenic carbonates are usually enriched in LREE with respect to coexisting solution (Zhong and Mucci, 1995) and with observed LREE enrichment, Eu depletion and progressive decreasing of REE contents with increasing atomic number in dolomite crystals in sediments (Banner et al., 1989). These above mentioned evidence suggests that the authigenic dolomite crystallization can indeed influence the YREE distribution in coexisting brines with examined sediments.

Inside the brine, both Y/Ho and Zr/Hf ratios decrease due to lower removal rate of Ho and Hf than Y and Zr; this evidence suggests that the removal process inside the brine is different from the removal process along the water column. It is likely that, during dissolution and/or crystallization of FeOOH, Y/Ho and Zr/Hf change in similar way, whereas this phenomenon doesn't occur for the crystallization of authigenic dolomite. This process affects differently the two geochemical twins, probably for dissolved complexation reasons that

influence the Zr-Hf and Y-Ho behaviour, with Zr-Hf being driven by hydroxo-complexes and Y-Ho being driven by carbonate complexes.

Fig. 3.13 SEM analysis of deep hypersaline sediments

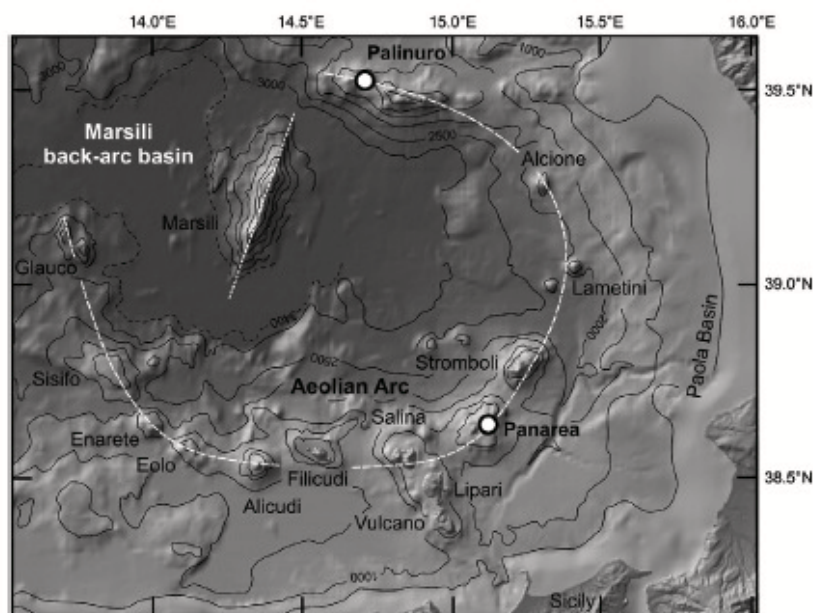


3.2. Hydrothermal submarine vents

3.2.1. Fumarolic vents in Panarea Island

Panarea is the smallest (3.3 Km²) of the Aeolian Islands (southern Tyrrhenian Sea), although it homes the emerging part of a wide stratovolcano which is more than 2000 m high and 20 Km long. (Gabbianelli et al., 1993). The Aeolian archipelago is a ring-shaped volcanic arc that lies north of Sicily and borders the SE portion of the Tyrrhenian Sea. The archipelago is formed by seven islands and ten seamounts, associated with the Peloritanean-Calabrian orogenic belt, including the present active volcano of Stromboli. The sea among Vulcano and Panarea islands shows fumarolic activity and gas vents (Fig. 3.14).

Fig. 3.14 Aeolian Archipelago
(from Peters et al., 2011)



Panarea volcanic complex consists of at least three separated portions: 1) the main Panarea island, showing a complex morphology resulting from the subaerial emplacement of several dacitic domes between 150 and 100 ka; 2) the endogenous dome of Basiluzzo (3 Km NE of Panarea island); and 3) the submarine fumarolic field, located about 2.5 Km E of

Panarea island surrounded by five emerging reefs (Dattilo, Bottaro, Lisca Bianca, Panarelli, Lisca Nera). The emerging reefs are arranged along a circular rim of about 1 Km in diameter and are characterised by a maximum sea depth of 30 m. According to Calanchi et al., (1999), the reefs are made of high K-calc-alkaline dacite and porphyritic basaltic-andesite lavas.

The spatial distribution of fumarolic vents appears to be controlled by NNE and NW oriented fault system aligned with the dominant regional tectonic lineaments of the Aeolian Island. The discharging fluids are the superficial expression of a marine shallow-water hydrothermal system, whose composition was modified during the 2002 gas blast by inputs of magmatic-related fluids. The emission were found to be an aerosol of CO₂-dominated gas with suspended sediments, colloidal sulphur and water microdroplets acidified by dissolution of compounds such as SO₂, HCl and HF (Capaccioni et al., 2006).

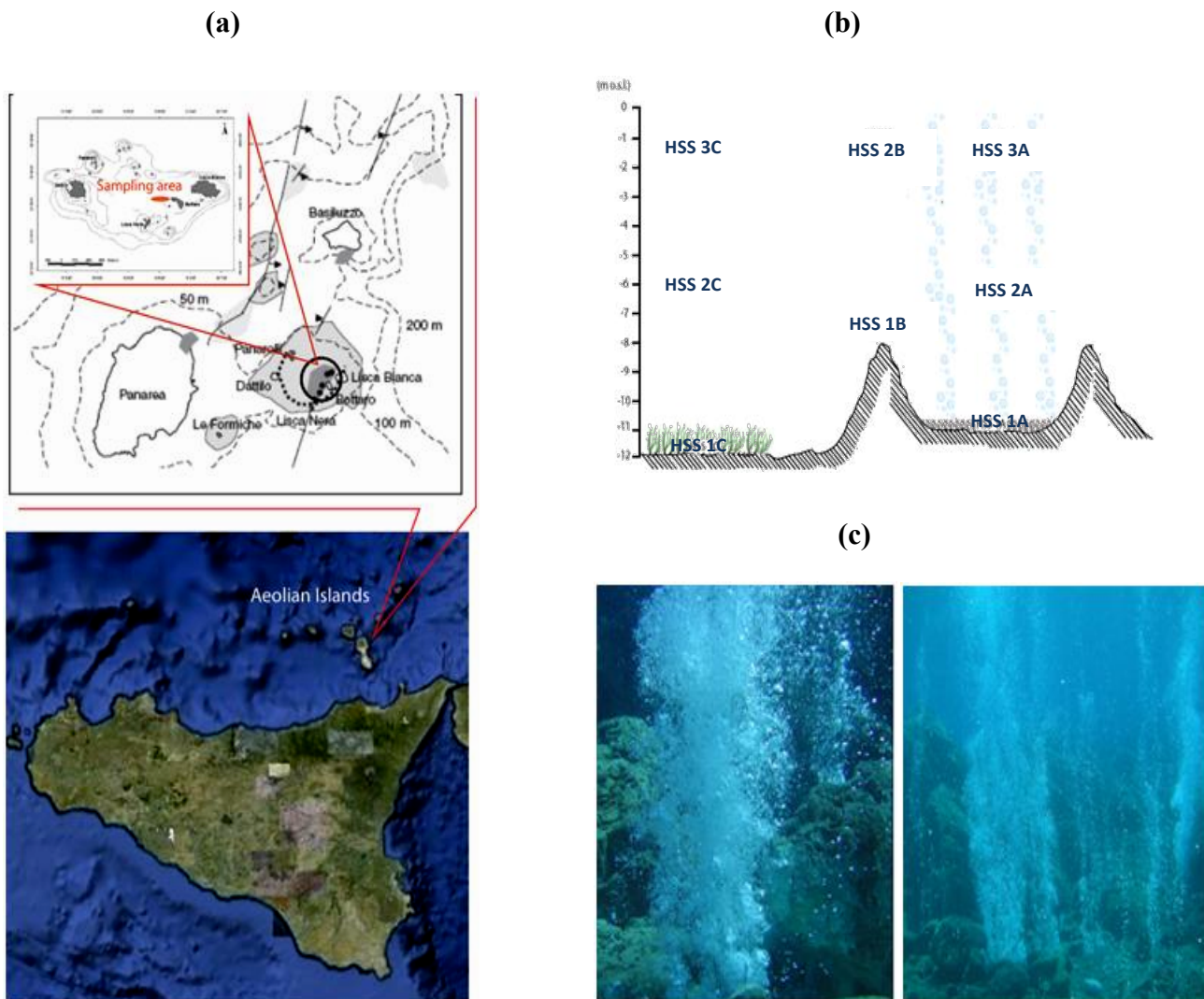
For this study seawater samples were collected in front of Bottaro (38°38'20"N 15°06'37"E) by diving, starting from the emission point HSS1A, formed during the volcanic events of 2002 (Fig. 3.15 a,c), and moving towards the shallow water layer represented by point HSS3A. Furthermore, starting again from the emission point HSS1A, samples were collected radially along the E-W transect, from the sites named HSS1B÷HSS3C, (Fig. 3.15 b).

3.2.2. Collection and storage

Seawater samples were collected in a 1 L bottle and prepared for the analyses. For trace metal analysis samples were filtered and acidified while, for anion determinations, samples were only filtered.

Physical-chemical parameters (pH, temperature and conductivity) were determined *in situ*. Chemical analysis on major anions were carried out by ion-chromatography. The HCO₃⁻ content was determined in the laboratory by volumetric titration with HCl. YREE, Zr and Hf content was carried out by co-precipitation on Fe(OH)₃.

**Fig. 3.15 (a) Sampling point (modified from Sieland, 2009), (b) Sampling plan,
(c) Main gas exhalation on Bottaro sampling point in November 2002
(from WISTAU 2007 + 2008)**



3.2.3. Results

YREE, Zr and Hf concentrations in hydrothermal submarine springs (HSS) from Aeolian Islands are reported in Tab. 3.3. At this depth, only limited changes could be observed for most elements, probably due to the shallow water where these springs occur.

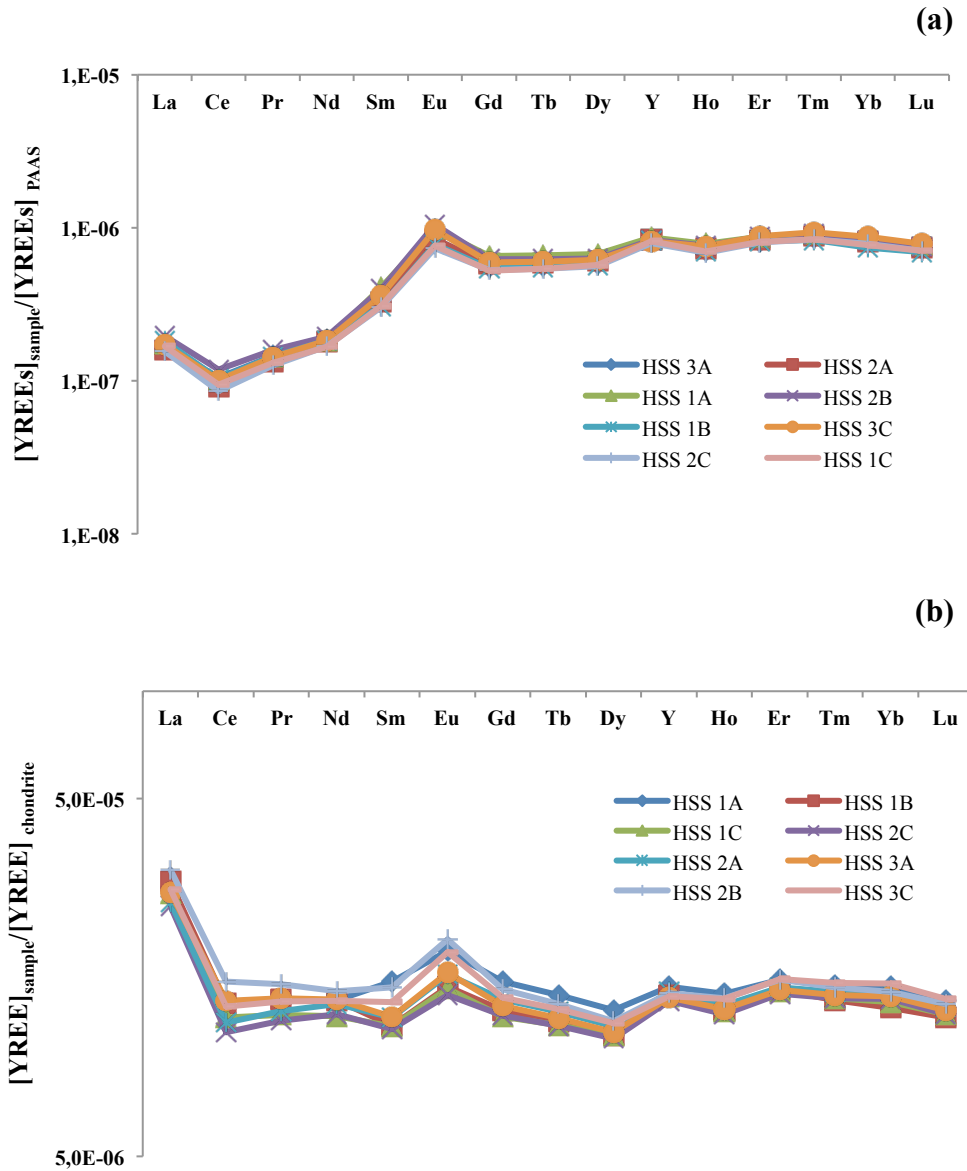
As a consequence of quick dilution in the seawater body and the distance from the emission point, all the shallowest waters and the whole seawater column in C point showed the same Zr, Hf and YREE contents. On the contrary, samples collected near to the hydrothermal source were characterised by different Zr, Hf and YREE concentrations. In particular, vertical distributions of investigated elements decreased from bottom to surface waters. La, Ce, Pr and Nd deviated from this trend, and reached a minimum value at 6 m below the sea level. The distribution of Zr mainly changed along the A seawater column that is the most sensitive to the increasing distance from the hydrothermal source, thus implying that the lowest Zr concentration was recorded at the bottom of the A water column (sample 1A).

Tab. 3.3 YREE, Zr and Hf contents (pmol/L) in hydrothermal submarine springs

Sampling point	Zr	Y	La	Ce	Pr	Nd	Sm	Eu	Gd	Tb	Dy	Ho	Er	Tm	Yb	Lu	Hf
HSS 1 A -11 m	117	263	48	58	9.0	43	15.1	6.9	19.5	3.2	19.4	4.7	14.9	2.2	14.0	1.9	3.5
HSS 2 A -6 m	150	255	44	52	8.4	42	12.0	6.0	17.4	2.9	17.5	4.4	14.2	2.1	13.3	1.8	2.6
HSS 3 A -1 m	123	246	47	60	9.1	43	12.1	6.0	16.7	2.8	16.8	4.2	14.0	2.1	13.1	1.8	2.2
HSS 1 B -1 m	125	253	54	67	10.0	46	14.6	7.5	18.5	3.0	18.1	4.5	14.9	2.2	13.4	1.9	2.7
HSS 2 B -8 m	124	250	50	59	9.0	43	11.4	5.5	16.2	2.7	16.5	4.2	14.0	2.0	12.1	1.7	3.1
HSS 1 C -12 m	121	247	46	54	8.2	39	11.4	5.5	15.6	2.6	16.5	4.2	13.8	2.0	12.6	1.8	2.6
HSS 2 C -6.2 m	100	240	43	49	7.9	40	11.2	5.2	15.7	2.6	16.1	4.1	13.6	2.0	12.8	1.8	2.3
HSS 3 C -1 m	126	248	48	57	8.9	43	13.3	6.9	17.6	2.9	17.9	4.5	15.0	2.2	14.2	1.9	2.3

The occurrence of the hydrothermal source can be recognised by features of normalised YREE concentrations (Fig. 3.16 a). Only at first glance, such features look very similar among all the examined HSS samples.

**Fig. 3.16 (a) PAAS normalised YREE pattern in Hydrothermal submarine springs,
(b) Chondrite normalised YREE pattern in Hydrothermal submarine springs**

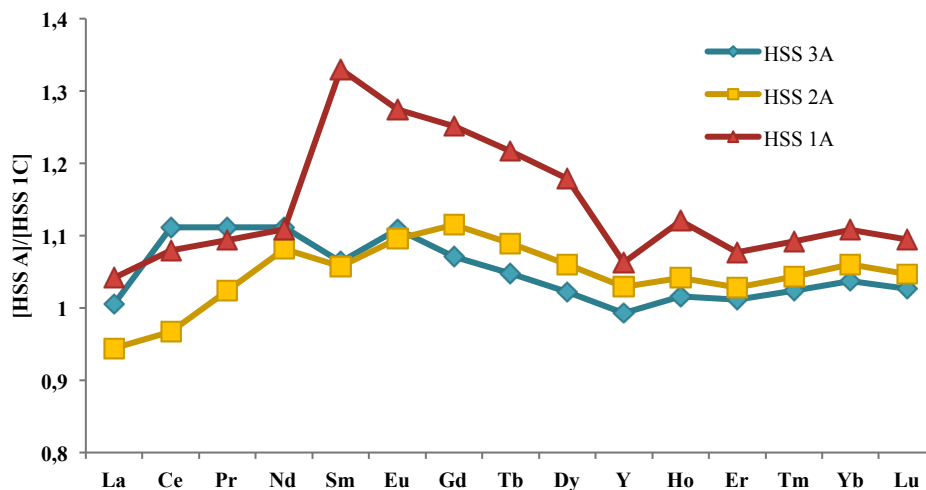


This evidence is mainly justified by our collection of waters that represent a mix between hydrothermal fluids and shallow seawater. This condition was confirmed by: i) clearly negative Ce anomaly values that are typical for seawater rather than for hydrothermal sources (Bau et al., 1997; Alibo and Nozaki, 1999), ii) significant but not hugely positive Eu anomalies that can be explained only if strongly Eu-enriched hydrothermal fluids are diluted into a larger seawater mass that usually doesn't show Eu positive anomalies (German et al.,

1990; Douville et al., 1999). However, it was reassuring that also YREE fractionations of both shale normalised concentrations or of chondrite-normalised concentrations were characterised by general seawater-like features. Only La was slightly enriched with respect to other LREE, as shown in chondrite-normalised patterns (Fig. 3.16 b). The same feature can be recognised in Y/Y^* value that was less positive in HSS ($Y/Y^* = 1.2$) than in seawater ($Y/Y^* = 1.8$).

Although YREE pattern normalised to PAAS showed characteristic seawater features and are very similar all together, impressive differences among the studied HSS samples can be highlighted by normalising their YREE contents to YREE compositions of sample HSS1C, collected far from hydrothermal source in an area free from contaminations from hydrothermal fluids (as evidenced by occurrence of a large *Posidonia* colony on seafloor). HSS1C normalised patterns of samples collected closer to hydrothermal source are reported in Fig. 3.17.

Fig. 3.17 HSS1C normalised YREE pattern

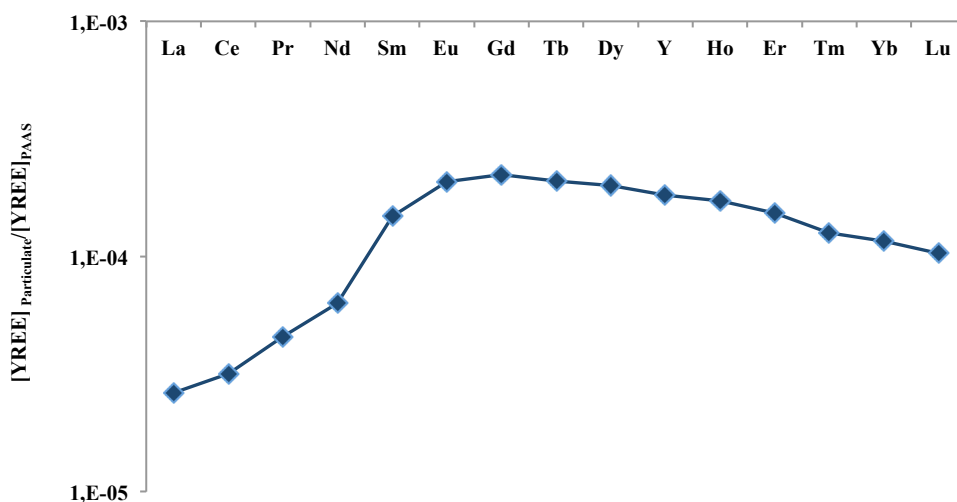


Positive Sm anomaly recorded near the emission point is related to the large Sm affinity for Fe-bearing solids stable under hydrothermal conditions, which dissolve in contact with seawater. In farther places, crystallization of authigenic Fe-oxyhydroxides preferentially removes Sm from dissolved pool allowing the observed Sm negative anomaly values reported in Fig. 3.17. These features indicate that YREE fractionations are induced by mixing between

seawater and hydrothermal fluids. Their significance can be fully explained by comparing them with YREE distribution in the particulate matter sinking around the hydrothermal source, close to HSS1A sample (Fig. 3.18).

Dissolved HSS1A composition, normalised as mentioned above, mirrors the YREE distribution in particulate matter normalised to PAAS. Differences are limited to Y fractionation with respect to Ho, and to the concentration of Sm. Furthermore, the concentration of Sm is higher compared to its neighbours. These differences only occur in dissolved phase normalised to "unaffected" seawater composition (identified by sample HSS1C)

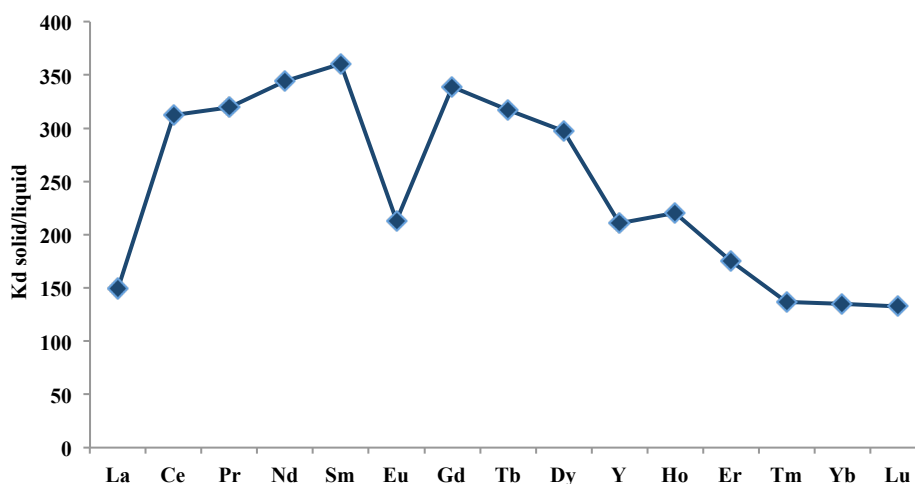
Fig. 3.18 PAAS normalised YREE pattern of particulate matter of HSS1A



The discussed similarities between YREE contents in particulate matter and HSS1A samples suggest that the materials can represent the authigenic fraction precipitated by dissolved mix between hydrothermal fluids and seawater and the parent dissolved fraction, respectively. If this hypothesis is true, their concentration ratios would represent YREE distribution coefficients calculated during solid-liquid process between the dissolved phase (representative of hydrothermal fluid-seawater mix) and authigenic crystallizing solid.

Effectively calculated YREE K_d values for above mentioned samples (Fig. 3.19) are very similar to values of distribution coefficients measured by Bau (1999) for YREE scavenging onto FeOOH. In particular, our values behave similarly to K_d values calculated by Bau (1999) at pH=6.21. However our values indicate that Y is less fractionated with respect to Ho, and the K_d value for Eu is lower than the value expected from the K_d sequence reported by Bau (1999).

Fig. 3.19 Distribution coefficients (K_d)

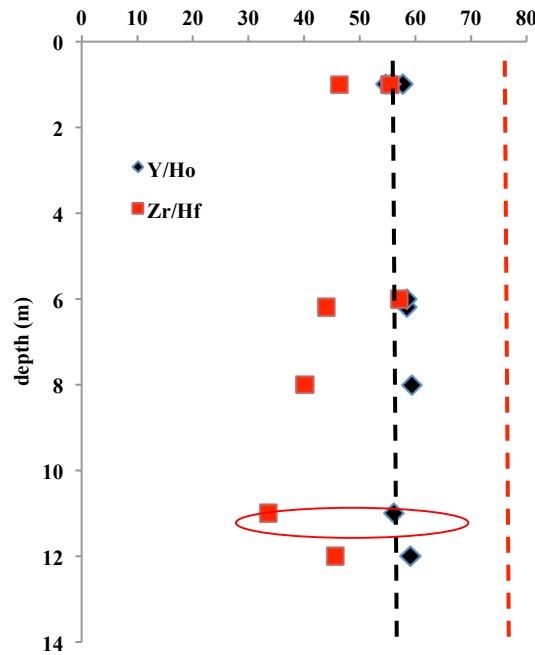


Y/Ho ratio in the studied area has slightly superchondritic values, with tendency to show lower values close to the emission vent. This evidence agrees with larger Ho particle reactivity with respect to Y, that produces a preferential Ho scavenging onto particulate surfaces, similarly to phenomena recognised in several submarine hydrothermal systems around the world (Klinkhammer et al., 1994; Douville, et al., 1999)

Zr/Hf ratio behaviour during hydrothermal submarine emissions in the studied area is similar to the above reported Y/Ho ratio (Fig. 3.20).

Fig. 3.20 Y/Ho and Zr/Hf values in hydrothermal submarine springs

Dot lines are chondritic values. Red circle highlights Y/Ho and Zr/Hf values in HSS1 sample



Zr/Hf values are always subchondritic close to the hydrothermal vents ($\text{Zr/Hf} \approx 32$ molar ratio) and mildly increase from deep to shallow waters ($\text{Zr/Hf} \approx 55$ molar ratio). Similarly to Y/Ho behaviour, the evolution of Zr/Hf ratio could be induced by larger Hf affinity for particles with respect to Zr. This Hf affinity is confirmed by the calculated $K_d^{(\text{Hf})}$ value (2104.7) which is larger than $K_d^{(\text{Zr})}$ value (293.3), confirming that dissolved Zr and Hf behaviour in seawater is coherent with Fe equilibria between dissolved and suspended phases.

No references are present about Zr/Hf ratio values analysed in submarine hydrothermal vents, and only scarce information can be found about the range of Zr/Hf values in other thermal waters. Therefore is very difficult to compare observed data in the studied area with previous measurements. Only a few data of Hf concentrations in Mn-Fe nodules are reported by Godfrey et al. (1997) and they suggest that hydrothermal vents in deep seawater can represent a Hf source for seawater coming from altered oceanic crust Hf leaching in hydrothermal systems where high Mn/Fe ratios occur. This is consistent with the strong

affinity occurring between Zr and Hf behaviour in seawater and iron confirmed by our measurements of Zr and Hf K_d values that agree with evidences of strong Hf affinity for FeOOH reported by Koschinsky and Hein (2003).

3.3. Thermal springs

3.3.1. Thermal spring along Belice Fault (Western Sicily)

Sicily represents the southernmost part of the Alpine orogenesis in the Mediterranean. It comprises the Iblean Plateau (foreland) and the Appennine-Maghrebien Chain located in the northern part, mostly made of carbonate rocks and characterized by southward vergence.

The structural geology of western Sicily is characterised by the overlap of south-trending stratigraphic-structural units (Catalano et al., 1983) placed between the lower Miocene and the middle-upper Pliocene. Their lithological features identify various hydrological system (Fancelli et al., 1991):

- 1) Carbonate complex, with high permeability due to fissuring and karsification.
- 2) Clay and Clayey-sand complex, impermeable in the clay levels and locally permeable in the conglomerate layers.
- 3) Evaporite and limestone-marly complex, permeable for fissuring and karsification.
- 4) Marly sandstone, calcarenite and alluvial complex, with permeability ranging from high in alluvial rocks to very low in clayey ones.

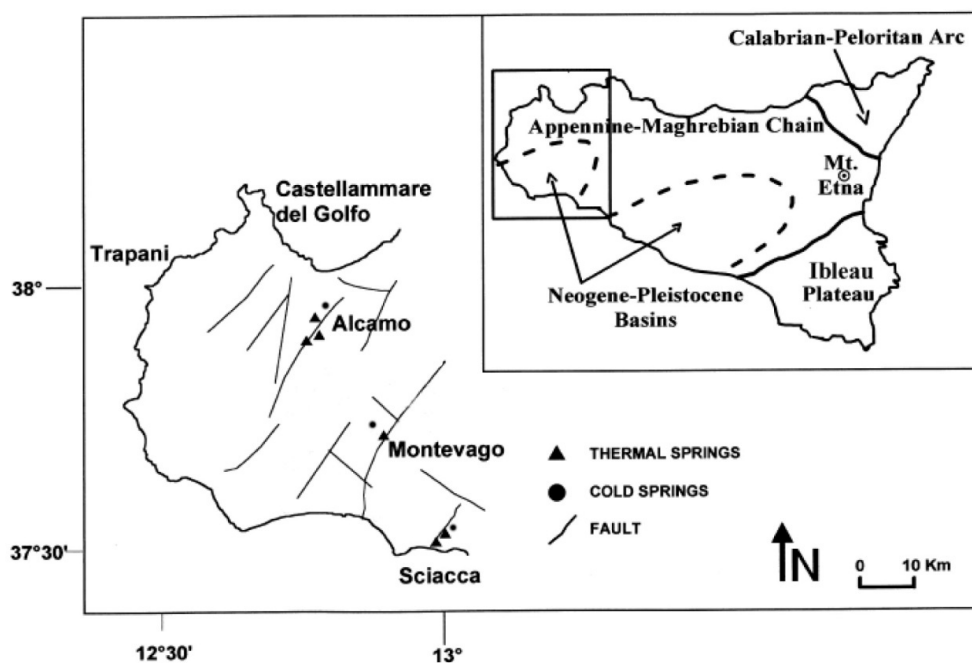
In this area, the stratigraphic-structural units belonging to the Trapanese domain are tectonically overthrust on the Saccense ones (Catalano and D'Argenio, 1982). Moreover, there are outcrops of evaporitic deposits made up of limestone, gypsum and highly soluble salts, such as halite, kainite and sylvite, etc. From a hydrogeological point of view, the carbonate units belonging to the Trapanese and Saccense domains are the most important, because of their capability to form reservoirs. The carbonate complex contains circuits giving rise to both

cold and thermal springs. In terms of structures and tectonics, these units are characterized by fault systems mainly directed W-E and NW-SE. A succession of tectonic events over time has formed a horst and graben structure on the stratigraphic-structural carbonate units. In this context, faults play an extremely important role because, on the one hand, they form the vertical hydraulic continuity within the carbonate reservoirs and, on the other hand, they allow the waters to rise and thus form the main thermal springs in the area.

3.3.2. Sampling and storage

The thermal spring sampled are located in the northern part of the study area (Alcamo-Segesta), central southern part (Montevago) and further south, on the Mediterranean coast near Sciacca (Fig. 3.21). Water temperature, pH and conductivity were measured directly in situ. HCO_3^- content was measured by titration with HCl. Water samples were filtered through 0.45 μm filter and the major constituent determined by ion-chromatography and AA spectrometer. YREE, Zr and Hf content were determined by co-precipitation on $\text{Fe}(\text{OH})_3$.

Fig. 3.21 Location of sampling sites and the main fault systems of Western Sicily (modified from Favara et al., 2001)



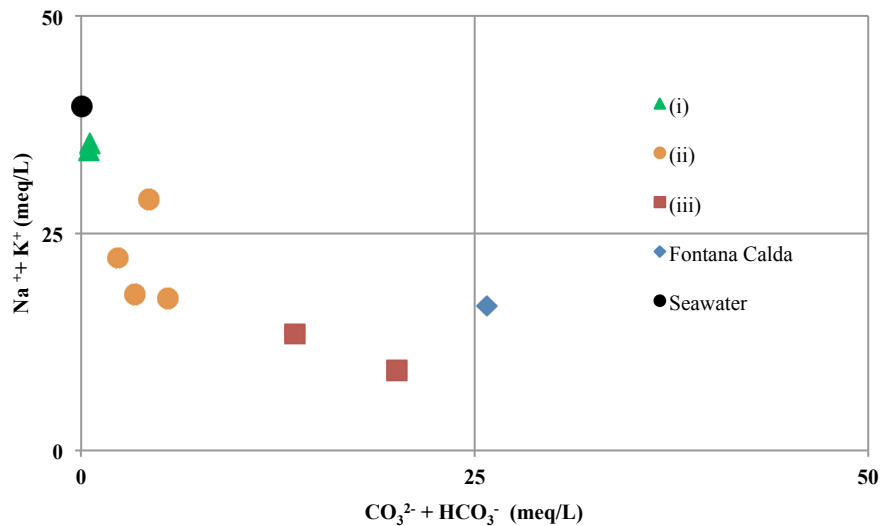
3.3.3. Results

Water samples were classified according to measured temperatures and their main chemical constituent (Tab. 3.4).

Tab. 3.4 Physical-chemical parameters of water samples of western Sicily

sample	date 2011	coordinate	T °C	pH	cond mS/cm	Na ⁺ meq/L	K ⁺ meq/L	Ca ²⁺ meq/L	Mg ²⁺ meq/L
Sciacca Hotel	May	37°30'22"N 13°05'17"E	52.00	5.80	14.00	256.30	9.69	79.48	31.19
Terme Selinuntine	May	37°30'28"N 13°05'34"E	53.00	5.96	14.00	243.71	9.40	77.37	36.53
Gorga Botola	June	37°58'14"N 12°54'29"E	48.00	6.51	2.89	14.28	0.66	11.56	7.30
Gorga Canne	June	37°58'35"N 12°54'21"E	46.10	6.64	2.09	7.34	0.41	8.67	5.24
Montevago	May	37°42'22"N 12°58'45"E	37.70	6.68	2.01	7.50	0.38	8.79	5.83
Terme Segestane	June	37°58'21"N 12°53'37"E	44.00	6.79	2.35	11.52	0.48	3.42	5.40
Fontana Calda	May	37°31'07"N 13°08'01"E	29.80	7.20	1.18	3.75	0.36	5.42	2.85
Partanna	May	37°42'35"N 12°55'20"E	18.00	7.20	1.36	3.87	0.04	8.26	2.45
Bevaio Pioppo	June	37°59'19"N 12°54'18"E	23.00	6.97	0.82	1.90	0.06	5.70	3.04
sample	date 2011	CO ₃ ²⁻ meq/L	HCO ₃ ⁻ meq/L	Cl ⁻ meq/L	SO ₄ ²⁻ meq/L	F ⁻ meq/L	Br ⁻ meq/L	NO ₃ ⁻ meq/L	S ²⁻ meq/L
Sciacca Hotel	May	0.00	4.72	415.13	15.37	0.63	1.90	0.00	2.64
Terme Selinuntine	May	0.00	4.69	465.44	16.82	0.82	1.85	0.00	2.14
Gorga Botola	June	0.00	1.55	19.65	11.82	0.21	0.03	0.00	0.15
Gorga Canne	June	0.00	1.47	9.93	10.39	0.21	0.02	0.00	0.17
Montevago	May	0.00	2.38	8.45	10.70	0.12	0.02	0.01	0.00
Terme Segestane	June	0.00	2.36	12.92	12.28	0.22	0.02	0.02	0.11
Fontana Calda	May	0.00	3.23	1.72	1.32	0.01	0.00	0.24	0.00
Partanna	May	0.00	3.59	4.22	5.42	0.03	0.01	0.21	0.00
Bevaio Pioppo	June	0.00	2.18	2.11	1.15	0.01	0.00	0.53	0.00

For a preliminary classification of the waters, concentration of the major component are plotted on the Langelier-Ludwig diagram of Fig. 3.22.

Fig. 3.22 Langelier-Ludwig diagram

According to previous studies (Favara et al., 2001 and reference) three main groups can be identified:

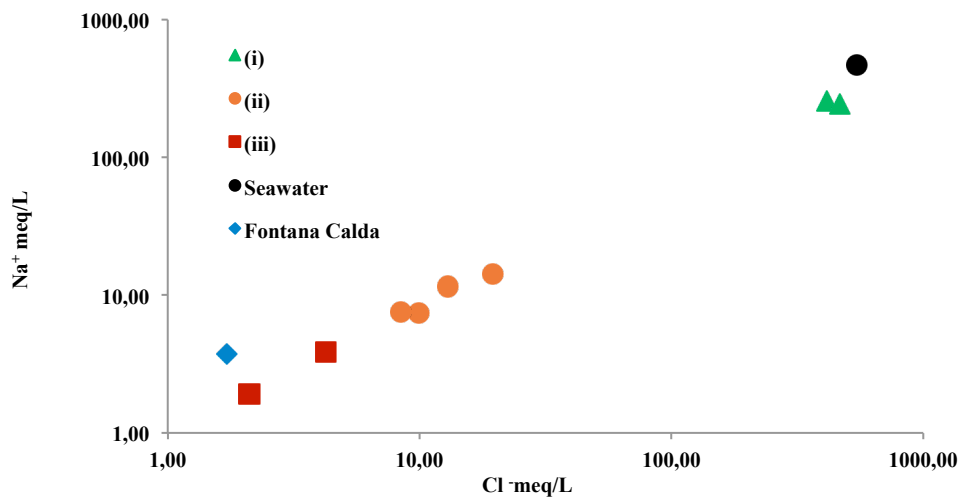
- (i) Thermal springs (Sciacca) collected near Sciacca are chloride-sulphate alkaline waters with composition very close to seawater.
- (ii) Thermal springs (Seg-Alc) sampled in a region between Segesta and Alcamo, parallel to a major tectonic structure of western Sicily are chloride sulphate earth –alkaline waters.
- (iii) Cold springs located along the same valley of the River Belice, but lacking the typical characteristics of the hydrothermal sources although classified as chloride-sulphate alkaline – earth waters, show a higher content of carbonates and bicarbonates in relation to (ii).

The water sample of "Fontana Calda", although formally belonging to group (i), shows different chemical composition falling along the border between chloride-sulphate waters and the bicarbonate earth-alkaline waters.

The Na-Cl graph (Fig. 3.23) shows that all sampled waters have Na/Cl ratio close to that of seawater. This evidence suggest that NaCl contribution could be linked to a distinct

process. On the basis of Na^+ and Cl^- contribution it is possible to divide all sampled waters in the same groups as Fig. 3.22; in particular springs (i) show the highest Na^+ and Cl^- contents very close to seawater, springs (ii) show concentration of Na^+ and Cl^- between 7 and 14 meq/L and between 8 and 20 meq/L respectively. Cold springs (iii) are the least affected by marine contribution in the reservoir showing Na^+ and Cl^- content lower than 4 and 5 meq/L, respectively. The thermal springs “Fontana Calda” is the only one to stand aside from the general trend showing a Na/Cl ratio of 2.19.

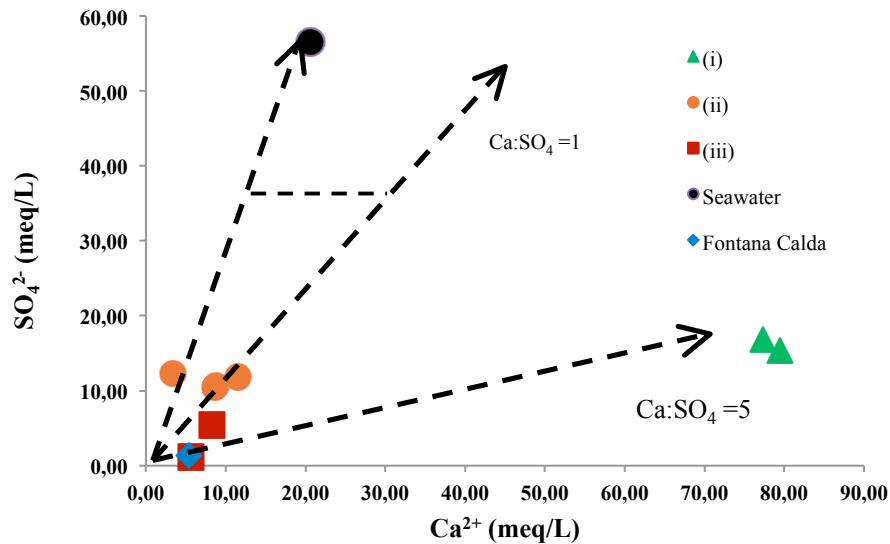
Fig. 3.23 Na^+ vs Cl^- relationship in water samples of western Sicily



The high content of Cl^- and Na^+ in the samples (i) implicate a direct contribution of seawater and/or interaction of groundwater with highly soluble evaporitic deposits. The latter hypothesis could be supported by the measured concentrations of Br (150 mg/L) and K (370 mg/L) in these waters, that are higher than those of sea water. The evidence of Fig. 3.24 support the hypothesis that the higher water content in group (ii) and (iii) may also be affected by interaction with sulphate evaporite sediments outcropping extensively along the tectonic structure of the Belice Valley. The water collected at “Terme Segestane” falls along the Ca/SO_4 line typical of seawater. The composition of waters (i) suggest an interaction with the

most evolved salts deposits of Messinian period. The Ca^{2+} enrichment with respect to SO_4^{2-} implies that an additional interaction with carbonate rocks cannot be excluded.

Fig. 3.24 Ca^{2+} vs SO_4^{2-} relationship in water samples of western Sicily



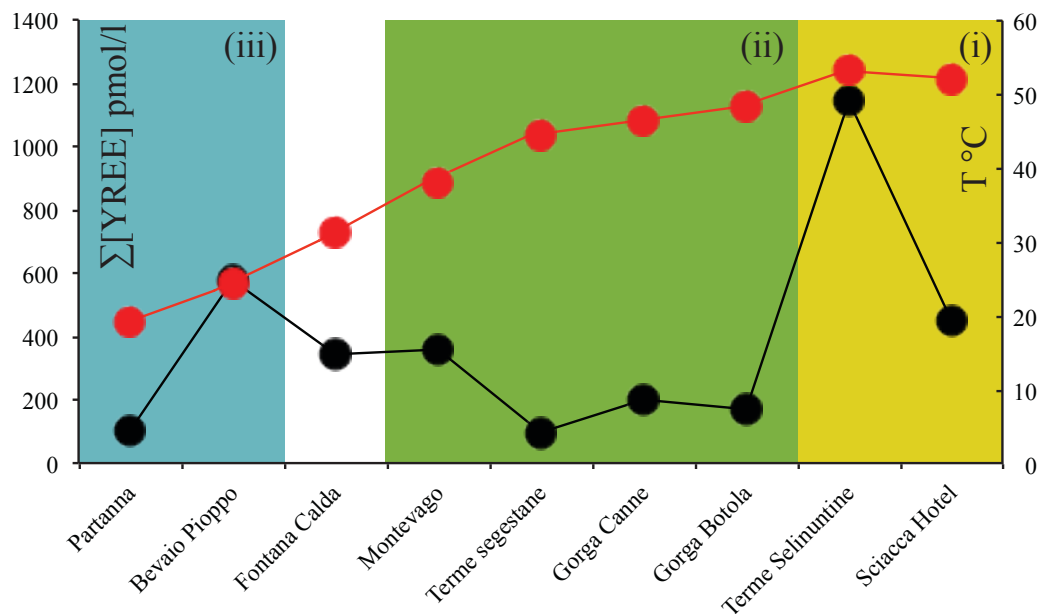
Trace element concentrations of water samples are listed in Tab. 3.5. Sample waters of springs (i) show the highest YREE, Zr and Hf contents, on the contrary the water collected at “Terme Segestane” show the lowest ones. Sample water (iii), both belonging to cold spring group show a different trace elements distribution.

Tab. 3.5 YREE, Zr and Hf concentration in western Sicily springs (pmol/L)

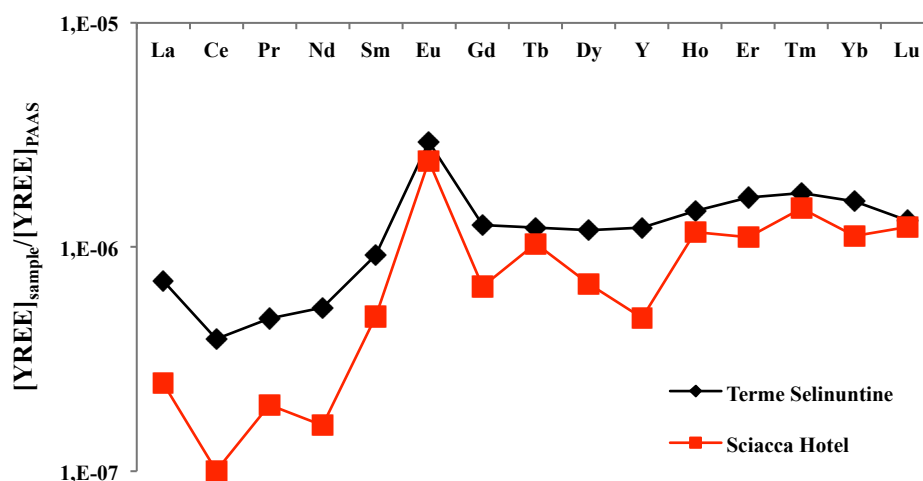
	Zr	Y	La	Ce	Pr	Nd	Sm	Eu	Gd	Tb	Dy	Ho	Er	Tm	Yb	Lu	Hf
Partanna	48	31	14	17	2.3	9.4	4.6	4.5	4.8	0.77	4.5	1.22	4.2	0.64	4.1	0.78	5.8
Bevaio Pioppo	14.7	339	49	14	7.8	64	16.0	8.6	21	3.4	19.6	4.6	14.1	2.07	13.0	1.90	3.0
Fontana Calda	11.0	101	38	59	10.4	57	14.2	7.8	15.8	2.4	12.6	2.9	8.6	1.31	8.5	0.93	2.4
Montevago	33	95	49	91	11.6	44	12.3	6.9	14.5	2.21	12.0	2.6	7.4	1.11	7.1	0.84	1.45
Terme Segestane	16.2	28	13	22	2.7	9.8	4.0	3.2	3.9	0.59	3.2	0.85	2.9	0.42	2.6	0.42	2.2
Gorga Canne	29	55	33	40	5.4	21.6	7.4	4.8	7.6	1.22	7.2	1.75	5.6	0.90	6.1	0.90	1.75
Gorga Botola	31	41	28	38	4.8	18	7.3	5.9	7.5	1.19	6.9	1.64	5.1	0.81	5.4	0.85	1.97
Terme Selinuntine	344	370	195	220	30.2	126.6	33.9	20.9	37	5.9	34	8.6	28	4.2	26	3.3	12.5
Sciacca Hotel	218	147	68	57	12.4	38	18.0	17.2	20	5.0	19.7	7.0	18.9	3.6	18.3	3.1	12.8

Fig. 3.25 suggests that the trace elements content must be considered in conjunction with the temperature of the fluid. This effect, linked to the lithology and composition of their host rock aquifers, is evident among the different groups of sources as highlighted by the highest concentration and the high temperature of (i) samples. Furthermore the highest concentrations of the elements under investigation recorded in the Sciacca area are a clear effect of temperature.

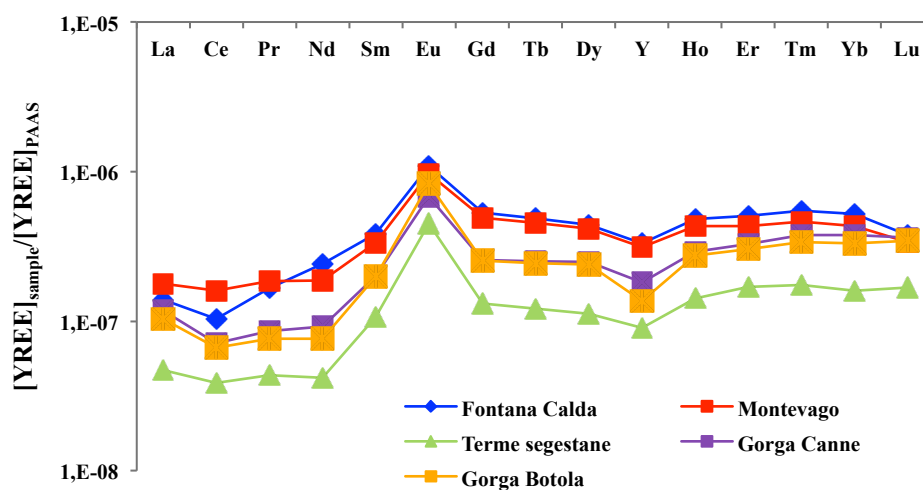
Fig. 3.25 Σ YREE (pmol/L) in water samples of western Sicily



The analysis of the YREE patterns normalized to PAAS for (i) group (Fig. 3.26) shows a clear positive Eu anomaly characteristic of hydrothermal fluids and a significant negative Ce anomaly, which presupposes the existence of oxic conditions. Moreover, the YREE pattern shows the seawater characteristic enrichment of LREE. Despite these common features, the two water samples show some differences in LREE contents, Y/Ho and Zr/Hf ratios; this evidence suggest the existence of different processes occurring during their interaction with solids in aquifers.

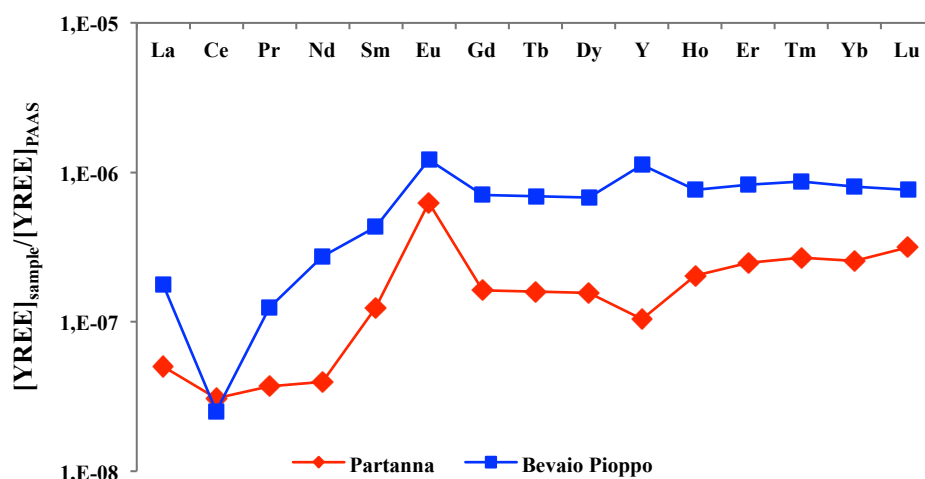
Fig. 3.26 PAAS normalised YREE pattern of thermal springs (i)

The dissolved YREE average amount of springs (ii) is sufficiently constant despite the temperature of the waters varying between 40 and 50°C (Fig. 3.27). The normalised patterns are similar, characterised by positive Eu anomaly and low negative Ce anomaly. Y/Ho ratio show subchondritic value that range between 25.2 and 36.7; also for these samples, this evidence suggests the occurrence of a process of preferential removal of Y onto the surfaces of phyllosilicates .

Fig. 3.27 PAAS normalised YREE pattern of thermal springs (ii)

The trace metal analysis of the two cold springs (iii) reveals a different total content of YREE. PAAs normalized pattern shown in Fig 3.28 highlights a elementary fractionation along the series suggesting that, although the two springs are classified in the same way according to temperature, the aquifers are fed differently.

Fig. 3.28 PAAS normalised YREE pattern of cold springs (iii)

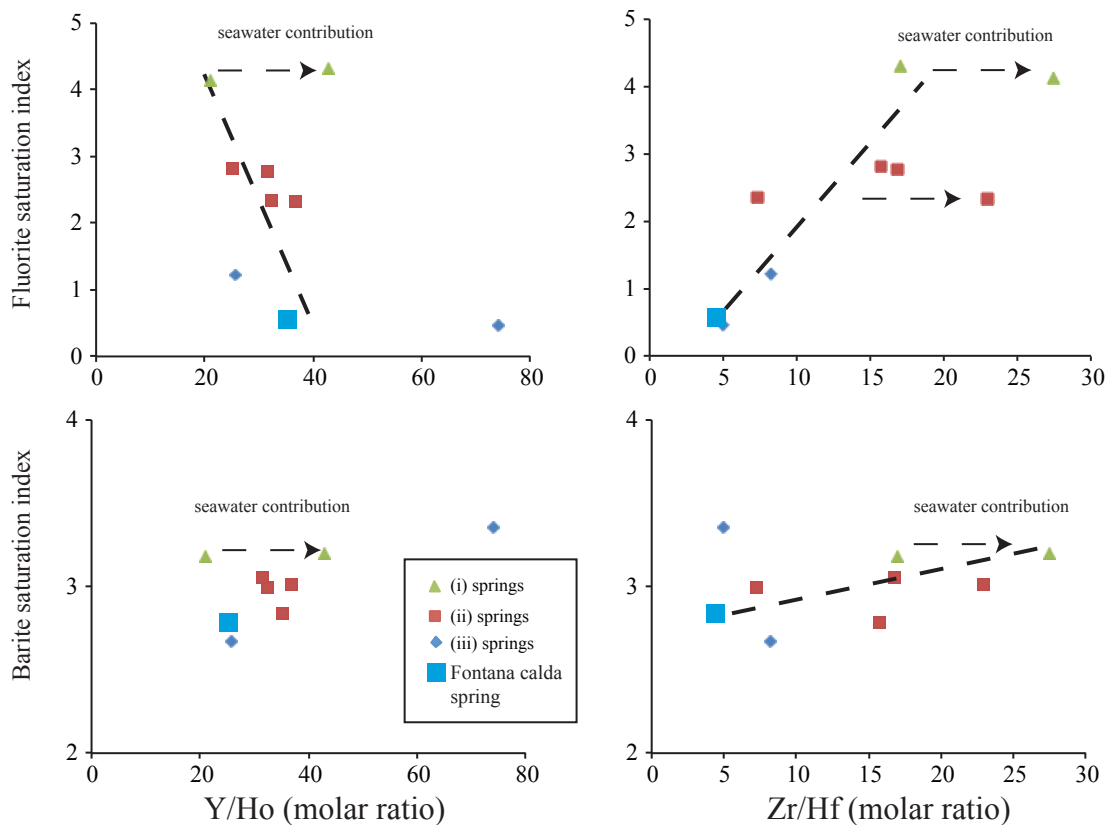


The water sample “Bevaio Pioppo” is characterized by flat shape of the pattern from Eu to Lu, a strong negative Ce anomaly ($Ce/Ce^* = 0.7$) and a progressive concentrations increase from La to Eu suggesting the presence of a superficial circuit supplied by meteoric waters that flow through sediments outcropping in the latest series. This evidence is in agreement with the highest Y/Ho ratios (74) produced by a weak splitting of Y due to preferential removal of Ho onto FeOOH probably present in the soils crossed by water. On the contrary, the spring Partanna is located on the western edge of the Belice graben and it is strongly influenced by a contribution of deep fluids with obvious positive anomaly of Eu ($Eu/Eu^* = 4.37$), subchondritic Y/Ho ratio and a negligible Ce anomaly ($Ce/Ce^* = 0.16$).

Unusually low values of Y/Ho and Zr/Hf ratios of all analysed waters, except that in water sample “Bevaio Pioppo”, can be justified by crystallization processes of neoformation phases by fluid or preferential adsorption of Y and Zr by selected minerals.

In the studied springs no neoformation products were found even if mineralizations in barite, scalenohedral calcite, aragonite and fluorite are reported in the area of Calatafimi and Termini Imerese (Bellanca et al., 1983). In order to clarify if the chemistry of the examined waters was compatible with the crystallization of neoformation phases as a result of water-rock interaction processes, we evaluated the relationships that may exist between Y/Ho and Zr/Hf ratios with water samples saturation index (SI) for fluorite, barite, calcite, aragonite and dolomite (Fig. 3.29).

Fig. 3.29 Saturation index vs Y/Ho and Zr/Hf ratios relationship



(continued)

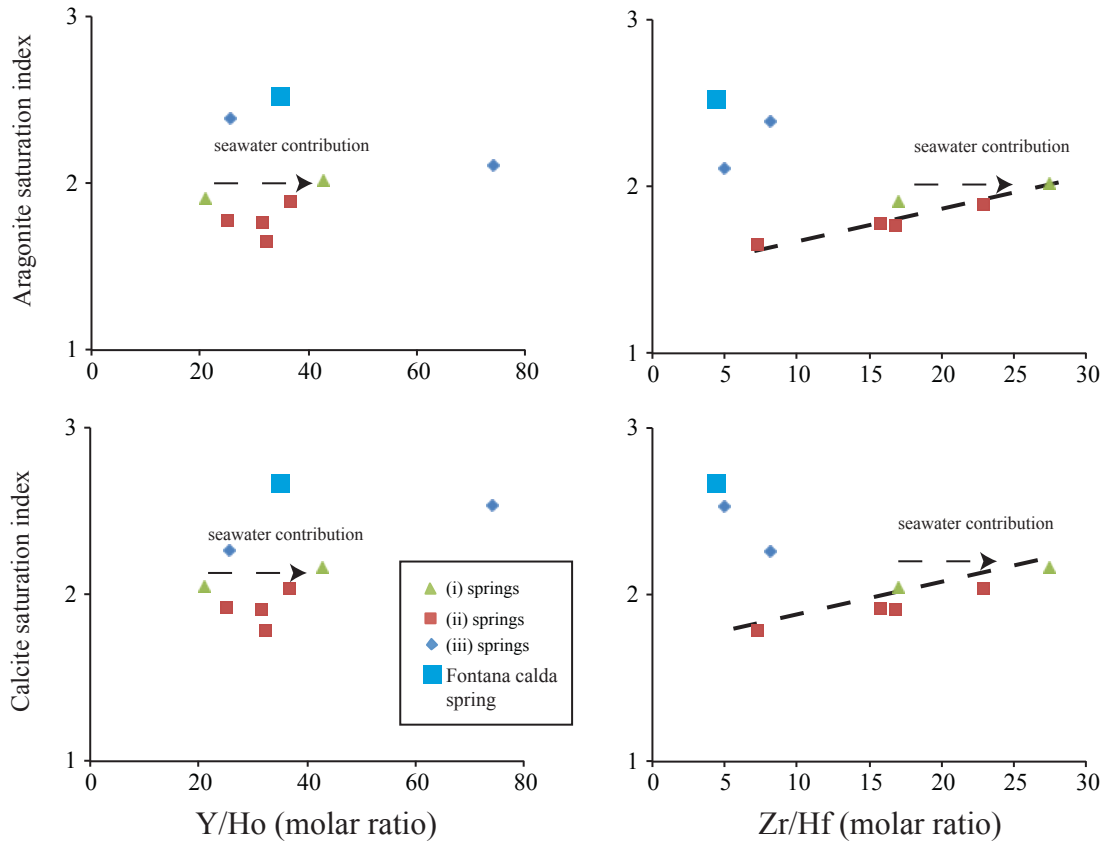


Fig. 3.29 shows a negative correlation occurring for Fluorite saturation index and Y/Ho ratio and a positive correlation between Zr/Hf ratio and SI for all considered phases. Furthermore waters of the (i) group show a Y/Ho and Zr/Hf shift, probably due to introduction into thermal circuit of seawater, characterised by larger Y/Ho and Zr/Hf molar ratios. Moreover, with respect to saturation index, the Zr/Hf ratio is more sensitive than Y/Ho, describing significant relationships for the polymorphic phases of CaCO_3 .

The described evidence could have a crystal chemical significance related to the size of different coordination polyhedra coordinated by YREE, Zr and Hf in considered phases; Fluorite and Barite have VIII-coordinated polyhedra whereas metals in Aragonite and Calcite occupy IX and VI coordinated polyhedra, respectively. Since the classic coordination of YREE is VIII or IX, this would be likely proving that Calcite is disadvantaged in incorporating YREE in the place of Ca in a crystal structure.

3.4. Comprehensive discussion

Key locations to study the geochemical behaviour of the Zr-Hf couple are those interface regions where the occurrence of heterogeneous reaction system conditions can induce geochemical decoupling between Zr and Hf. In marine systems these interfaces can be recognised in:

1. the shallowest water layer up to 100-200 m depth where dissolutions of atmospheric particulates delivered by fallout occur, representing the main source of minor and trace elements for an oligotrophic marine system such as Mediterranean Sea.
2. water layers between oxic water column and underlying anoxic deep-sea brines, where dissolutions of authigenic particulate, formed along the water column under oxic conditions takes place, inducing chemical migrations downwards towards hypersaline brines.

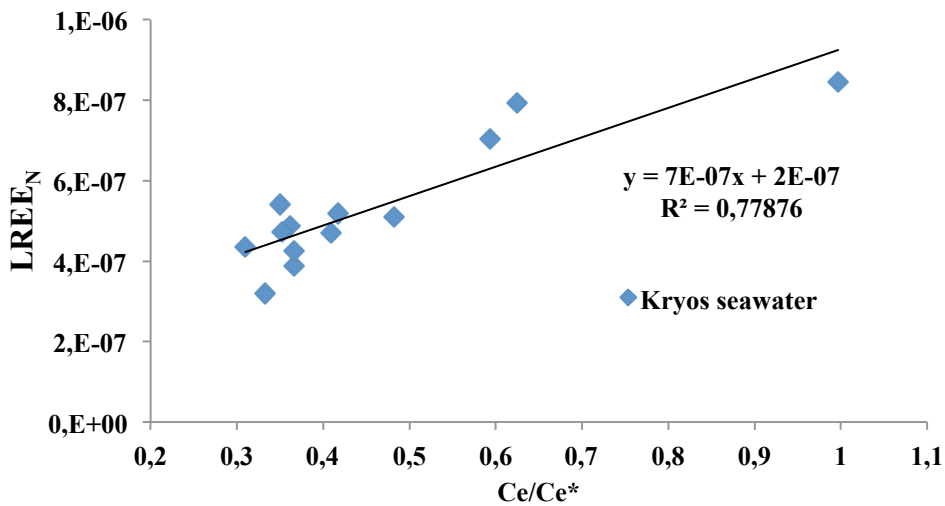
In both environments, Zr and Hf behaviour is poorly known and little investigated (Firdaus et al., 2011 and references therein) apart for the studied particle affinity of these elements towards Fe-oxyhydroxides (Bau and Koschinsky, 2006). The tool to evaluate Zr and Hf behaviour is given by comparison with the REE one,, when studied under the same conditions (Bau et al., 1997).

For this study, further information about Zr and Hf fate during heterogeneous reaction system conditions was sought at locations where mixing processes occurred between fluids with different nature and compositions, and crystallizations of authigenic suspended particulates in shallow submarine hydrothermal vents occurred. Moreover, Zr and Hf behaviour was investigated during rock-water interactions under different temperature conditions in thermal and spring waters. This choice allowed us to clarify analogies and/or differences between Zr and Hf fates during weathering of lithogenic materials that is considered the main source of both elements for oceans (Firdaus et al., 2011 and references

therein). Also in these systems, a useful investigating tool was represented by specific features of REE behaviour. These features can be summarized in terms of changes of some parameters assessed by normalised REE concentrations (Ce/Ce^* , Eu/Eu^* , LREE fractionations with respect to HREE and MREE) associated with the amplitude of Y-Ho decoupling, having several analogies with respect to Zr/Hf ratio.

REE distributions along the investigated water column, and the behaviour of Ce/Ce^* and Y/Ho ratio, represent the key to understand geochemical features of Zr-Hf couple and relate them to the processes taking place in the sampled area. As demonstrated by REE and Ce/Ce^* signature of studied waters, LREE content of seawater progressively decreases along the water column similarly to Ce/Ce^* anomaly that reaches a minimum between 0.35 and 0.40 (Fig. 3.30). This process mirrors the dissolution of LREE-enriched suspended atmospheric dust in contact with shallow seawater layers and their preferential scavenging onto authigenic suspended particulate.

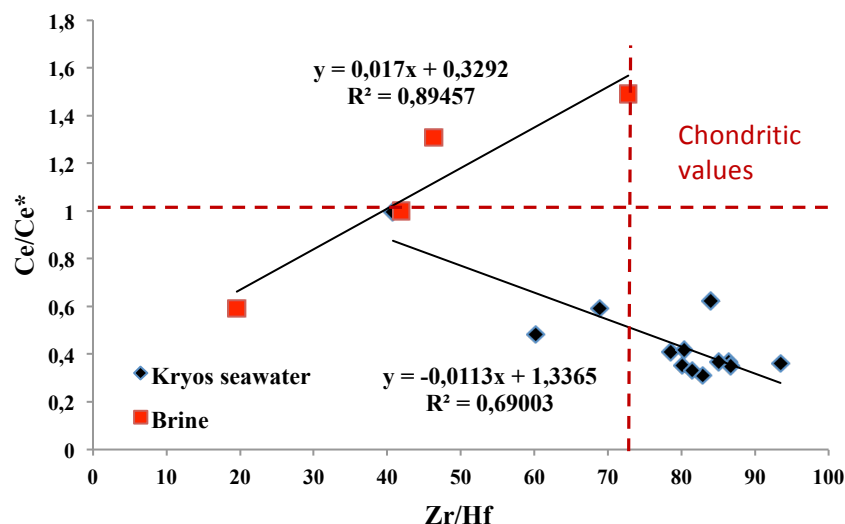
Fig. 3.30 Ce/Ce^* and LREE along the water column



During this process, Ce released from Fe-rich coatings of atmospheric particles is involved in oxidative scavenging onto Mn and/or Fe oxyhydroxides (Byrne and Kim, 1990; De Carlo, 1993; De Carlo et al., 1997; Kawabe et al., 1999; Quinn et al., 2006) even if Ce

preferential association to Fe or Mn species during scavenging remains a debated argument (Bau and Koschinsky, 2009). Whilst Ce scavenging can occur onto both Mn and Fe-rich hydrous oxides, the aqueous behaviour of tetravalent Zr and Hf is mainly related to hydrous Fe oxides (Bau and Koschinsky, 2006). Therefore the recognised relationship between Ce/Ce^* and Zr/Hf indicates that also Ce is involved in the same process driving Zr and Hf behaviour in seawater, namely scavenging onto Fe oxyhydroxides (Fig.3.31). Being Hf more particle-sensitive than Zr (Godfrey et al., 1996), as demonstrated by the increasing Zr/Hf ratio from charge and radius controlled conditions to processes driven by electronic configuration of elements (Bau, 1996), scavenging onto Fe oxyhydroxides should allow for the parallel increase of Zr/Hf and amplitude of negative Ce anomaly along the water column. This hypothesis is confirmed by Zr/Hf vs. Ce/Ce^* behaviour in anoxic brines, where the previously reported negative correlation changes to a significantly and positively correlated linear trend (Fig. 3.31), which demonstrates that Ce removal from dissolved phase in seawater is due to oxidative behaviour related to Fe oxyhydroxides formation. Both Zr and Hf are involved in scavenging onto these materials.

Fig. 3.31 Ce/Ce^* vs Zr/Hf for seawater and brine



Usually, the main feature proving the hydrothermal origin of an investigated fluid consists of the recognition of positive Eu anomalies.

At the same time Y-Ho twin in that fluid is decoupled when this fluid mix with oxygenated ambient bottom waters, changing from geochemical behaviour bringing memory of occurred solid-liquid interactions with host rock of the hydrothermal system to those typical for a cold, weakly alkaline carbonated seawater (Klinkhammer et al., 1994). Being Zr and Hf a geochemical couple that shares some similarities with Y and Ho, any effects of hydrothermal fluxes in terms of Zr, Hf and REE distributions in seawater, have been investigated by means of relationships occurring in Eu/Eu^* vs. Y/Ho , and Eu/Eu^* vs. Zr/Hf . Effects induced by rock-water interactions in hydrothermal and groundwater systems have also been described. The evolution of Y/Ho values during rock-water interactions would be influenced by the amplitude of these processes due to: a) different dissolved behaviour of Y with respect Ho, and b) to the crystallization of authigenic phases that differently involves Y and Ho in surface complexation phenomena. Due the lack of knowledge about Zr and Hf behaviour during similar processes our geochemical investigations of thermal and groundwaters have led to the recognition of effects of these processes on Zr-Hf geochemical couple.

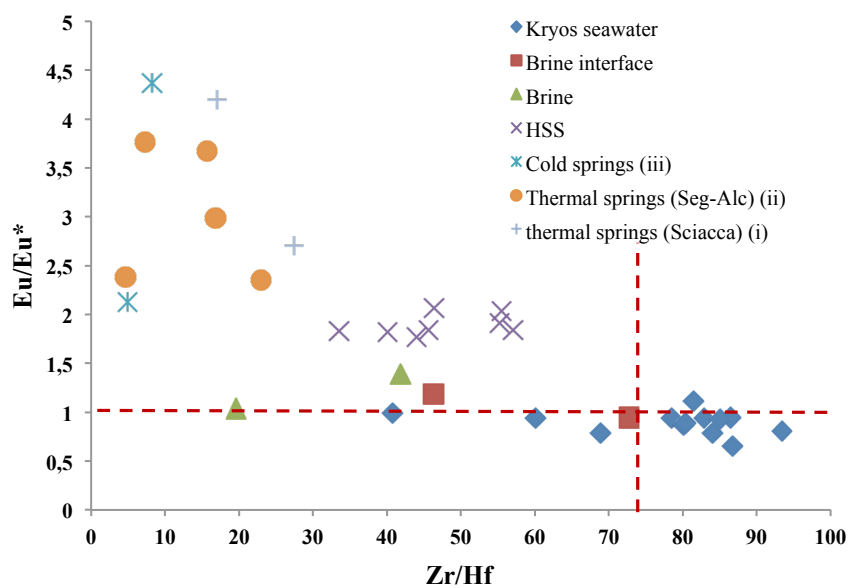
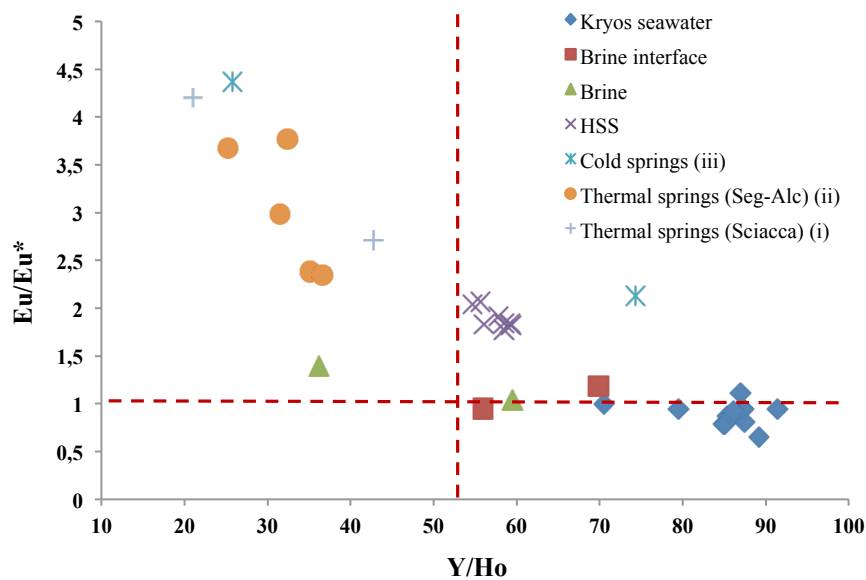
In this study, I show inverse linear relationship between Eu anomaly and Y/Ho values in thermal waters collected in thermal spring area in western Sicily (Fig. 3.32). This relationship occurs from values ranging between $\text{Eu}/\text{Eu}^* \approx 3$ and $\text{Y}/\text{Ho} \approx 25$ (molar ratio) and $\text{Eu}/\text{Eu}^* \approx 1$ and Y/Ho close to chondritic values (Fig. 3.32).

Highest Eu/Eu^* values and lowest Y/Ho ratios are reported for Sciacca (i) thermal springs and for Partanna sample (iii) confirming the presence of a deep-input; whereas lowest Eu/Eu^* values and highest Y/Ho ratios are found in cold waters of Bevaio Pioppo, thus corroborating the meteoric origin of these waters. Highest temperature springs underwent

stronger rock-water interactions, and their observed Y/Ho values are probably due to these interaction leading to the formation of hydrothermal phases (Fluorite and Barite)

Fig. 3.32 Eu/Eu* vs Y/Ho and Zr/Hf

(dotted lines mark chondritic values)



In Fig. 3.32 features of HSS at Panarea likely represent the link between linear trend of thermal springs from Western Sicily and seawater samples from Eastern Mediterranean, where Y/Ho and Eu/Eu* values are driven by equilibria between dissolved- and surface-REE complexes. This evidence suggests that the Eu/Eu* vs. Y/Ho relationship can be used to detect mixing features in dissolved media, ranging from typical marine conditions to classical hydrothermal system in carbonate rocks through intermediate marine-hydrothermal fluids mixture conditions.

Therefore this relationship can be interpreted as a tool to recognize geochemical processes involving REE, ranging from conditions close to equilibrium (in terms of surface vs. dissolved complexation) towards conditions far from equilibrium where hydrothermal dissolution of host rocks occurs. This suggestive hypothesis is corroborated by features of seawater samples and deep-sea brines shown in Fig. 3.32. Here samples from intermediate and deep water column are clustered around superchondritic Y/Ho values and Eu/Eu* close to 1. Both values are typical for seawater under oceanic conditions. On the contrary, Y/Ho values from the shallowest water layers and brines fall along a linear trend towards lower Y/Ho values that I propose being the result of dissolution of Fe oxyhydroxides in suspended particulates under reducing conditions (in brines), and dissolution of Fe oxyhydroxide coatings of atmospheric delivered particulates (in shallowest water layers). In both cases, larger Ho affinity for Fe-oxyhydroxides caused progressive Y/Ho reductions from superchondritic to subchondritic values.

Features of Zr/Hf vs. Eu/Eu* relationship in studied waters is substantially similar to the scenario depicted by Y/Ho changes (Fig. 3.32), suggesting that Zr and Hf behave similarly to Y and Ho during these processes. The linear shifts, described by shallowest seawaters and deep-sea brines from values calculated in open seawaters, are due to the dissolution of authigenic Fe-oxyhydroxides under reducing conditions in deep sea brines and of detrital Fe-

rich coatings of atmospheric particles in shallowest water layers. In both cases Hf behaves similarly to Ho, showing a higher particle affinity than Zr that explains why Hf is preferentially scavenged onto Fe-oxyhydroxides (Boswell and Elderfield, 1988; McKelvey and Orians, 1998; Godfrey et al., 1996). In the same graph, low Zr/Hf ratios in thermal springs are probably the results of incongruent weathering postulated by several authors that is considered a suitable Hf source from rock-water interactions (Rickli et al., 2009; Stichel et al., 2011). Hf fluxes can be otherwise justified by delivery of significant radiogenic Hf from deep-seated hydrothermal fluids (van de Flierdt et al., 2007); this hypothesis would agree with He isotopic data reported in these springs (Caracausi et al., 2005). In both cases the amount of preferentially released Hf that contributes to the observed Zr/Hf ratio in thermal springs, is certainly related to rock-water interactions and can be considered a further indicator of these processes. In the samples from thermal springs, superchondritic Eu/Eu* values corroborate the amplitude of rock-water interactions under hydrothermal conditions, in agreement with the hypothesis that crystallization of hydrothermal phases took place (Godfrey, 1995; Bau, 1996).

3.5. Conclusion

Solid-liquid processes are responsible for the composition of hydrosphere, hence their study is of great interest to understand the health status of the environment. As a general rule, solid-liquid processes are not related to physical characteristics of involved elements (charge and radius), being those determined by electronic configurations (non-CHARAC processes). Beginning from late 70s, quantification of REE distributions, amplitudes of elemental fractionation along the series and Y/Ho ratio have been used as useful geochemical tools able to describe the natural occurrence of non-CHARAC processes through improved analytical techniques. Subsequently, the Zr-Hf geochemical couple started to be used, together with Y/Ho ratio and REEs distributions, to investigate non-CHARAC processes. Like for REE, researches started from investigating rocks and minerals, but later expanded the analysis to dissolved media by means of neutron activation analyses. However, a comprehensive analytical method suitable to simultaneous determinations of Zr, Hf and REE from the same sample was lacking, along with a comprehensive statistical approach that would allow to keep all analytical determinations under control. This requirement was magnified by the absence of certified reference materials for the determinations of these elements. During the last fifteen years, researches investigating origins, elemental fluxes and Zr-Hf distributions in seawater and rivers were carried out, but to date only scarce data about distributions of these elements in thermal waters are known, and nothing was published about REE, Zr and Hf comparative data collected in hydro-sphere far from oceanic system.

The present research tried to fill all these gaps and provide all those long-needed analytical tools. I set up an analytical method allowing the simultaneously investigation of REE, Zr and H in dissolved media under several geochemical conditions. Geochemical results obtained comparing behaviour of Zr-Hf and Y-Ho couples, REE distribution, Eu and Ce anomaly values in different studied systems allowed us to clarify the role played by Fe-rich

materials to determine REE fate during scavenging-dissolution equilibria. In particular, the strong analogy found between Ce distribution and Zr/Hf variations, demonstrates that oxidative Ce scavenging in marine environment is related to Fe-oxyhydroxides, rather than to Mn species, contributing for the first time to clarify Ce fate under natural seawater conditions, far from laboratory experiments and analytical simulations.

I was able to relate variations of Zr/Hf and Y/Ho ratios to amplitudes of hydrothermal supply (evaluated in terms of Eu/Eu^*) also in dissolved media under different chemical-physical natural conditions in variable temperature thermal sources, in deep-sea brines, in submarine hydrothermal vents and in seawater column under oceanic conditions. Results thus obtained have expanded the scientific knowledge about the meaning of decoupling phenomena for Y-Ho and Zr-Hf couples, and the relationships with dissolved complexation of these elements. Lastly, this study has shed light upon the necessity to increase the knowledge of Zr-Hf behaviour under several natural conditions and to compare it with data related to REE behaviour.

Appendix A

Fig. A.1 Physical Chemical parameters for Medea (a), Tyro (b) and Thetis from oxic water to anoxic brine

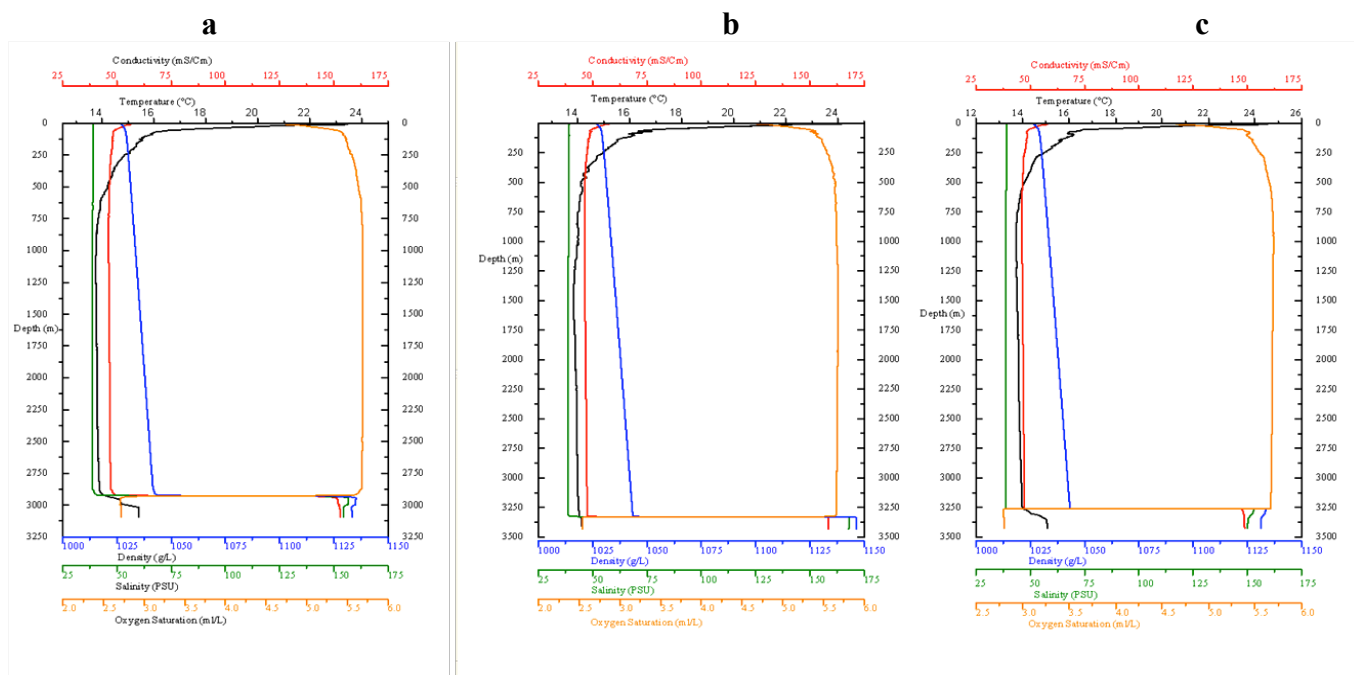


Fig. A.2 Physical Chemical parameters for Medea (a), Tyro (b) and Thetis from interface and anoxic brine

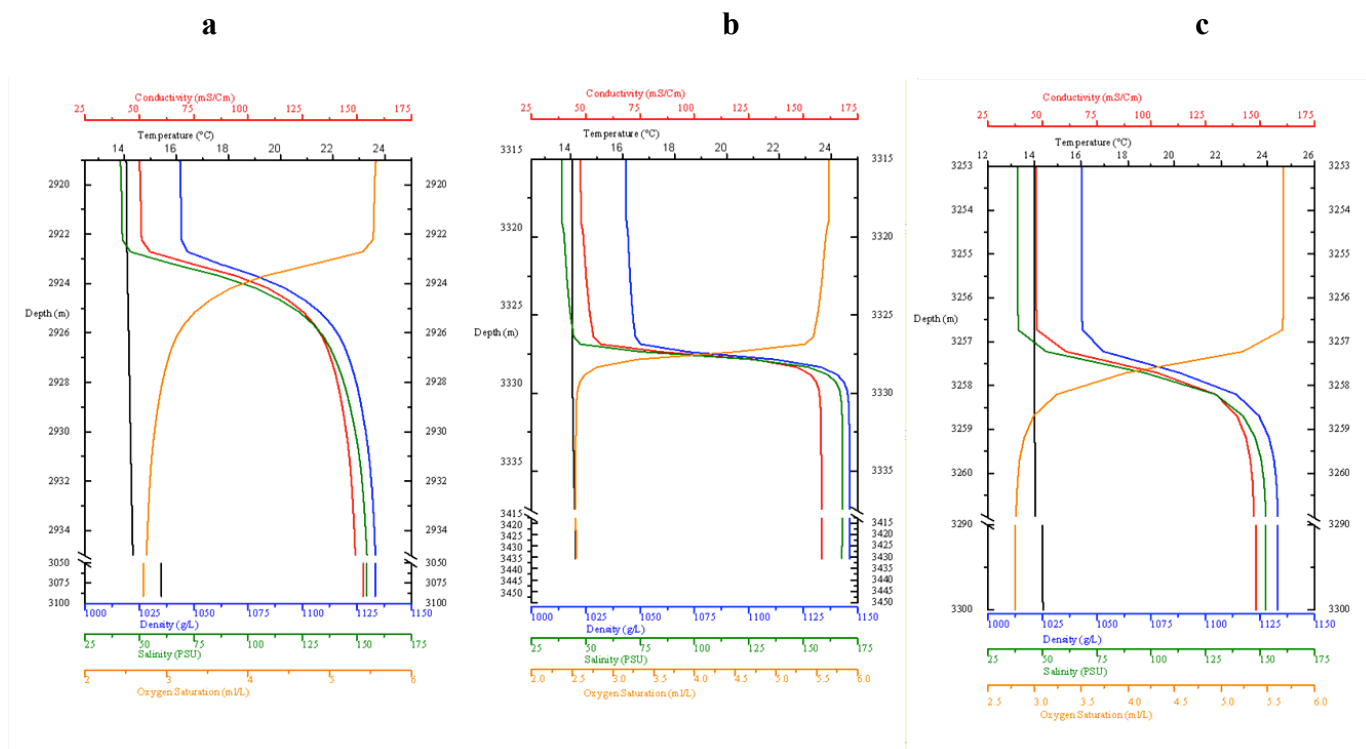
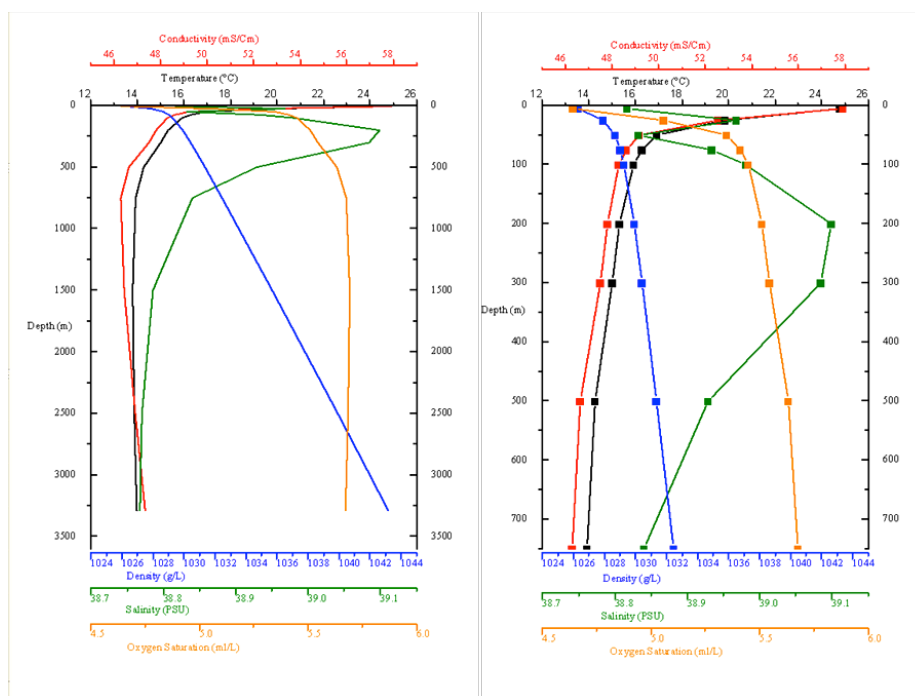


Fig. A.3 Physical Chemical parameters for Kryos water column

References

- Alibo, D. S., and Nozaki, Y. (1999). Rare earth elements in seawater: Particle association, shale normalization, and Ce oxidation. *Geochim. et Cosmochim. Acta*, 63 (3/4), 363-372.
- Alibo, D. S., and Nozaki, Y. (2000). Dissolved rare earth elements in the South China Sea: Geochemical characterization of the water masses. *Journal of Geophys. Res. C: Oceans*, C12 (105), 28771-28783.
- Baes, C., and Mesmer, R. (1976). The Hydrolysis of Cations. 152-157.
- Banks, D., Siewers, U., Sletten, R. S., Haldorsen, S., Dale, B., Heim, M.. (1999). The thermal springs of Bockfjorden, Svalbard: II: Selected aspects of trace element hydrochemistry. *Geothermics*, 6 (28), 713-728.
- Banner, J. L., Wasserburg, G. J., Dobson, P. F., Carpenter, A. B., and Moore, C. H. (1989). Isotopic and trace element constraints on the origin and evolution of saline groundwaters from central Missouri. *Geochim. et Cosmochim. Acta*, 2 (53), 383-398.
- Bau, M. (1996). Controls on the fractionation of isovalent trace elements in magmatic and aqueous system: evidence from Y/Ho, Zr/Hf, and lanthanide tetrad effect. *Contrib. Mineral. Petrol.*, 123, 323-333.
- Bau, M. (1999). Scavenging of dissolved Yttrium and rare earth earth by precipitating iron oxyhydroxide: Experimental evidence for Ce oxidation, Y-Ho fractionation, and lanthanide tetrad effect. *Geochim. et Cosmochim. Acta*, 63 (1), 67-69.
- Bau, M., and Alexander, B. W. (2009). Distribution of high field strength elements (Y, Zr, REE, Hf, Ta, Th, U) in adjacent magnetite and chert bands and in reference standards FeR-3 and FeR-4 from the Temagami iron-formation, Canada, and the redox level of the Neoarchean ocean. *Precambrian Research*, 3-4 (174), 337-346.
- Bau, M., and Dulski, P. (1995). Comparative study of Yttrium and rare-earth element behaviours in fluorine-rich hydrothermal fluids. *Contribut. to Mineral. and Petrol.*, 2-3 (119), 213-223.
- Bau, M., and Koschinsky, A. (2006). Hafnium and Neodymium isotopes in seawater and in ferromanganese crusts: The "element perspective". *Earth and Planetary Science Letters*, 3-4 (241), 952-961.
- Bau, M., and Koschinsky, A. (2009). Oxidative scavenging of Cerium on hydrous Fe oxide: Evidence from the distribution of rare earth elements and Yttrium between Fe oxides and Mn oxides in hydrogenetic ferromanganese crusts. *Geochemical Journal*, 1 (43), 37-47.
- Bau, M., Moller, P., and Dulski, P. (1997). Yttrium and lanthanides in Eastern Mediterranean seawater and their fractionation during redox-cycling. *Mar. Chem.*, 56, 123-131.
- Bellanca, A., Censi, P., Neri, R. (1983). Studio isotopico, chimico e tessiturale su materiali carbonatici associati a mineralizzazioni di fluorite e barite nell'area di Termini Imerese (Sicilia). *Rendiconti della Societa Italiana di Mineralogia e Petrologia*, 38, (3) 1251-1261.
- Boswell, S.M., Elderfield, H. (1988). The determination of Zirconium and Hafnium in natural waters by isotope dilution mass spectrometry, *Mar. Chem.*, 25, (3), 197-209.

- Bregant, D., Catalano, G., Civitarrese, G., and Lucchetta, A. (1990). Some chemical characteristics of the brine in Bannock and Tyro basins: Salinity, sulphur compounds, Ca^{2+} , f, pH, a, PO_4^{3-} , SiO_2 , NH_3 . *Mar.Chem.*, 31, 35-62.
- Burke, S. (2001). Regression and Calibration. *LC-EG Europe Online Supplements*, 13-17.
- Byrne, R. H., and Kim, K. H. (1990). Rare earth element scavenging in seawater. *Geochim. et Cosmochim. Acta*, 10 (54), 2645-2656.
- Byrne, R., and Lee, J. (1993). Comparative Yttrium and rare earth element chemistries in seawater. *Mar. Chem.*, 44, 121.
- Byrne, R., and Sholkovitz, E. (1996). Marine chemistry on geochemistry of the lanthanides. In handbook of the physics and chemistry of rare earth. 23, 497-593.
- Calanchi, N., Tranne, C. A., Lucchini, F., and Rossi, P. L. (1999). Geological map of the Island of Panarea and Basiluzzo, Aeolian Island, 1:10000 scale. *G.N.V.Siena*.
- Camerlenghi, A. (1990). Anoxic basins of the eastern Mediterranean: Geological framework. *Mar. Chem.*, 31, 1-19.
- Capaccioni, B., Tassi, F., Vaselli, O., Tedesco, D., and Podera, K. (2006). Submarine gas burst at Panarea Island (Southern Italy) on 3 November 2002: a magmatic versus hydrothermal episode. *Journal. Of Geophys. Res.*, 112, B05201.
- Caracausi, A., Favara, R., Italiano, F., Nuccio, P.M., Paonita, A., Rizzo, A. (2005). Active geodynamics of the central Mediterranean Sea: Tensional tectonic evidences in Western Sicily from mantle-derived Helium. *Geophys. Res. Letters*, 32, (4), 15.
- Cassiaux, M., Proust, D., Siitari-Kauppi, M., Sardini, P., and Leutsch, Y. (2006). Clay minerals formed during propylitic alteration of a granite and their influence on primary porosity: A multi-scale approach. *Clay and Clay minerals*, 5 (54), 541-554.
- Catalano, R., Macaluso, T., Monteleone, S., and Calandra, D. (1983). Lineamenti geostrutturali ed idrogeologici e geotermici della Sicilia occidentale. *CNR-PFE-RF13*.
- Catalano, R., D'argenio, B. (1982). Schema geologico della Sicilia - In: Catalano R. and D'Argenio B. (Eds.) Guida alla Geologia della Sicilia Occidentale. Guide Geologiche Regionali. – Mem. Soc. Geol. It., 24 (Suppl. A), 43-42.
- Cotton, F., and Wilkinson, J. (1968). Chimica inorganica.
- Cotton, S. (2007). Lanthanide and Actinide Chemistry.
- Daux, V., Crovisier, J. L., Hemond, C., and Petit, J. C. (1994). Geochemical evolution of basaltic rocks subjected to weathering: fate of the major elements, rare earth elements, and thorium. *Geochim. et Cosmochim. Acta*, 22 (58), 41-49.
- De Carlo, E. H. (1993). Geochemistry of pore water and sediments recovered from Leg 136, Hawaiian Arch. *Proc., Scientific results, OPD Leg 133, Hawaiian Arch*, 77-83.

- De Carlo, E. H., Wen, X. Y., and Irving, M. (1997). The influence of redox reactions on the uptake of dissolved Ce by suspended Fe and Mn oxide particles. *Aquatic Geochemistry*, 3 (4), 357-389.
- De Giudici, G., and Zuddas, P. (2001). In situ investigation of galena dissolution in oxygen saturated solution: evolution of surface features and kinetic rate. *Geochim. et Cosmochim. Acta*, 65 (65), 1381-1389.
- de Lange, G. J., Boelrijk, N., Catalano, G., Corselli, C., Klinkhammer, G. P., Middelburg, J. J., et al. (1990b). Sulphate-related equilibria in the hypersaline brines of the Tyro and Bannock basins, Eastern Mediterranean. *Mar. Chem.*, 31, 89-112.
- de Lange, G., Middelburg, J., Weijden, C. D., Catalano, G., Luther, G.W., Hydes, D.J. (1990a). Composition of anoxic hypersaline brines in Tyro and bannock basins, Eastern Mediterranean. *Mar. Chem.*, 31, 63-88.
- Donat, J., and Dryden, C. (2001). *Transition metals and heavy metal speciation* (Vol. Encyclopedia of Ocean Science).
- Douville, E., Bienvenu, P., Charlou, J. L., Donval, J. P., Fouquet, Y., Appriou, P., (1999). Yttrium and rare earth elements in fluids from various deep-sea hydrothermal systems. *Geochim. et Cosmochim. Acta*, 63 (63), 627-643.
- Ece, O. I., and Nakagawa, Z. E. (2003). Alteration of volcanic rocks and genesis of kaolin deposits in the Şile region, northern Istanbul, Turkey. Part II: Differential mobility of elements. *Clay Minerals*, 38 (38), 529-550.
- Ederfield, H., and Greaves, M. (1988). *Nature*, 334, 214.
- Fancelli, R., Monteleone, S., Nuti, S., Pipitone, G., Rini, S., and Taffi, L. (1991). Nuove conoscenze idrogeologiche e geotermiche della Sicilia occidentale. *Geologia e idrogeologia*, 26.
- Favara, R., Grassa, F., Inguaggiato, S., and Valenza, M. (2001). Hydrogeochemistry and stable isotopes of thermal springs: Earthquake-related chemical changes along Belice Fault (Western Sicily). *Applied Geochemistry*, 16 (16), 1-17.
- Firdaus, M. L., Norisuye, K., Nakagawa, Y., Nakatsuka, S., and Sohrin, Y. (2008). Dissolved and labile particulate Zr, Hf, Nb, Ta, Mo and W in the western North Pacific Ocean. *Journal of Oceanography*, 64, 247-257.
- Firdaus, M., Minami, T., Norisuye, K., and Sohrin, Y. (2011). Strong elemental fractionation of Zr-Hf and Nb-Ta across the Pacific Ocean. *Nature Geoscience*, 4, 227-230.
- Gabbianelli, G., Romagnoli, C., Rossi, P. L., and Calanchi, N. (1993). Marine geology of the Panarea-Stromboli area Eolian Archipelago, Southeastern, Tyrrhenian Sea. *Acta Vulcanology*, 3, 11-20.
- German C.R., Klinkhammer G.P., Edmond J.M., Mitra A. and Elderfield H. (1990). Hydrothermal scavenging of rare-earth elements in the ocean. *Nature*, 345 (6275), 516-518.
- German C.R. and Von Damm K.L. (2005). Hydrothermal Processes, In: Elderfield H. eds., *Treatise of Geochemistry* Vol. 6, 181-222.

- Godfrey, L. V., Field, M. P., and Sherrel, R. M. (2008). Estuarine distributions of Zr, Hf, and Ag in the Hudson River and the implications for their continental and anthropogenic sources to seawater. *Geochemistry, Geophysics, Geosystems*, 12 (9).
- Godfrey, L. V., Lee, D. C., Sangrey, W. F., Halliday, A. N., Salters, V. J., Hein, J. R., et al. (1997). The Hf isotopic composition of ferromanganese nodules and crusts and hydrothermal manganese deposits: Implications for seawater Hf. *Earth and Planetary Science Letters*, 1-2 (151), 91-105.
- Godfrey, L., White, W., and Salters, V. (1996). Dissolved Zirconium and Hafnium distributions across a shelf break in the North Eastern Atlantic Ocean. *Geochim. et Cosmochim. Acta*, 60 (21), 3995-4006.
- Gonzales, G., and Herrador, M. (2007). A practical guide to analytical method validation, including measurement uncertainty and accuracy profile. *Trends in Analytical Chemistry*, 26 (3).
- Greaves, M.J., Elderfield, H., Sholkovitz, E.R. (1999). Aeolian sources of rare earth elements to the Western Pacific Ocean. *Mar. Chem.*, 68, (2), 31-38.
- Haley, B. A., Klinkhammer, G. P., and McManus, J. (2004). Rare earth elements in pore waters of marine sediments. *Geochim. et Cosmochim. Acta*, 6 (68), 1265-1279.
- Implementing Council Directive 96/23/EC concerning the performance of analytical methods and the interpretation of results. (2002). *European Commission, 2002/605/EC*, 1-29.
- In-house method validation : a guide for chemical laboratories/produced by LGC as part of the DTI VAM Programme.* (2003). Teddington.
- International Vocabulary of basic and general terms in Metrology (VIM). (1993). ISO.
- Irber, W. (1999). The lanthanide tetrad effect and its correlation with K/Rb, Eu/Eu*, Sr/Eu, Y/Ho, and Zr/Hf of evolving peraluminous granite suites. *Geochim. et Cosmochim. Acta*, 3-4 (63), 489-508.
- Kawabe, I., Ohta, A., Ishii, S., Tokumura, M., and Miyauchi, K. (1999). REE partitioning between Fe-Mn oxyhydroxide precipitates and weakly acid NaCl solutions: Convex tetrad effect and fractionation of Y and Sc from heavy lanthanides. *Geochemical Journal*, 3 (33), 167-179.
- Kendrick, M. A., Burgess, R., Pattick, R. A., and Turner, G. (2002). Hydrothermal fluid origins in a fluorite-rich Mississippi Valley-type district: Combined noble gas (He, Ar, Kr) and halogen (Cl, Br, I) analysis of fluid inclusions from the South Pennine ore field, United Kingdom. *Economic Geology*, 97 (3), 435-451.
- Klinkhammer, G., German, C. R., Elderfield, H., Greaves, M. J., & Mitra, A. (1994). Rare earth elements in hydrothermal fluids and plume particulates by inductively coupled plasma mass spectrometry. *Mar. Chem.*, 45 (3), 179-186.
- Koschinsky, A., Hein, J.R. (2003). Uptake of elements from seawater by ferromanganese crusts: Solid-phase associations and seawater speciation. *Marine Geology*, 198, (4), 331-351.
- Linee guida per la validazione dei metodi analitici e per il calcolo dell'incertezza di misura - Accreditamento e certificazione. (2003). *Manuali ARPA*.
- Marini, L., Yock Fung, A., and Sanchez, E. (2003). Use of reaction path modeling to identify the processes governing the generation of neutral Na-Cl and acidic Na-Cl-SO₄ deep geothermal liquids at

- Miravalles geothermal system, Costa Rica. *Journal of Volcanology and Geothermal Research*, 128 (4), 368-387.
- McKelvey, B. A., and Orians, K. J. (1998). The determination of dissolved Zirconium and Hafnium from seawater using isotope dilution inductively coupled plasma mass spectrometry. *Mar. Chem.*, 60, 245-255.
- Miller, J. N., and Miller, J. C. (2005). *Statistics and Chemometrics for Analytical Chemistry*. Pearson.
- Millero, F. (1992). Stability constant for the formation of rare earth inorganic complexes as a function of ionic strength. *Geochim. et Cosmochim. Acta*, 56, 3123-3132.
- Moller, P., Dulski, P., and Luck, J. (1999). Determination of rare earth elements in seawater by inductively coupled plasma-mass spectrometry. *Spectrochimica Acta*, 478 (12), 1379-1387.
- Monecke, T., Kempe, U., Monecke, J., Sala, M., and Wolf, D. (2002). Tetrad effect in rare earth element distribution patterns: A method of quantification with application to rock and mineral samples from granite-related rare metal deposits. *Geochim. et Cosmochim. Acta*, 66, 1185-1196.
- Norén, B. (1967). The fluoride complexes of Zirconium(IV). *Acta Chemical Scandinavica* (21), 2457-2462.
- Ojiambo, S. B., Lyons, W. B., Welch, K. A., Poreda, R. J., and Johannesson, K. H. (2003). Strontium isotopes and rare earth elements as tracers of groundwater-lake water interactions, Lake Naivasha, Kenya. *Applied Geochemistry*, 18, 1789-1805.
- Orians, K., and McKelvey, B. (1998). The determination of dissolved zirconium and hafnium from seawater using isotope dilution inductively coupled plasma mass spectrometry. *Mar. Chem.*, (60), 245-255.
- Pearson, R. G. (1963). Hard and soft acids and bases. *Journal of Am. Chem. Soc.* (85), 3533-3539.
- Peters, M., Strauss, H., Petersen, S., Kummer, N., and Thomazo, C. (2011). Hydrothermalism in the Tyrrhenian Sea: Inorganic and microbial sulfur cycling as revealed by geochemical and multiple sulfur isotope data. *Chemical Geology*, 280, 217-231.
- Quantifying Uncertainty in Analytical Measurements 2nd edition. (2000). *Eurachem Guide*.
- Quinn, P. K., Bates, T. S., Coffman, D., Onasch, T. B., Worsnop, D., Baynard, T., et al. (2006). Impacts of sources and aging on submicrometer aerosol properties in the marine boundary layer across the Gulf of Maine. *Journal of Geophysical Research D: Atmospheres*, 111, 2311.
- Rickli, J., Frank, M., Halliday, A.N. (2009). The Hafnium-Neodymium isotopic composition of Atlantic seawater. *Earth and Planetary Science Letters*, 280, (4), 118-127.
- Schijf, J., de Baar, H., and Millero, F. (1995). Vertical distribution and speciation of dissolved rare earth elements in the anoxic brines of Bannock Basin, Eastern Mediterranean Sea. *Geochim. et Cosmochim. Acta*, 59 (16), 3285-3299.
- Scislewski, A., and Zuddas, P. (2010). Estimation of reactive mineral surface area during water-rock interaction using fluid chemical data. *Geochim. et Cosmochim. Acta*, 74, 6996-7007.
- Shabani, M., Agati, T., Shimizu, H., and Masuda, A. (1990). *Analytical Chemistry*, 62, 2790.

- Sieland, R. (2009). Chemical and isotopic investigations of submarine fluid discharges from Panarea, Aeolian Islands, Italy. *Freiberg Online Geology*, 21.
- Stichel, T., Frank, M., Rickli, J., Haley, B.A. (2011). The Hafnium and Neodymium isotope composition of seawater in the Atlantic sector of the Southern Ocean. *Earth and Planetary Science Letters*, 317-318, (6), 282-294.
- Tachikawa, K., Roy-Barman, M., Michard, A., Thouron, D., Yeghicheyan, D., and Jeandal, C. (2004). Neodymium isotopes in the Mediterranean Sea: Comparison between seawater and sediment signal. *Geochim. et Cosmochim. Acta*, 68, 3095-3106.
- Tamburo, E., Aiuppa, A., Marini, L., & Valenza, M. (2011). Modelling groundwater processes in a carbonate catchment: A case study from the madonie area (northern sicily). *Applied Geochemistry*, 26 (7), 1274-1287.
- Tang, J., and Johannessons, K. (2003). Speciation of the rare earth elements in natural terrestrial water: assessing the role of dissolved organic matter from the modelling approach. *Geochim. et Cosmochim. Acta*, 67, 2321-2339.
- The Fitness for Purpose of Analytical Methods. (1998). *Eurachem Guide*.
- Thompson, M., Ellison, S., and Wood, R. (2002). Harmonized guidelines for single-laboratory validation of the method of analysis. *Pure and Applied Chemistry*, 74 (5), 835-855.
- Thompson, M., Ellison, S., Fajgelj, A., Willetts, P., and Wood, R. (1999). Harmonised guidelines for the use of recovery information in analytical measurement. *Pure and Applied Chemistry*, 71 (2), 337-348.
- van der Flierdt, T. (2007). Global Neodymium-Hafnium isotope systematics-revisited. *Earth and Planetary Science Letters*, 259, 432-441.
- White W.H. (2001). *Geochemistry*. 266.
- Zhong, S., Mucci, A. (1995). Partitioning of rare earth elements (REEs) between calcite and seawater solutions at 25°C and 1 atm, and high dissolved REE concentrations. *Geochim. et Cosmochim. Acta*, 59, (3), 443-453.
- Zuddas, P., and Michard, G. (1993). Experimental mineral-fluid interaction in the Na-Ca-(Sr)Al-Si system. *European Journal of Mineralogy*, 5 (5), 807-818.
- Zuddas, P., and Michard, G. (1990). Trace elements behaviour during fluid-plagioclase interaction: Experimental study. *Chemical Geology*, 84 (1-4), 337-338

Acknowledge

I wish to thank my tutors, Paolo Censi and Filippo Saiano for their help and support throughout my research. I would like to thank the members of PhD programme board for their valuable advice over the years as have been important for my scientific growth.

I want to thank the IAMC-CNR Institute U/O Messina and Capo Granitola for sampling in the eastern Mediterranean Sea and Dr. Pietro Aricò for diving in Panarea.

A special thank to Doriana for her precious help in the manuscript language revision and to the reviewers Dr. T. Darrah, Prof. S. A. Wodd, and Prof. P.Zuddas for accepting to review my paper and for their constructive criticisms that helped me to improve the quality of the text.

Finally I would like to thank my family and Nicola as they have always believed in me and they have been patient and close to me during this research period.